Multiscale Modelling of Biological Systems: A Computational Approach to Studying Natural Phenomena from Cellular to Ecological Levels

Wieloskalowe modelowanie systemów biologicznych: obliczeniowe podejście do badania zjawisk naturalnych od poziomu komórki po ekosystemy

Faculty of Mathematics and Computer Science
Adam Mickiewicz University, Poznań

Andrzej Kokosza

Thesis supervisor (Promotor): prof. UAM dr hab. Krzysztof Dyczkowski
Thesis assistant supervisor (Promotor pomocniczy): dr Wojciech Pałubicki

A doctoral dissertation in natural sciences in the discipline of computer and information sciences.
Rozprawa doktorska w dziedzinie nauk ścisłych i przyrodniczych, dyscyplina informatyka

June 2024

Dedykuję tę pracę mojej żonie, Martynie, której miłość i wiara we mnie były nieocenionym wsparciem na każdym etapie doktoratu.

Acknowledgements

I would like to express my deepest gratitude to Prof. Dr Krzysztof Dyczkowski, whose expertise, understanding, and patience, added considerably to my graduate experience. Your guidance helped me in all the time of research and writing of this thesis.

I am equally thankful to my co-advisor, Dr Wojciech Pałubicki, whose insights and expertise in modeling of natural phenomena have been invaluable throughout this process. Your rigorous standards pushed me to refine my ideas and encouraged my academic growth.

I would like to acknowledge the efforts and contributions of the co-authors I had the privilege to work with during my research. First Prof. Dr Agata Burian for introducing me to the real of plant biomechanics and giving me opportunity to join her research project. I also extend my gratitude to Dr Chang Su, Prof. Dr Kaisa Nieminen, and Prof. Dr Ykä Helariutta for enabling me to enhance their findings with my modelling expertise. Lastly, I am thankful for the fruitful collaboration with Prof. Dr Dominik L. Michels, Prof. Dr Sören Pirk, Helge Werde, Daniel Gonzalez Espraza, Dr Miołosz Makowski, Dr Daoming Liu which culminated in our successful SIGGRAPH publication.

This work was supported by the research grant SONATA BIS6 (2016/22/E/NZ3/00342) from the National Science Centre, Poland.

Abstract

The study of natural phenomena gives rich opportunities for those interested in modelling and simulations. The challenge they present lies in the complexity, dynamic nature, and sheer variety of patterns such as wildfires or plant growth. These processes, ranging from the cellular mechanisms that dictate the growth and function of living organisms to the environmental or ecological dynamics that shape our environment manifest unique behaviours and patterns that challenge our understanding and push the boundaries of traditional scientific disciplines.

This thesis shows the development and validation of several computational models that simulate complex biological processes across various scales. The goal of this dissertation is first to demonstrate that computational models can accurately replicate and predict complex biological systems across different scales; second to illustrate the necessity of diverse modelling approaches to address distinct biological phenomena; and third, to illustrate that mathematical models can be utilized to validate or challenge existing biological theories and identify areas requiring further investigation.

I present three models of specific natural phenomena validated against empirical data. These include a discrete model for vascular pattern formation in Arabidopsis thaliana, a continuous model of long-distance signalling in birch trees, and an advanced hybrid simulation of wildfires. The results supported the assumptions posed, Additionally, they allowed us to assess the applicability of modelling paradigms used in different scenarios. The findings underscore the crucial role of interdisciplinary approaches in advancing our knowledge.

Streszczenie

Badanie zjawisk naturalnych za pomocą modelowania matematycznego i symulacji komputerowej oferuje szerokie możliwości ze względu na złożoność, dynamiczną naturę i różnorodność wzorców obserwowanych w procesach takich jak pożary lasów czy wzrost roślin. Te zjawiska, począwszy od mechanizmów komórkowych, które kierują wzrostem i funkcjonowaniem żywych organizmów, po szeroko zakrojone dynamiki ekologiczne kształtujące nasze środowisko, prezentują unikalne zachowania i wyzwania. Takie badania nie tylko zwiększają nasze zrozumienie, ale również przesuwają granice tradycyjnych dyscyplin naukowych, przyczyniając się istotnie do nauk biologicznych oraz informatyki poprzez innowacyjne strategie obliczeniowe.

Niniejsza praca doktorska prezentuje rozwój i walidację kilku modeli obliczeniowych symulujących złożone procesy biologiczne na różnych skalach. Celem tej dysertacji jest po pierwsze wykazanie, że modele obliczeniowe mogą dokładnie odtwarzać i przewidywać złożone systemy biologiczne na różnych skalach; po drugie zilustrowanie konieczności zastosowania różnorodnych podejść do modelowania różnych zjawisk biologicznych; oraz po trzecie, pokazanie, że modele matematyczne można wykorzystać do walidacji lub kwestionowania istniejących teorii biologicznych oraz identyfikacji obszarów wymagających dalszych badań.

Przedstawiam trzy modele specyficznych zjawisk naturalnych, które zostały zwalidowane na podstawie danych empirycznych. Obejmują one dyskretny model formowania wzorca naczyniowego w Arabidopsis thaliana, ciągły model długodystansowego przesyłania sygnału w drzewach oraz zaawansowaną hybrydową symulację pożarów lasów. Wyniki potwierdziły postawione założenia oraz pozwoliły ocenić przydatność stosowanych paradygmatów modelowania w różnych scenariuszach. Odkrycia podkreślają kluczową rolę interdyscyplinarnego podejścia w poszerzaniu naszej wiedzy.

Contents

List of Figures

List of Tables

Chapter 1

Introduction

This thesis presents how a computational approach can extend our comprehension of natural phenomena across multiple scales, employing a blend of mathematics, computer science, and biology. By adopting a computational lens, we aspire to uncover the universal principles governing these systems, drawing parallels with the precision and quantitative rigour of the 'hard' sciences.

My approach is inspired by the philosophical notion that biology, much like physics, can be abstracted through mathematical modelling to reveal underlying laws and patterns. The history of physics indicates how employing formal descriptions can be beneficial to advances in science. For instance, the development of integral calculus was essential in the formulation of classical mechanics. Similarly, introducing differential equations offered a framework for modelling dynamic systems, allowing us to create models describing phenomena such as electromagnetism or quantum mechanics. The shift from the natural language description to the axiomatic notion of mathematics in physics marked a breakthrough not only for physics but civilization as a whole.

This paradigm, leveraging mathematical models to distil complex phenomena into understandable principles, holds immense promise for the 'softer' natural sciences, such as biology or earth sciences. These fields, characterized by their intricate web of variables and interactions, stand to gain significantly from adopting a similar methodological stance. A pioneering effort in this field was a description of reaction-diffusion systems by Alan Turing [62]. Turing proposed a mathematical model of morphogenesis that demonstrates how simple interactions between chemicals could give rise to various patterns such as fur stripes and spots. Turing's work didn't simply show this, rather he laid the groundwork for the rise of mathematical biology [17]. However, in contrast to physics, biological systems perform tasks such as growth or self-healing, that are difficult to describe in a similar framework. These systems build upon the physical and chemical processes down to molecular or even quantum level, like in photosynthesis, which makes modelling large scale phenomena from first principles impossible to simulate on current hardware. Therefore they require an elevated level of abstraction and the development of novel mathematical tools tailored to their unique problems. The path forward necessitates a symbiotic relationship between empirical discovery and theoretical innovation, where new mathematical models are both inspired by and instrumental in advancing our understanding of nature.

This dissertation exemplifies the interdisciplinary potential of computer science by integrating mathematical modeling and empirical biological data, showcasing how computational methods can provide new insights into scientific questions.

In our prior work ‘Formal description of plant morphogenesis’ [45], we discuss a wide array of mathematical modelling methods in biology. This thesis is an extension of that work. My objective of this dissertation is to carefully evaluate and further develop mathematical and computational methods for studying natural phenomena. The central hypotheses of this thesis are:

1. Computational models can simulate complex biological systems.
2. Different modelling approaches are necessary to address the unique challenges presented by different biological phenomena.
3. Modelling can be used to assess hypothetical biological mechanisms and discover areas where more comprehensive research is needed.

To address them in the following chapters, I conduct a detailed exploration of computational models using diverse mathematical formalisms studying distinct biological phenomena. Each chapter is dedicated to a unique natural phenomenon modelled using specific mathematical approach, crafted to model. These models are rigorously based on empirical data and were developed in collaboration with specialists from relevant fields.

The phenomena studied cover a wide range of spatial and temporal scales, from cellular-level growth to the dynamics of entire ecosystems, and span time scales from minutes to months. This diversity requires a variety of modelling approaches such as discrete modelling with agents, where we considered a finite amount of objects interacting with each other, or a continuous model defined by partial differential equations, and hybrid approaches where I combined discrete geometry with continuous models of dynamic signalling.

Chapter 2 presents a discrete model of vascular pattern formation. This project aims to study the vascular pattern formation in the apical meristem of Arabidopsis Thaliana. Pattern formation is observed by looking at incipient veins - paths formed by the expression of the hormone auxin. I use an agent-based approach to simulate the emergence of developing veins: I place an agent in a 3D vector field that dictates its movement expressing various developmental hypotheses of vein formation. The model replicated the formation of the pattern and revealed the change in the meristem growth rate as a possible reason for the change in the phyllotactic pattern.

Chapter 3 describes a model of long-distance signalling in large plants. This model combines a discrete description of tree geometry with a continuous formulation of signalling to investigate if variations in tree architecture contribute to differences in the auxin gradient along the tree stem. In response to this question, I propose a simplified model of polar auxin transport in trees, represented as a directed graph with all edges aligned toward the root and controlled by a series of differential equations describing the rate of transport and auxin production.

Chapter 4 focuses on the phenomena of wildfires at an environmental scale. Simulating combustion is a difficult task, to achieve results in real-time that requires a highly efficient simulation. To achieve this I propose a hybrid approach which consists of several components that describe heat transfer and combustion for vegetation, atmosphere and several distinct ground layers. It builds upon Hädrich et. al. [20]. The original work did not account for the moisture in trees and fuel accumulated in the understory and ground, which limits its predictive capacity. To extend upon this work, I added water content in the tree description and introduced additional components of ground layers as well. These additions were able to simulate more complex fire behaviour, which allowed the reproduction of various wildfire phenomena.

Chapter 2

Vascular Strands Formation in the Arabidopsis Shoot Apex

2.1 Introduction

The development of the vascular system within the shoot apical meristem (SAM) of vascular plants is a fundamental aspect of plant biology, integrating the generation of new organs with the establishment of a complex vascular network. The vascular system plays a pivotal role in organ function and development by supplying necessary nutrients and hormones. As plants continuously produce organs throughout their life, the vascular system must dynamically expand and reorganize in response to developmental cues and environmental factors.

The relation between organ formation at the SAM and vascular development has been a long-standing question in plant biology. Given that lateral organs, such as leaves, are supplied by vascular strands that are continuous throughout the shoot vasculature, the formation of organs and their spatial arrangement (phyllotaxis) generated at the shoot apical meristem (SAM) have to be coordinated with the establishment of new strands. Early morphological studies, observed that the precursor to vascular strands, the procambium, forms before the emergence of leaves, suggesting that vascular development is regulated by an internal signal independent of organ formation at the SAM surface. However, these studies did not account for the genetic regulators of organ initiation that might precede vascular development.

With the progress in molecular and imaging techniques, mechanisms of organ formation at the SAM have been revealed, with auxin as a central regulator of this process. Namely, it was found that the initiation of new organs is triggered by auxin accumulation at the SAM surface, as deduced from the local upregulation of the auxin transporter PIN-FORMED1 (PIN1) and the auxin-induced transcriptional reporter DR5 ([7], [50], [23]). Soon after auxin accumulation, PIN1-mediated basipetal auxin transport from the SAM surface towards pre-existing shoot vasculature induces the formation of a vascular strand (including the future midvein) that supplies a new organ ([58], [57]). This leads to a hypothesis that a signal (auxin) inducing this vascular strand derives from the SAM surface and then flows down towards pre-existing shoot vasculature. However, computer simulations show that basipetal auxin transport from the SAM surface by itself cannot connect to the pre-existing vasculature beyond a short distance ([6], [22]). Thus, to enable the connection, a hypothetical attraction factor diffusing from the pre-existing vasculature has been proposed. This evidence supports two main hypotheses: one suggesting that vascular development is driven by an internal signal and occurs independently of organ formation at the SAM surface, and the other indicating that vascular development is directly triggered by the formation of new organs, specifically through the action of auxin. Understanding these processes is crucial for insights into plant growth and development, offering potential applications in agriculture and plant science.

To investigate those hypotheses we did imaging the isolated Arabidopsis shoot apex with laser confocal microscopy deep enough to capture the earliest stages of vascular strand formation below the SAM. It is based on experimental data from more than 100 3D reconstructions of shoot apices from deep confocal microscopy scans at various developmental stages. These scans revealed narrow DR5-expressing strands (denoted as incipient vascular strands-iVs) corresponding to the localization of future vascular strands. We observe that these strands originate from previously established iVs and only later connect to the DR5 maxima at the surface, which is a strong argument for independent vein formation.

In this chapter, we will focus on the computational aspect of our work that evaluates these hypotheses. It is based on experimental data from more than 100 3D reconstructions of shoot apices at various developmental stages. We describe a data acquisition process and formulate a model based on the spatial self-organisation of strands which describes the development of a vascular network in growing tissue. Interestingly, most research done with confocal microscopy tends to discard the depth aspect of the images either by focusing solely on the organ surface or by merging/slicing the stacks. The depth component is essential to study the development of the vascular system. Therefore, our study required the development of new approaches for both image analysis and modelling.

Work presented in this chapter was created as part of the research project ‘A role of vascular system in plant patterning’ that was supported by the research grant SONATA BIS6 (2016/22/E/NZ3/00342) from the National Science Centre, Poland.

2.2 Related works

The formation and formation of vascular systems and auxin pattern formation are critical areas of study within biological modelling. The first models of auxin canalization date to 1980 ([39]). These models are based on differential equations of polar auxin transport (PAT). These works predominantly focus on 2D models that are modelling either leaf veins or close to meristem surface ([52], [58], [57], [6]), with few attempts of extending it to 3D [22].

2.3 Modelling approach

Our study focuses on the early stages of vein formation, which occur in deeper layers of an apical meristem. It is a novel problem, where we do not understand the processes that govern it. In contrast to previously mentioned works, we don't have other information than auxin concentration, such as polar transporter configurations. Additionally, the patterns we observe are more complex and varying. These facts led us to the conclusion that crafting a model based on PAT would require many hypothetical assumptions. This would render it hard to control and unreliable without further evaluation lies out of scope with current capabilities.

Instead, we describe the iVs dynamics as a discrete agent-based model. In this model, the extension of iVs is defined as the movement of the corresponding agent and iV is a result of this movement. This is a high-level descriptive model, the agents follow the behaviour of the iVs observed in confocal images over time without acknowledging the underlying processes of auxin transport as in PAT.

Although this high-level model does not describe molecular mechanics, it has proven predictive capabilities in mutants and variations that express unusual vascular patterns. Using this approach we could test various hypotheses after translating them into agent behaviour.

2.4 Incipient veins annotation

Computational analysis, modelling, and simulation required a mathematical description of the vascular system's geometry and topology. We decided to represent it as a set of polylines or a graph with points in 3D space. We call this structure a **skeleton graph** S. Formally, we define S as $S = (V, E, P, A)$, where V is a set of vertices, $E \subset V \times V$ is a set of edges, $P : V \longrightarrow \mathbb{R}^3$ is a positioning of vertices in 3D space and A is a set of functions of V and E describing properties of each vertex line or strand.

Recovering the geometry of incipient veins from confocal stacks brought a unique set of challenges. Incipient veins are marked by pDR5revV2:YFP (DR5 in short) reporter that localizes auxin, a hormone responsible for various processes related to growth. Consequently, there are maxima of DR5 that are not part of the vascular network, and distinguishing between them requires expert knowledge. Another challenge comes from the process of capturing scans. Although a confocal microscope can penetrate the tissue, deeper layers are less visible due to light absorption and are prone to artefacts. It is particularly challenging when incipient veins are between 50 and 150 µm deep from the surface. Those issues rendered the standard methods, such as morphological skeletonization, inefficient.

Manual annotation

We developed software for manual annotation. In this program, the user manually selects points on the stack and connects them into lines. It consists of two windows: one displays a single horizontal slice of the stack, and the other shows a 3D view of the whole stack. A view of a single slice allows for fast and accurate annotations of points on vascular strands, while the second presents all points and lines, which helps in connecting them properly. The application was developed with Python and wxWidgets.

Similar results can be achieved with a combination of already available software, but creating dedicated software drastically accelerated the process.

Semiautomatic Annotation: An Agent-Based Model

Based on the results from manual annotation and insights into the process of annotating itself, we devised a semiautomatic solution employing an agent-based model. This method works locally, a user selects the initial position and direction of an agent at the beginning or end of an incipient vein. The algorithm works iteratively, moving the agent according to the calculated direction through the incipient vein with the purpose of staying close to the center of the incipient vein. We trace its path to recover the shape of this vascular strand.

Direction calculation

The new direction is calculated as a weighted average of the previous direction and the normalized vector between the agent's position and the weighted center of mass of voxels detected as inside the strand and in front of the agent by the *detection function*. The weight of the previous direction is denoted as **inertia** and can be specified by the user.

The detection function assigns each voxel in the stack a weight between 0 and 1. Firstly, it filters voxels by field of vision, voxels are assigned values equal to the percentage of voxel volume inside the cone. We chose a cone as the shape of this field. The cone starts at the agent's position and points in the previous direction. It is parameterized by **angle** and **range**, which are parameters chosen by the user. Next, the weight is multiplied by the value based on the value of the auxin marker. The marker value should be similar to the value in the agent's neighbourhood. The weight is calculated by the formula:

$$\max(0,(0.3-|m_x-m_A|/m_A)/0.3,$$

where m_x is marker of voxel x, m_x is marker value in this voxel and m_A is agent's marker value.

Finally, to avoid discontinuities in the set of detected voxels, we run a flood-fill algorithm on non-zero voxels starting at the agent's position and assign 0 to all voxels outside the compact component.

Finally, to avoid discontinuities in the set of detected voxels, we run a flood-fill algorithm on non-zero voxels starting at the agent's position and assign 0 to all voxels outside the compact component.

Performance

The performance of our agent-based model primarily hinges on the number of voxels present within the field of view during each step of the algorithm. This number is directly proportional to the volume of the field of view. Mathematically, the volume V of this field can be given as:

$$\frac{2}{3}\pi r^3(1-\cos\theta),$$

where r represents the range and θ corresponds to half of the viewing angle. As evident, the complexity of the algorithm scales cubically with the range r. However, if calculation on a single voxel is simple we can achieve real-time performance even if the range is considerably large.

For optimal performance, we implemented step calculation using Cython, a Python-to-C compiler. We conducted a performance test on a laptop equipped with an Intel i7-8750H processor. For this test, we set the range equal to 40 microns and an angle equal to 120 degrees. Voxel dimensions were equal to 0.37 microns x 0.37 microns x 0.81 microns, which gives 82,200 voxels in the field of view on average. Our tests showed that a single step took 0.05 seconds on average without flooding implemented and increased to 0.6 seconds when the flooding algorithm was incorporated, which was still an acceptable value. It's worth noting that our implementation is single-threaded, which leaves room for significant optimization if needed.

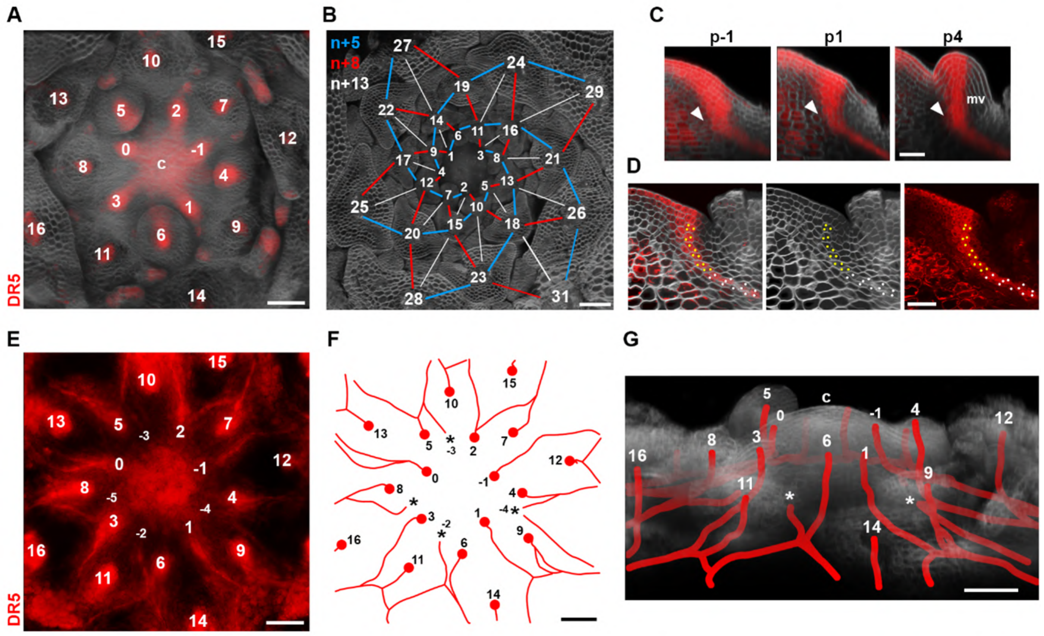

Figure 2.1 Figures A-E show confocal images of SAM. Vascular strands indicated by expression of DR5 are marked by red. Figures F and G present a skeleton reconstruction of iV system.

Other applications

The versatility of the agent model allows it to be adapted for detecting a variety of objects with similar structural characteristics. One potential application might be quantifying the morphological parameters, such as the length and width of a plant's stems or roots. The agent model can represent such an object using polylines or splines, which will be essential in parameter extraction.

Additionally, the agent model can also be employed for dynamic tracking, such as tracing the path of a moving cell. For this more unpredictable scenario, the agent's field of view can be modified from a cone to a ball. This modification allows the agent to center on the moving object, the agent would follow the centre of an object. Combining it with real-time tracking, with each step of the agent corresponding to a frame in a time-lapse sequence, the agent can effectively trace the paths that objects follow over time. This approach can be further enhanced by combining it with other techniques like cell segmentation or object detection to provide a more comprehensive and consistent analytical framework.

2.5 Incipient vein growth modelling

Introduction

Using the methods described earlier, we have successfully reconstructed the geometry of incipient vein networks in over 100 apical meristems. To accomplish this, we extracted over 30 skeleton graphs, comprising more than 100 emerging iVs and 200 pre-existing iVs. Incipient veins in these skeleton graphs are assigned integer numbers that correspond to the primordium to which they are connected. For instance, the youngest and the first primordium appearing as a bulge is denoted as $p1$, whereas incipient primordia are labelled as $p0$, $p-1$, etc. Additionally, we have adopted a similar notation for free-ending iVs, assigning them negative numbers based on their development and phyllotactic patterns. We later map those values to the age of an incipient vein.

We split a skeleton graph into vascular bundles. Those bundles are divided into emerging and pre-existing according to parameters in the reconstruction. Each pre-existing vascular bundle corresponds to a different primordium and contains that are connected to this primordium, whereas an emerging vascular bundle contains a single vein that, we predict, would connect to an unformed yet primordium.

Vascular bundle $G = (V_G, E_G, n_G)$ consists of a set of points V_G in 3D space and a set of line segments E_G with endpoints in V_G and n_G is a real number describing a pre-existing iVS's age. It can be considered as an undirected graph with embedding in 3D space or a collection of polylines. For a given skeleton graph, let G_p denote a set of bundles, that are considered pre-existing iVSs and G_e denote a set of bundles that are considered emerging iVSs.

We observe two intriguing patterns: initial free-ending iVs from two neighbouring pre-existing iVs often merge into one single iV. Furthermore, in younger meristems, an iV numbered n tends to emerge from iVs numbered $n+5$ and $n+8$, whereas in older meristems, they emerge from $n+8$ and $n+13$. Our goal is to reIn our first two models, we treat these merging iVs as two separate entities—one from the left and one from the right—effectively doubling our data set.

Analysis of these samples reveals two distinct phases in vasculature formation. In the initial phase, a new incipient vein (iV) emerges from a pre-existing one (parent vein) and extends over 100 microns towards the meristem center. Remarkably, this initial phase is independent of surface-derived auxin signalling. This phase occurs only in the narrow layer of cells with a cone-like shape that is approximately 50 microns below the meristem surface. In the subsequent shorter phase, iVs situated approximately 40 microns below the SAM surface connect to primordia, but only when surface auxin signalling of the corresponding primordium is present.

Intriguingly, our data suggests that the positioning of free-ending iVs within the vascular cylinder is correlated with the phyllotactic pattern before they connect to the incipient primordial. Despite appearances, this alignment does not rely on surface auxin signalling, but may instead depend on signals in inner tissues.

Existing studies have shown that pre-existing vascular strands can either attract or repel newly induced strands, depending on their relative auxin concentration. These observations lead us to hypothesize that auxin-mediated interactions between emerging iVs and neighbouring, pre-existing veins guide the extension of iVs. This process may represent a self-organizing phenomenon occurring within inner tissues. To explore this hypothesis further, we turn to tissue-level computational simulations to determine whether attraction-repulsion interactions can account for the observed shapes of iVs.

To model emerging iV extensions, we will once again use the agent-based method. The agent is defined by its position A_p and extension vector $\vec{A_E}$ In each step of the simulation $\vec{A_E}$ is updated according to the model logic and the A_p is moved by the vector $\vec{A_E}$. Consecutive agent positions are joined together as a skeleton graph which represents an emerging iVS in our simulation. The movement direction is determined by the modelled interaction between the agent and pre-existing iVs. Movement is restricted to a parametric cone that represents the area of incipient vein extension. Observations indicate that the shape of emerging iVs does not change significantly, they only extend further toward the center. Thus, this modelling approach serves as an acceptable approximation of the iV formation process.

Naive Random model

This subsection introduces a simplified model designed to investigate whether the shape of iVs can be exclusively attributed to acropetal extension without any interaction. In this model, the extension process of new iVs is represented as a random walk directed toward the meristem center.

The simulation requires several input parameters: the initial point of the iV where it begins to extend (p_S), the location of the meristem center (p_C) and the minimum distance (d_m) from the endpoint of the iV and the center p_C.

Initially, the agent is located at p_S. In each simulation step, the tangent vector $\vec{A_c}$ is set in a direction from the agent's current position to p_C. A second vector $\vec{A_n}$ is randomly chosen through uniform sampling from all vectors that are perpendicular to $\vec{A_c}$. Then, an extension vector $\vec{A_E}$ is calculated with formula $v = \text{slerp}(\vec{A_c}, \vec{A_n}, s)$, where the s is a random

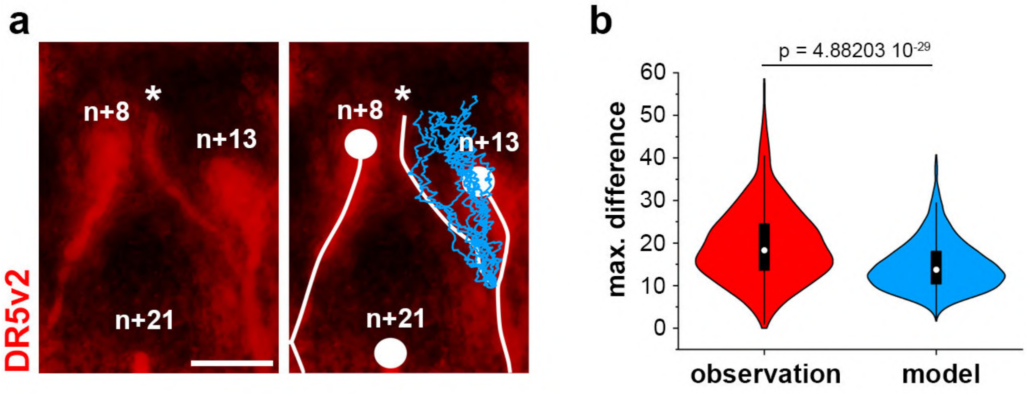

Figure 2.2 Figure (a) depicts a fragment of a confocal stack with DR5v2 marker in red. White lines depict iVs in white and emerging iV is marked by a star. Blue lines represent results from random walks. Figure (b) presents violin plots of maximal distance between emerging iV or random walk and pre-existing iVs.

value sampled from a normal distribution with $\sigma = 1/3$ and $\mu = 0$. Finally, the agent's position A_p is updated translating it along the vector $\vec{A_E}$.

The simulation continues until the distance from the agent to the center p_C falls below the predefined minimum distance d_m.

We compared sets of generated random paths and the original emerging incipient veins. First, for each free-ending iV, we identified a branching point from its parent vein and calculated the distance from its tip to the meristem center; as respective parameters p_S and d_m to create corresponding random walks. This resulted in sets of paths random and original. Then, we use the Hausdorff distance between an iV (or a random walk) and their parent vein as a statistic for comparison. A two-sample Kolmogorov-Smirnov test yielded a p-value of 0.0075. Thus, we conclude that the extension of emerging iVs is not purely stochastic but might be influenced by attraction-repulsion interactions during their development.

Incipient vascular strand model (iVSM)

To further investigate the role of attraction-repulsion interactions in iV extension, we introduce a self-organizing model that incorporates attraction-repulsion dynamics to simulate emerging iVs. As before, we place an agent at the start of emerging iV, that moves towards the center and stops. Unlike the previous model, where the movement was random, this model introduces an interaction function. This function dictates how the agent behaves in relation to pre-existing iVs. It is important to note that the scope of this model is limited to simulating local interactions on a short timescale of a few hours. Consequently, this does not consider other factors such as tissue growth or interaction with the meristem tip.

For each emerging iV, the initial agent's position A_p is set to the starting position p_S. In each simulation step, we update the current position A_p and the extension vector $\vec{A_E}$. The agent's position A_p is updated by adding $\Delta t\vec{A_E}$ to A_p and projecting to the growth cone (Δt is some small value). The simulation continues until the distance from A_p to p_C is less or equal to d_m. Consecutive agent positions are connected to form a polyline, which represents an emerging iV in our simulation.

Parametric cone as extension region

We observed that the initial phase of this extension occurs within a thin layer around 50 microns deep. To capture this biological constraint we limit agent movement to this region, approximated as a parametric cone. The cone is characterized by four parameters: d (distance from the meristem tip), T (tangent of the cone angle), and A_1, A_2 (tangents of the rotation around X and Y axis rotation; these are essential due to the slight rotation in confocal scans).

The equation for this cone, considering the meristem tip as the origin of the coordinate system, is:

$$z = -T \cdot \sqrt{(x + d * A_1)^2 + (y + d * A_2)^2} + A_1 \cdot x + A_2 \cdot y - d$$

For each confocal scan and its corresponding skeleton graph, we calculate a different set of these parameters to minimize the average squared distance between the parametric cone and the segments of IVs developed in the first phase.

Extension vector calculation

The extension vector $\vec{A_E}$ is calculated as the linear combination of the previous extension vector $\vec{A_E}$ and a set of interaction vectors. These interaction vectors capture the influence exerted by primordia and neighbouring pre-existing iVs on emerging iV. Specifically, we propose that neighbouring vascular bundles and primordia can either repel or attract emerging incipient veins. Formally, an interaction vector is defined as a unit vector directed from the agent's position to the closest point on a vascular bundle Gp_i multiplied by a function depending on the distance between those two points. We assume that distant vascular bundles cannot noticeably influence the extension direction of emerging iVs thus we ignore all vascular bundles at a distance greater than max_D.

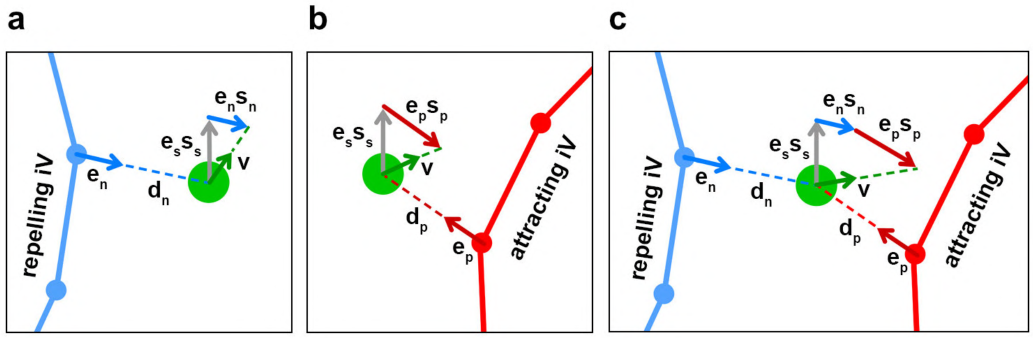

Figure 2.3 Figure shows schematically how a new extension vector is calculated in the case of single repelling iV (a), attracting iV (b), attracting and repelling iVs (c).

The new extension vector $\vec{A_E}$ is calculated using the following equation:

$$\vec{A_E} = \text{normalize}(s_A \vec{A'_E} + s_c \vec{v_c} + s_1 \vec{e_1} + \cdots + s_n \vec{e_n}), \tag{2.1}$$

where s_A is an inertia parameter, s_c and $\vec{v_c}$ represent the strength and direction of attraction to the meristem center. $\vec{e_i}$ is a unit vector directed from the agent's position to the closest point on the vascular bundle $G_{p,i}$, and s_i represents the strength of interaction between $G_{p,i}$ and the agent. s_A, s_c are parameters of the model, while s_i are results of the interaction function.

Incipient vascular strand model (iVSM)

The interaction function encapsulates attraction-repulsion behaviour. For different results shown in this paper, we employ the interaction function with a set of parameters. An example plot of the interaction function is shown in Figure 2.4 shows an example plot of an interaction function. The triangularly shaped graph allows for expressing repulsion at shorter distances and attraction over longer distances. However, the graph can be shifted in the negative horizontal axis direction to reflect a lack of a repulsion effect (Figure 2.4 c) representing, for example, still-growing veins. The function incorporates several parameters:

- negative range (r_n) – range of negative interaction (repulsion),
- positive range (r_p) – range of positive interaction (attraction),
- negative strength (s_n) – strength of negative interaction (repulsion),
- positive strength (s_p) – strength of positive interaction (attraction),
- peak coefficient (p_p) – peak of positive interaction.

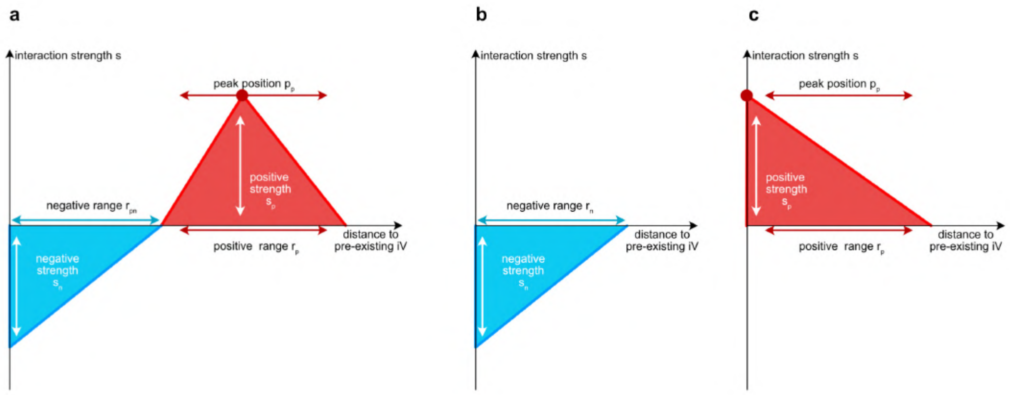

Figure 2.4 Figure (a) shows the interaction function on a plot, with its parameters, figures (a), (b) show how by modifying parameters of the interaction function it can express only repulsion or only attraction.

- age modifier (a_m) – extends the range of negative interaction with vein age,
- age cutoff (a_{min}) – minimal age for negative interaction to have effect.

For given bundle $G_{p,i}$ it takes its age a_i and the shortest distance d_i between the agent and the bundle. Initially we determine the age-modified negative range $r_{n,i}$ as follows:

$$r_{n,i} = r_n \sqrt{\max(0, a_m \cdot (a_i - a_{min}))}, \tag{2.2}$$

The value of the interaction function s_i is calculated according to the following equation:

$$s_i(d) = \begin{cases} -s_n \cdot (1 - \frac{d}{r_{n,i}}) & \text{if } d \leq r_{n,i}, \\ s_p \cdot \frac{d - r_{n,i}}{p_p \cdot r_p} & \text{if } r_{n,i} < d, \leq r_{n,i} + p_p \cdot r_p, \\ s_p \cdot (1 - \frac{d - (r_{n,i} + p_p \cdot r_p)}{(1 - p_p) \cdot r_p}) & \text{if } r_{n,i} + r_p < d. \end{cases} \tag{2.3}$$

Parameter optimization

To optimize the model's predictive accuracy, we developed a parameter-tuning strategy. Provided the set of parameters s_A, s_c, r_n, r_p, s_n, s_p, a_m and a_{min}, we evaluate their suitability by running the model for all emerging iVs in the dataset. Each simulated iV $L_a = (p_{a_1}, p_{a_2}, \cdot, p_{a_n})$ with the corresponding incipient vascular strand G_e using distance value defined as follows

$$d(L_a, G_e) = \max\left(\left\{d(p, G_e)^2 : p \in L_a\right\}\right) + \text{end\_distance}, \tag{2.4}$$

Algorithm 1: Algorithm for calculating iV based on iVSM

```
Input: Set of pre-existing iVs $\mathcal{G}_P$, Starting position $p_S$, Center position $p_C$, Distance margin $d_m$, Maximum influence distance $\max_D$
Output: Simulated iV polyline
Initialize: Set initial agent's position $A_p$ to starting position $p_S$.
Initialize: Set initial extension vector $\vec{A_E}$ to $\vec{0}$ vector.
Initialize: Initialize empty list $L_a$.
repeat
    Update $A_p$ by adding $\vec{A_E}$ to $A_p$.
    Calculate distance from $A_p$ to $p_C$.
    if distance $\leq d_m$ then
        Stop the simulation.
    end if
    for $G_{p,i} \in \mathcal{G}_P$ do
        Calculate vector $e_i$ and value $s_i$ using Equation 2.3
    end for
    Compute the new extension vector $\vec{A_E}$ using Equation 2.1.
    Update $\vec{A_E}$ to the newly computed value.
    Project agent's position $A_p$ to growth cone.
    Add agent's position $A_p$ to $L_a$
until simulation stops
Return $L_a$
```

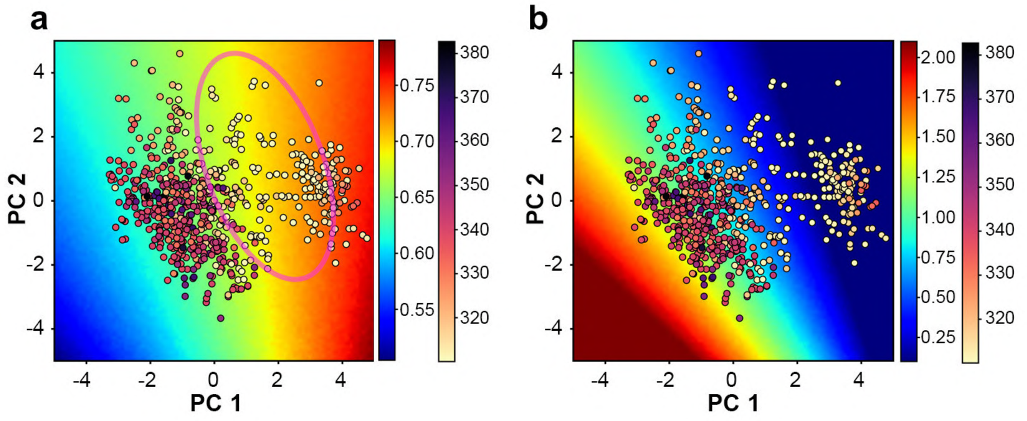

Figure 2.5 Figures show the best parameter sets projected to the plane spanned by the first two principal components. Each point refers to one parameter set, and its colour represents the value of the cost function. Pink oval marks approximate region with low cost-function value. The underlying scatter plots represent values of parameters in the plane; in Figure (a), it represents the ratio between negative strength and attraction to the center, while in Figure (b), positive strength.

where end_distance represents the squared distance between the endpoint of the emerging iV and p_{a_n}. $d(p, G_e)$ is the smallest distance between a point p and G_e. We aggregate all $d(L_a, G_e)$ values into a single metric $D(s_A, s_c, r_n, r_p, s_n, s_p, a_m, a_{min})$ by calculating the root mean square.

As the cost function is non-differentiable, the optimization method could not rely on the function's gradient. Our strategy can be divided into two steps. Initially, we explored 9-parameter space by sampling 100,000 combinations uniformly distributed in probable range. The most promising combinations were further refined using a random search. This method iteratively samples cost function values around a current position in parameter space and moves towards the point with the lowest cost, dynamically adjusting the search radius based on performance. The method stops after a predefined number of steps or if it cannot find a better position.

We obtained 600 combinations of parameters with cost function values ranging from 320 to 380. These are visualized as an 8D point cloud as reduced to a 2D scatter plot through Principal Component Analysis (PCA) as shown in Figure 2.5. The first two principal components explained 41% and 21% of the variance, respectively. Further exploration of this reduced parameter space led to optimized results, with the lowest cost function value recorded being 309. PCA analysis revealed a region in the parameter space characterized by low cost-function values, indicating the stability of our model.

Analysis of the parameter space led to interesting conclusions. Specifically, there is an area with the lowest distance, as marked in Figure 2.5. The area of lowest error has an attraction lower than 0.1. While the repulsion coefficient varies between 1.2 and 2.5, similarly attraction to the meristem center varies between 2 and 3.3 however, the ratio between those two is 0.75 in most of the results. Other parameters have stable values: age coefficient around 0.1, age cutoff 1, negative range 45. The positive range and peak coefficient are not important, because they are bound attraction, which is too weak.

Additionally, we evaluated the importance of limiting the area of extension to the cone, by running optimization without this assumption. The received parameters promoted only long-distance (approximately 100 microns) attraction, which is not probable from the biological perspective. We conclude that the extension of incipient veins is likely driven by either repulsion or an attraction-repulsion dynamic.

Variable Name	r_n	r_p	s_n	s_p	s_A	s_c	p_p	a_m	a_{min}
Value	59.225	0.0	2.787	0.0	0.5	3.062	0.99	0.039	0.896

Table 2.1 Parameter acquired from optimization

Global Incipient Vascular Strand Model

The Global Incipient Vascular Strand Model (GiVSM) extends the capabilities of the Incipient Vascular Strand Model (iVSM) by representing vascular formation in the meristem globally in the long term. While iVSM primarily addresses local interactions between neighbouring iVs, the GiVSM aims to simulate the comprehensive growth of the vascular system throughout the vegetative phase. To accomplish this the GiVSM integrates several additional processes and phenomena, including tissue growth, which pushes iVs and primordia away from the center, giving a place for new to appear. It also accounts for the emergence of new iVs from pre-existing ones, as well as, the second phase of iVs, which is the process of connecting to the primordium.

In the GiVSM, we differentiate between emerging vascular bundles (eVB) and mature vascular bundles (mVB). The latter is analogous to the pre-existing iVs in the iVSM. the growth of eVB is governed by the iVSM model, utilizing the most optimised parameter set. When an eVB comes close enough to the center, its extension halts and awaits the emergence of primordium near its endpoint. Primordia appear at regular intervals, known as plastochrons. They are situated at a predefined distance to the center while respecting the phyllotactic angle. Upon connecting to a primordium, it transitions into an mVB. Subsequently emits two new eVBs after a specified amount of time. Throughout the simulation, tissue growth displaces mVBs away from the center, thereby creating space for new bundles to emerge. Similarly to iVSM, the simulation is confined to a parametric cone, with the center located under the meristem tip and the spanning angle determined empirically based on confocal stacks.

Formally, vascular bundles are represented as a skeleton graph with additional information such as age, growth stage or index. Each eVB also has an agent that is responsible for its extension. The simulation is conducted in a discrete-time domain. Each simulation step represents 20 minutes of meristem growth. In each step, we apply tissue growth and extension of eVB as well as increase the age of all the vascular bundles and primordia. Tissue growth moves all vertices (including agents) away from the meristem center. This movement is modelled by a tissue growth function. This function is a quadratic approximation of distance from the meristem center with respect to time, as further described in tissue growth approximation.

The extension moves all agents by a distance equal to the **extension rate** and in the direction dictated by the process described in iVSM. The agent is additionally attracted to other eVB by **emerging attraction** if the distance to it is smaller than the **attraction threshold**. After agents move to a new position, we consider several cases. If this position is closer than the **bundle merging threshold** to another eVB B, then the agent is removed and the eVBs are merged. The EVB A is connected to the eVB B by connecting the last agent's position with the vertex closest to the new agent's position in bundle B. If the distance is less than the **primordium connection distance** to the new primordium (i.e. one that no bundle has connected to), it will connect to the primordium and begin maturation. If neither of the aforementioned conditions is met, the new agent's position is added to its emerging bundle and connected to its previous position. To prevent reaching the meristem center, we cancel bundle extension if it would be closer to the center than **center distance threshold**.

In addition, we assess at each step whether a new eVB or primordium will appear. mVBs emit either left or right eVB immediately after reaching the **left bifurcation age** or **right bifurcation age**, respectively. It emerges **bifurcation distance** away from the interconnection point on a left or right branch respectively.

New primordia are introduced independently of iVs at each **plastochron** with the initial development stage described by the **initial primordium stage** value The radial position of new primordia relative to the apex center is defined by **center distance threshold** and the angular distance from the final position of the previous primordium is equal to the **divergence angle**. Once the primordium is introduced, it awaits a free-ending iV that will be in **primordium connection distance** evaluated in radial coordinates. If the positions of the primordium and iV endpoint do not overlap the primordium position is changed to the iV endpoint. This new position of the primordium is used in calculating the next primordium

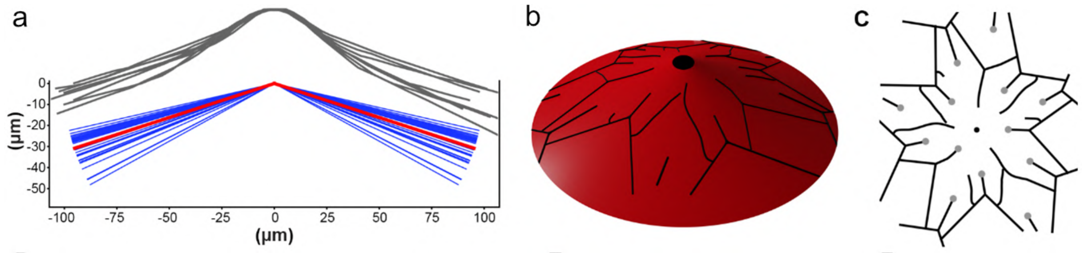

Figure 2.6 (a) Computation of the vascular space for the GiVSM. Individual reconstructions of real iV network were used to compute cone-shaped surfaces (blue) from which an averaged surface was obtained (red), serving as the vascular space in the simulations. n = 30 iV reconstructed networks. For comparative purposes, the shoot apex surface silhouettes are presented above (grey lines). n= 10 apices.
(a, b) Illustration of the vascular space with overlaid iV network (b) and a top view on an exemplary simulation of expanding iV network (c). The cone-shaped space is in red, simulated iVs are represented by black lines. Free-ending iVs emerge from pre-existing iVs. The connection of pre-existing iVs to the DR5 maxima on the SAM surface is denoted by grey dots. The apex center is indicated by a black dot.

position. It enables us to avoid cumulative error, for example when the divergence angle from the GiVSM is different than the surface divergence angle.

Primordia serve as a synchronizer in our simulation. Based on the **initial primordium stage** we calculate the time left to reach stage P0, which is denoted by **maturing time**. As time progresses, this maturing time decreases to indicate primordium growth. When an eVB connects to primordium, it inherits the maturing time of this primordium. The bundle matures after the maturing time passes. It is then transformed into mVB and we start counting time to bifurcation. This approach together with a wide angular threshold allows us to control the divergence angle with an GiVSM while the temporal aspect of transforming free-ending iV into preexisting is controlled by the primordia at the SAM surface

Tissue growth approximation

Tissue growth moves primordia away from the meristem tip. We assume that the speed of this movement is dependent solely on the distance to the meristem center and that iVs are affected by it at the same rate as primordia. To approximate it, we considered each of the three meristem stages separately. From all meristems of the given stage, we collected information about every primordium's age and their distance to the center. We used the least mean square method to fit the quadratic function $f(t) = A * r^2 + B * r + C$ to the relationship between age and distance. Although we examined different functions like exponential or linear, the quadratic yielded the lowest error.

During each simulation step, we analytically calculate the post-growth position for every point of every vascular bundle. Given a point p we calculate a radial distance r between p and meristem center. Then, we calculate the inverse function

$$t_p = g(r) = f^{-1}(r) = -b + \frac{\sqrt{(b^2-4ac)}}{2a}. \tag{2.5}$$

Finally, we compute a new radial distance $r' = f(t+\Delta t)$ and move point p away from the meristem center by $r' - r$.

Algorithm 2: Single Step Simulation of Global Incipient Vascular Strand Model (GiVSM)

```
Input: Set of mature incipient vascular bundles $\mathscr{P}_{MVB}$, set of emerging incipient vascular bundles $\mathscr{P}_{EVB}$, set of primordia $\mathscr{P}$, meristem center $p_C$, and simulation parameters $SP$.
Output: Updated sets of $\mathscr{P}_{MVB}$, $\mathscr{P}_{EVB}$, and $\mathscr{P}$.
Apply Tissue Growth:
for each point $p$ in $\mathscr{P}_{MVB} \cup \mathscr{P}_{EVB}$ do
    Calculate new position considering tissue growth.
end for
Extend Emerging Incipient Vascular Bundles:
for each $P_{EVB}$ in $\mathscr{P}_{EVB}$ do
    Calculate extension vector $\vec{A_E}$ using iVSM logic.
    Update $P_{EVB}$ append new agent position and check for connection criteria.
    if $P_{EVB}$ connects to a primordium in $\mathscr{P}$ then
        Start maturing of $P_{EVB}$.
        Stop extension of $P_{EVB}$.
    end if
    if $P_{EVB}$ meets merging criteria with another $P'_{EVB}$ then
        Merge $P_{EVB}$s and update $\mathscr{P}_{EVB}$.
    end if
end for
Introduce New Primordia and Incipient Vascular Bundles:
if conditions for new primordium introduction are met then
    Create new primordium and add to $\mathscr{P}$.
end if
for each $P_{MVB}$ in $\mathscr{P}_{MVB}$ ready to bifurcate do
    Emit new $P_{EVB}$s according to bifurcation logic.
    Update $\mathscr{P}_{EVB}$ with new $P_{EVB}$s.
end for
Update Ages and Stages:
for each entity in $\mathscr{P}_{MVB}$, $\mathscr{P}_{EVB}$, and $\mathscr{P}$ do
    Update age and proceed to next developmental stage if applicable.
end for
Return updated $\mathscr{P}_{MVB}$, $\mathscr{P}_{EVB}$, and $\mathscr{P}$.
```

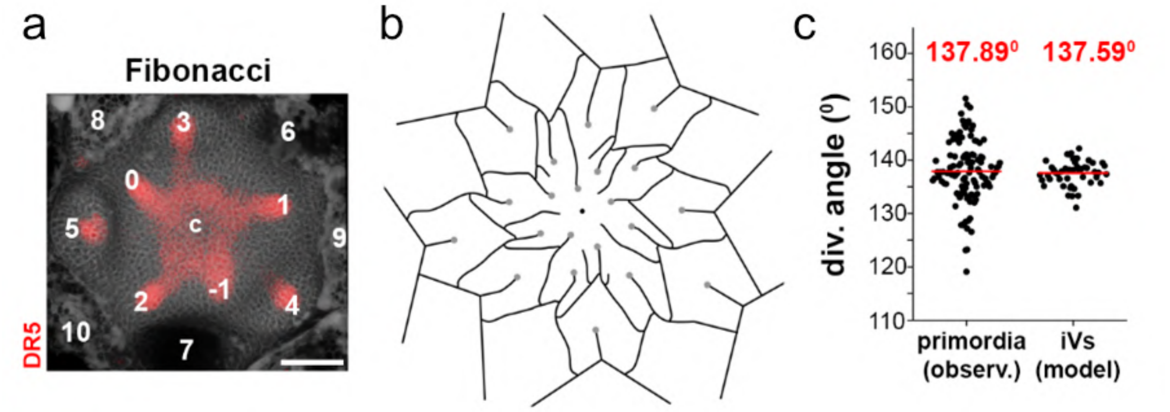

Figure 2.7 (a) Exemplary shoot apex displaying Fibonacci phyllotactic pattern. The DR5 expression (red) marks incipient and existing leaf primordia. c, the SAM surface.
(b) Simulation of iV network development according to Fibonacci phyllotactic patterns. Grey dots, connections to the surface; a black dot, apex center.
(c) Divergence angles measured between successive real primordia (left) or simulated iVs (right). Red lines and numbers, mean; black dots, data. The iV angles were measured between iVs just before and after their connection to the surface (two-sample t-test, p=0.7273). In (c) n=111 p1-p2 primordia, for model n=48 iVs;

2.6 Model validation and results

In this section, we explore the predictive capabilities of **Global Incipient Vascular Strand Model**. We start with validating it against skeleton graphs acquired from confocal microscopy. Unlike with iVSM validation, we cannot do direct comparisons as we simulate the growth of a whole vascular system over 20 days, which is impossible to document in a timelapse scan. Therefore, we examine whether the model-generated skeletons faithfully replicate the expected features and dynamics of vascular development.

In the analysis of empirical data, we observe that iVs are situated beneath the primordium before its manifestation. To ascertain the fidelity of our model, an initial verification was conducted to determine whether this fundamental characteristic could be accurately reproduced. As demonstrated in Figure 2.7, the comparison reveals that the model's average phyllotactic angle deviates by merely 0.3 degrees, accompanied by a significantly reduced variation. Based on these findings, it is concluded that our model replicates the empirical observations with a high degree of precision.

Another feature validated in this model is the transition from M-type interconnections to R, and ultimately, to R+M patterns, as depicted in Figure 2.8(e,f). In small meristem, new iVs emerge according to pattern M (2.8(c)). They emerge from two iVs attached to primordia $n+5$ and $n+8$ connect and finally connect to primordium n. As meristem grows

Table 2.2 Parameters for Small, Medium, and Large meristem Stages. Values that change with stages are written in bold

Parameter	**Small**	**Medium**	**Large**
Extension rate (µm/h)	3.50	4.00	5.00
Emerging attraction	0.15	0.15	0.15
Attraction threshold (µm)	18.000	18.000	18.000
Bundle merging threshold (µm)	4	4	4
Primordium connection distance - radial(µm)	2.000	2.000	2.000
Primordium connection distance - angular (deg)	25.0	25.0	25.0
Center distance threshold	48.00	52.66	60.63
Plastochron (h)	13.00	10.00	8.000
Initial primordium stage	-1.000	-1.000	-2.000
Divergence angle	137.2	137.2	137.2
Left bifurcation age	13	45	40
Right bifurcation age	39	20	16
bifurcation distance	28	28	28
Tissue growth a	0.0015	0.0017	0.0019
Tissue growth b	0.54	0.64	0.74
Tissue growth c	46.00	50.66	58.63

and becomes medium we observe a switch to R and R+M pattern (2.8(d)), in this case *n+8*-derived emerging iV attaches to primordium *n* before connecting with other emerging iV. After that, *n+5*-derived emerging iV is repelled from it instead of connecting (probably due to the supply of auxin coming from the surface) establishing the R pattern. Instead of connecting id grows further and attaches to the next *n-8* primordium, while iV connected to *n* releases a new iV that connects to it establishing an R+M pattern. Eventually, in the large meristem, new interconnections are made only according to the R+M pattern.

Each distinct stage of meristem development: small, medium and large is characterized by different values for certain characteristics, such as the time interval between plastochrons and lateral growth rate. We set the simulation parameters for each stage based on empirical data acquired from the confocal scans. We also calculated an average time for each stage to be reached. The simulation starts from a template of an initial stadium of a small meristem (2.8 a). During the simulation, we use a linear approximation for these parameters to model the gradual transition from one state to another. Table 2.2 contains all parameters of GiVSM for each stage. As can be observed in the figure 2.8, GiVSM follows correctly the aforementioned change from M to R+M pattern.

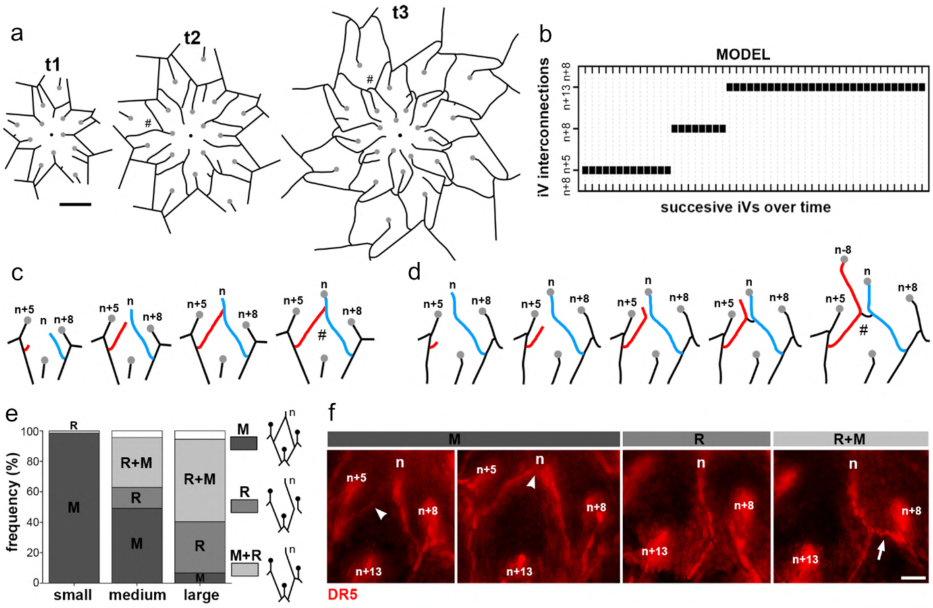

Figure 2.8 (a) Simulation of iV network development. The simulation initiates from a template (t1 = 1 h). Over time (t2 = 85 h, t3 = 314 h), free-ending iVs emerge from pre-existing connected iVs (grey dots). A black dot, apex center; hash, iV patterns at t1 and t2, whose generation is illustrated in (c) and (d), respectively.
(b) Progression of simulated iV interconnections in relation to parastichy order over 480 hours. The interconnections were determined in iVs after their connection to the SAM surface.
(c, d) Simulation illustrating the generation of different iV interconnection patterns over time. In (c), representing the M pattern, two iVs (n, blue and red) merge before connecting to the SAM surface. In (d), representing R and R+M patterns, the n+8-derived iV (n, blue) connects to the surface and repels the n+5-derived iV (red), which further extends and eventually connects to the surface (n–8). Another iV (black) links the n and n-8 iVs. Grey dots, connections to the surface; hash, iV patterns shown at (a).
(e) Frequency iV interconnection patterns in real small, medium, and large apices. Schematic representations of M (dark grey), R (grey), and M+R (light grey) patterns are shown on the right (n, iVs forming different pattern types). White bar, patterns with n+8-derived iVs. n= 29 (small), 36 (medium), and 35 (large) apices (iV stages from -5 to 3 were analysed in each apex).
(f) Sections through selected sites of shoot apices representing M, R, and M+R patterns with respect to parastichy order. Arrowheads indicate the n+5-derived iV before and after its merging with the n+8-derived iV. An arrow points to an iV linking n and n+8 iVs.

Repulsion strength

After establishing the GiVSM's capability to replicate key developmental phenomena in vascular formation, we examine model sensitivity to parameter changes. Specifically, we focus on how modification of tissue growth speed and repulsion strength influence when changes in interconnection patterns occur.

We ran the GiVSM 6 times gradually changing repulsion strength s_n (from $s_n = 1.7$ to $s_n = 4.2$ increasing it by 0.5 for each simulation. As observed in figure 2.9 despite changing the value of s_n by ±18.5%, ±37%, and ±55% relative to the optimal value maintain phylotactic angle (fig. 2.9(b)) as well as the switch of iV interconnection pattern. There is only a slight change in the switch of these patterns over time under different s_n values (indicated by asterisks for merging and by hush symbol for repulsion) (fig. 2.9(b)). As we can see this shift occurs later when repulsion strength is lower and earlier when repulsion strength is higher. This is probably caused by the change in the merging point. Higher repulsion strength causes it to be further from the center, which in turn moves the starting position of the new iV further to the center (as the interconnection position controls it). It causes n+5 to be too far away from n+8 to merge with it before maturation.

We also examined the extreme value of repulsion strength $s_n = 0.7$ (fig. 2.10). In this simulation, repulsion is too low for the iVs to merge, preventing the proper establishment of iV interconnections. This produces a very different pattern. Specifically, under a low repulsion, iV extension is predominantly subjected to acropetal attraction towards the apex center. In consequence, emerging iVs follow nearly straight trajectories, and remain closer to pre-existing iVs compared to the original simulation, where iV trajectories are more curved, and iVs extend further from the pre-existing iVs. This shows that the trajectory of iV extension, driven by repulsion interactions with other iVs, plays a crucial role in the iV patterning.

Given that PIN1 is highly expressed in domains where vascular strands are formed (Scarpella et al. 2006; Bayer et al. 2009) and suppression of polar-auxin transport leads to disruption of the vascular pattern in stems and leaves (Galweiler et al. 1998; Banasiak et al. 2018; Mattson et al. 1999; Verna et al. 2019), we infer that the interaction between iVs may depend on PIN1-mediated auxin transport. According to such a scenario, the pin1 mutant, in which PIN1 expression is suppressed, may represent a system with lower repulsion to test the prediction from our model. Because the DR5 signal in iVs at vegetative pin1 apices is extremely low, we imaged the inflorescence stems, where the DR5 expression allows for the reconstruction of the iV network. As predicted, in pin1 mutant iVs extend along nearly straight trajectories forming a parallel iV arrangement of high density, while the iV network in the WT is characterized by curved iV trajectories and gaps between iVs (fig. 2.10 d, e).

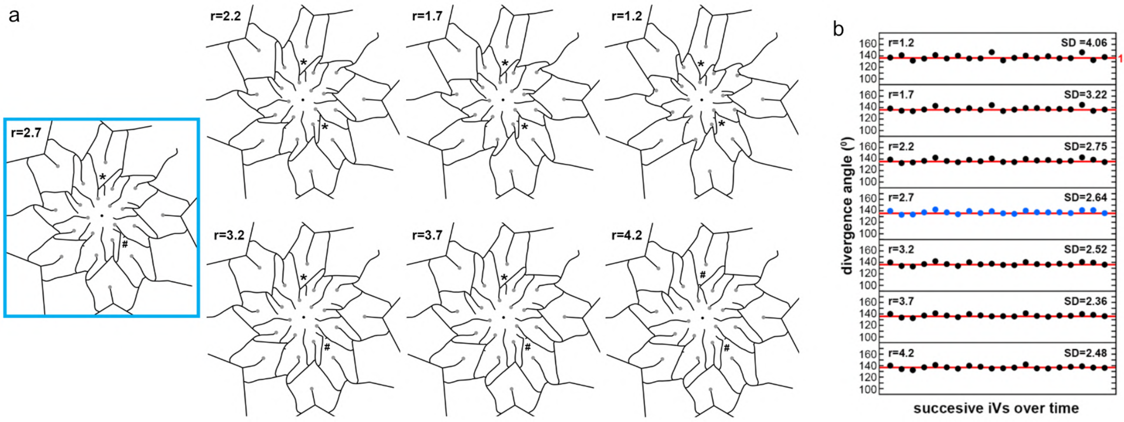

Figure 2.9 (a) Simulations of iV network development under different values of repulsion strength s_n at t= 218 h. A simulation under optimal repulsion strength ($s_n = 2.7$) is framed in blue. Grey dots, connections to the surface; a black dot, apex center. Selected merging and repulsion patterns are marked by asterisks and hash symbols, respectively, at the same iVs in simulations under different s_n value (also shown in c).
(b) Divergence angles measured between successive simulated iVs under different repulsion strength s_n over 255 hours. SD, Standard Deviation. The output of the simulation under optimal repulsion strength is shown in blue.
(c) Progression of simulated iV interconnections with respect to parastichy order under different repulsion strength s_n over 255 hours. The output of the simulation under optimal repulsion strength is shown in blue.

Moreover, the iV network in the pin1 mutant closely resembles the output of the Random Model (2.10d and 2.2a) supporting the view that the repulsion-based mechanism underlying the iV patterning may depend on polar auxin transport.

Tissue growth speed

Next, we analogously examined how the changes in tissue growth speed affect the interconnection pattern switch. We ran two simulations with modified growth speed values. It is interpolated as before but the b parameter is multiplied for all stages by 0.5 and 1.5 respectively. In figure 2.11 these simulations (marked as a, c) are compared to the original one (marked as a) after 290 hours of simulated growth. We can observe that with slower growth the shift from M to R occurs much later compared to the original simulation (5 more M pattern occurrences) and with faster growth, it occurs faster (2 more M pattern occurrences). Similarly to experiments with varying repulsion strength, changing growth speed moved the initial position of emerging iVs and as in the previous experiment if the initial position was further from the center, then the R pattern occurred earlier.

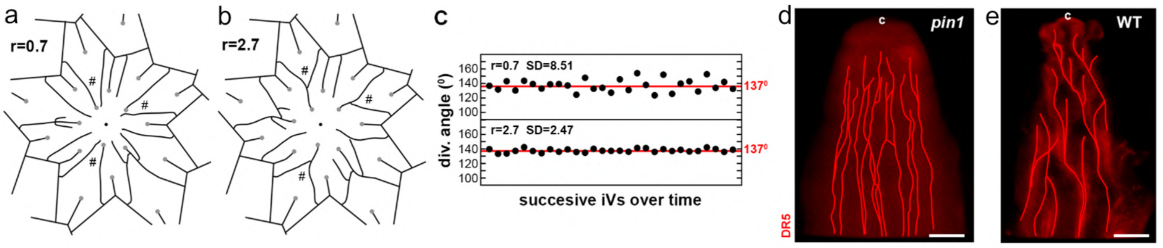

Figure 2.10 (a, b) Simulations of iV network development under lower (a) and optimized (b) repulsion strength at t=100h. At $s_n = 0.7$, iVs (hash) do not merge and their trajectories are nearly straight (a), while at $s_n = 2.7$, the corresponding iVs (hash) merge and show curved trajectories (b). Grey dots, connections to the surface; a black dot, apex center.
(c) Divergence angles measured between successive simulated iVs under lower and optimized repulsion strength 'sn' over 314 hours. n= 29 iVs for both 'sn' values.
(d, e) Side view of the inflorescence shoot apices in the pin1 mutant (d) and the wild type (WT) (e). Red lines, iV reconstruction based on internal DR5 expression. Black dot, the SAM center. n=9 apices per line.

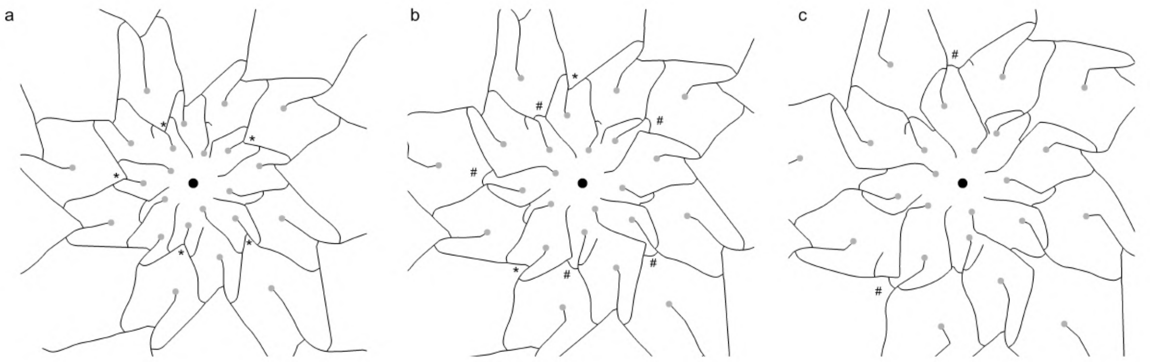

Figure 2.11 The figure shows simulations with modified parameters at t=290h *b* for growth speed: (a) - 50% of base value; (b) - 100% of base value; (c) - 150% of base value. Stars mark where the M pattern occurred and hashes mark the R pattern occurrence.

Lucas and bijugate phylotaxy

The model is not only limited to the Fibonacci pattern. We tested its ability to in two other occasional patterns Lucas spiral and bijugate. In them, We didn't notice anything similar to a connection pattern switch similar to one found in Fibonacci. The simulations were done with the assumption that the pattern and parameters of the simulation stay the same. However, due to their exceptional nature, we can be certain that they don't occur. The simulation required modification of certain parameters. A list of modified parameters can be found in 2.3

In the Lucas spiral pattern, the divergence angles between primordia are lower than in the Fibonacci pattern, i.e. 99.50 (Smith et al. 2006b) (fig. 2.12a). In our simulations

Table 2.3 Parameters for Small, Medium, and Large meristem Stages. Values that change with stages are written in bold

Parameter	**Lucas**	**Bijugate**	**Large**
Extension rate (µm/h)	4.00	6.00	
Emerging attraction	0.15	0.15	
Center distance threshold	55	53	
Plastochron (h)	13.00	24.00	
Divergence angle	99.50	68.76	
Left bifurcation age	13	42	
Right bifurcation age	39	24	
Tissue growth a	0.0015	0.0017	
Tissue growth b	0.54	0.64	
Tissue growth c	46.00	50.66	
Repulsion range r_n	69.23	79.225	

that use an appropriate template representing the Lucas pattern, we observed again a very good correspondence to the real observations (fig. 2.12c). Another phyllotactic pattern occasionally found in apices is the bijugate pattern, where two opposite primordia are formed simultaneously or almost simultaneously (fig. 2.12b). This differs significantly from the Fibonacci and Lucas patterns, which rely on single primordia initiated per plastochron. In the bijugate pattern, the divergence angles between primordia in successive pairs are 68.760, which is half of the Fibonacci angle (Smith et al. 2006b). We extended our model by taking into account the spatiotemporal localization of projected DR5 maxima and pre-existing iVs according to the dual-primordia development in the bijugate pattern. In this more complex phyllotactic pattern, these simulations also reproduce an iV arrangement with divergence angles that closely correspond to the angles of observed, real primordia (fig. 2.12d).

Thus, the repulsion-based model accurately replicates the iV arrangement according to various phyllotactic patterns, suggesting that local interactions between iVs are sufficient for recreating these complex patterns, even in the absence of directional cues from the SAM surface.

Ring experiment

To investigate how the positioning of surface primordia influences the outcomes of the model we increased the radial component of **primordium connection distance** to 180 degrees. This adjustment transforms the shape of a pending primordium from a dot or oval into a ring around the meristem center. In this experiment, there may be more than one iV awaiting a primordium. In this case, the older one is selected. This modification removes spatial

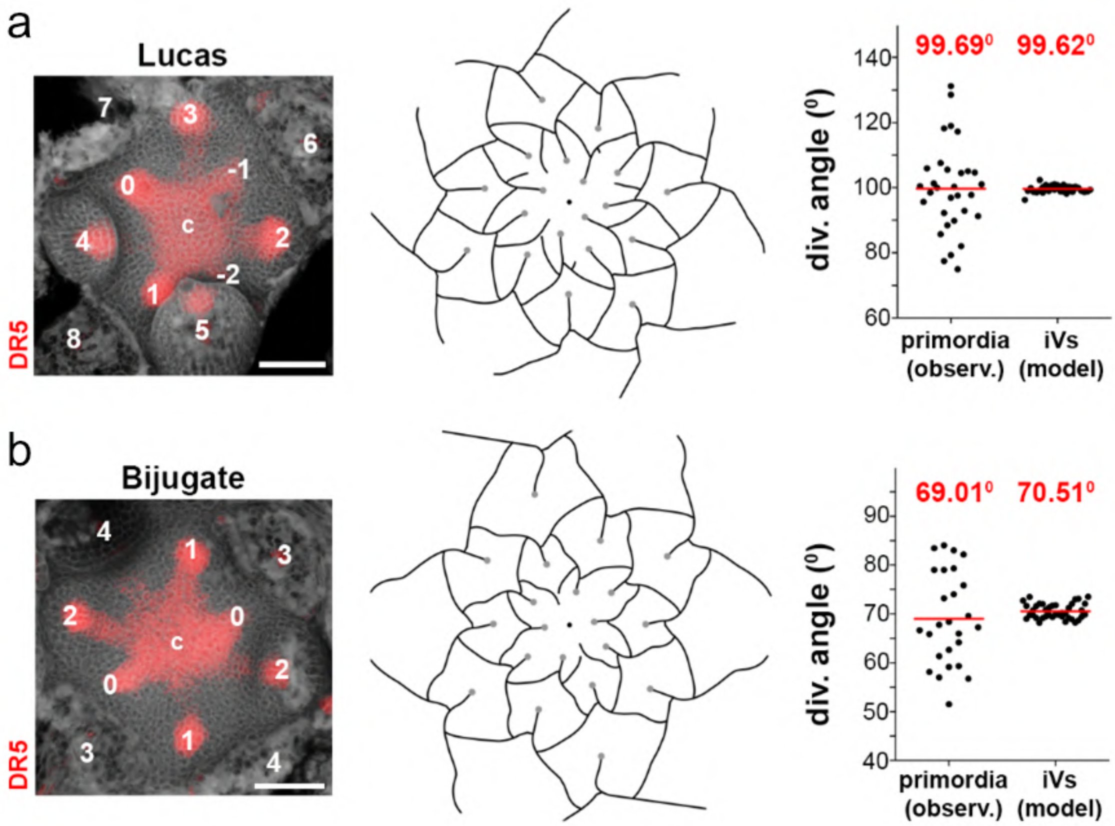

Figure 2.12 (a,b) Selected shoot apices displaying Lucas (a) and bijugate (b) phyllotactic patterns. The DR5 expression (red) marks incipient and existing leaf primordia. c, the SAM surface.
(c,d) Simulation of iV network development according to Fibonacci (B), Lucas (E) and bijugate (H) phyllotactic patterns. Grey dots, connections to the surface; a black dot, apex center.
(e,f) Divergence angles measured between successive real primordia (left) or simulated iVs (right). Red lines and numbers, mean; black dots, data. The iV angles were measured between iVs just before and after their connection to the surface. No significant differences between observation and model were detected (two-sample t-test, p=0.9742 (e), p=0.32773 (f). In (e) n= 31 p0-p12 primordia from 3 apices; for model n=36 iVs; in (f) n= 26 p0-p7 primordia from 2 apices, for model n=40 iVs.

influence from the primordia, confining their role to timing the maturation of iVs at each plastochron.

The results of this modification are depicted in 2.13. Initially, when the meristem is small, the simulation behaves identically to the original model (fig 2.13 a). However, upon the switch to the R pattern occurs, an anomaly arises: an emerging iV repelled from -17, begins to mature prematurely, creating an unusually sharp phyllotactic angle (24 degrees between

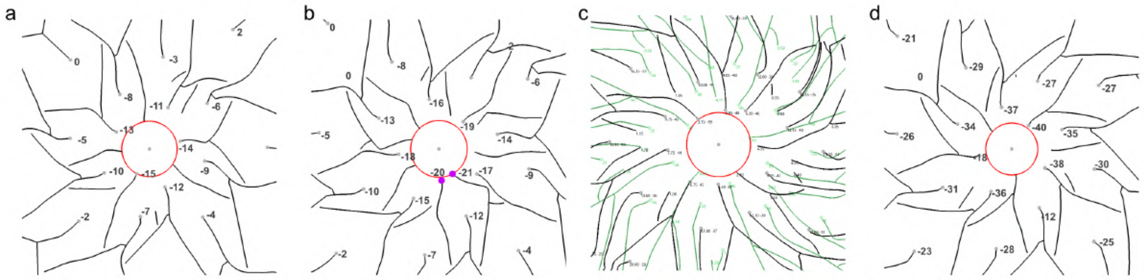

Figure 2.13 (a) Ring simulation of iV network development before the transition to the R pattern (t=168h).
(b) Ring simulation of iV network development after transition to the R pattern (t=228h). Two consecutive matured iVs from incorrect phylotactic angle of 24 degrees are marked with magenta.
(c) Ring simulation after 480 hours with overlaid original results (in green) shows a major deviation from the original experiment. (d) Ring simulation after 480 hours run with parameters for small meristem.

-20 and -21, fig 2.13 b). This discrepancy causes a chain reaction that leads to a completely different vascular pattern. To verify that this aberration is directly attributable to the transition to the R pattern, a parallel simulation with parameters set for a smaller meristem size was conducted (fig 2.13 c). This simulation maintained the merging pattern characteristic of a small meristem throughout 480 hours, aligning with the original simulation and experimental observations for small meristem (fig 2.13 d).

This experiment underscores the limitations of our model in accurately predicting phyllotaxy and suggests avenues for further research. One potential area of investigation is whether the extension speed of emerging iVs varies based on factors such as the proximity to existing iVs. If the growth rate of a repelled iV could be reduced due to the presence of a newly matured iV, this might yield a pattern that aligns more closely with observed plant structures. However, current experimental data do not provide a basis for this hypothesis. It's crucial to note that while this model aims to replicate iV patterns rather than phyllotaxy per se, the experiment highlights the significance of surface-level meristem processes in vascular formation.

2.7 Conclusion

This chapter presents the modelling of incipient vascular strands, an early stage of vein formation in the shoot apical meristem of Arabidopsis Thaliana with an agent-based model. It discusses the whole workflow of formulating this model from raw data and starting with data acquisition. It includes developing methods for manual and semiautomatic annotation of incipient veins from confocal microscopy data, that overcomes challenges faced when working with 3D volumetric data.

We formulate the model as a moving agent based on acquired empirical data. The agent's movement is controlled by an interaction function, that encapsulates the attraction-repulsion mechanism between iVs. Initially, our model generates the shape of an iV in a static skeleton. We develop an optimisation scheme that archives that allows us to find suitable values for the interaction function. After achieving the parameters, we extend the model, to include the dynamic effect of meristem growth and iVs maturation to accomplish a full simulation of incipient vasculature over a longer time of 20 days.

The final model was extensively validated, it can express shifts in vascular connection patterns in Fibonacci phyllotaxis. Additionally, it predicts how changes in growth speed or repulsion (caused by different PIN-1 expression) affect the vascular connections. Aside from that, we were able to recreate the iV connections in less common phylotaxis. Finally, we showed the limitation of this model, which suggests that the vein formation process below the surface requires input from the meristem surface.

There are several avenues for future work, such as better implementation of the second phase of growth, when iV goes up to the surface; examination of even eariler stages of grow or during the development from vegetative to reproductive stage. Those results are achievable by extending the current model with sufficient experimental data. However, to understand the mechanism governing iV formation would require to consider different modeling approach that can express celular dynamics.

This chapter directly addresses the hypotheses stated in the introduction by introducing a computational model to simulate vascular pattern formation, demonstrating the applicability of computational methods in biological research. This approach not only tests the capability of computational models to simulate intricate biological processes accurately (Hypothesis 1).

Using the agent-based model we could abstract complex mechanics of tissue growth, cell movement and division and treat the tissue as a uniform cone surface. We also abstracted from auxin transport mechanics. None of that has not been studied in this context yet. Instead, we focused on predicting the behaviour of the iV formation in various scenarios. This approach aligned well with the observations of this exploratory study of a newly observed phenomenon, where many details remain unclear. What prove the necessity of employing diverse modelling techniques to capture the unique dynamics of different biological phenomena (Hypothesis 2).

Moreover model conformed with extensive validation providing evidence for that attraction-repulsion is a governing mechanism in incipient vein formation and providing a new perspective on the discussion of the dominant component of vasculature formation, thus contributing to fulfilling Hypothesis 3.

Chapter 3

Long Distance Signalling Model of Auxin in Trees

3.1 Introduction

This chapter presents modelling aspects of [60], which investigates the underpinnings of the architectural differences between tree and bush forms in silver birch (Betula pendula) focusing on the comparison between the wild-type (WT) and strigolactone-deficient mutants exhibiting a bushy phenotype, particularly the transgenic line RNAi60. While the RNAi60 mutant is shorter than the wild-type, it maintains the same number of primary branches, whereas the number of secondary branches is higher, contributing to its dense, bush-like phenotype. Interestingly, the auxin (IAA), a pivotal plant growth hormone, distribution along the main stem differed between WT and the mutants. We observe a decreasing gradient of concentration from top to bottom in the WT, and conversely, an increasing gradient in RNAi60 mutants.

Apart from morphological distinctions, experimental observations did not reveal any differences that could account for the variance in auxin concentration observed. This led to the hypothesis that the same polar auxin transport (PAT) mechanism can account for the different auxin concentration gradients we observed in measurements of WT and RNAi60 based on the structural differences between these tree species alone. To investigate these auxin distribution patterns, we developed a Long-distance Signaling Model (LSM) and a computer simulation of dynamic PAT in three-dimensional tree structures based on it. In this simulation, we model auxin transport, synthesis and decay analytically using differential equations in a discrete graph structure of branch segments representing the topology of real birches.

3.2 Related Works and Modelling approach

PAT is an important aspect of plant growth, consequently, numerous works approached a process of modelling it in different aspects ([53]). These models predominately focus on phenomena observed at the cellular level, such as canalization or vein formation ([39]) or phyllotaxis ([24]). Very few works attempt to model auxin in the scale of a whole plant, ([65], ([48]).

The LSM is a hybrid model that combines a discrete representation of the geometry with a continuous representation of signalling. The choice of discrete representation for the tree geometry was motivated by its proficiency in representing branching structures of plants ([49],[48]), which allows for accurate replication of the distinct morphological features observed in the RNAi60 and WT forms, such as the variation in the number of primary and secondary branches. Similarly to [48], we divide the tree into segments branch segments of identical length. We assume that auxin transport mechanics in these segments mirror these mechanics on a cellular level. Modelling of signalling by differential equations was dictated by effort to achieve high efficiency. A discrete approach to signalling would require simulating millions of particles which would be computationally inefficient. Similarly, we use Navier-Stokes equations for modelling fluid behaviour instead of simulating individual water molecules.

3.3 Tree representation

Our model adopts a discrete graph representation to describe tree geometry, where each vertex corresponds to an element within the tree—be it a segment of a branch, a leaf, or a bud. In this framework, segments, each with a predefined length, define the tree's structure and directly determine branch lengths. Buds and leaves serve as primary and secondary sources of auxin, respectively.

The tree structure is similarly divided into metamers and branches as it is done in the assessment of biological trees. A metamer, the model's basic growth unit, consists of connected segments that follow a linear path. In botanical terms, a metamer includes a segment of a branch, a leaf, and a bud, forming a repeating unit of growth. We assume that the number of segments in every metamer, and effectively the length, is constant throughout the whole are as maximal paths of segments, and consequently metamers, sharing the same order, each terminating in a bud indicative of potential growth. At the end of each metamer, there is a branching segment, which serves as a potential bifurcation point. It has two child vertices. One represents the prolongation of a branch. The other represents an offshoot, a higher-order branch or a leaf.

The trees under investigation are 2-months-old silver birch trees cultivated under steady greenhouse conditions. Given their characteristics, the model's assumption of uniform metamer size closely reflects the observed growth patterns. These conditions have resulted in trees with a regular shape and metamers of equal size, validating our modelling choice and aligning it with the biological reality of these specimens. More importantly, the goal of the model is to facilitate the hypothesis, therefore it is sufficient to represent the architectural difference, not necessarily model every intricate feature of those trees. This substantiates the simplification within our model, making it not overly restrictive but an accurate representation of our experimental observations. While the assumption of uniform metamer size is validated by our observations of silver birch trees under controlled conditions, future iterations of the model could explore variations in growth patterns resulting from environmental factors or genetic differences.

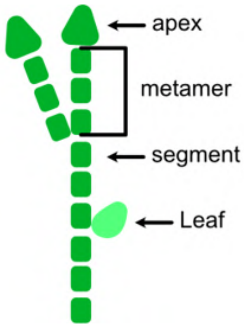

Figure 3.1 illustration represents a simple tree graph.

Trees are represented as directed graphs enriched with additional vertex information. Formally, the model represents a tree as tuple $\mathscr{T} = (V, E, F_t, F_o, F_A, F_T)$, where V is a set of vertices and a $E \subset V \times V$ is a set of directed edges. Each vertex v in the graph corresponds to a segment, a leaf, or a bud. We introduce several functions that correspond to the attributes of each vertex: F_t identifies the type of each vertex (segment, leaf, bud) and F_o identifies the branching order. Auxin and basipetal transport strength used for describing PAT dynamics are represented by functions F_A, and F_T respectively. For conciseness, we will use the notation $A_v := F_A(v)$ and $T_v := F_T(v)$.

Provided the tree representation we can recreate the architecture of 2-months-old WT and RNAi60 trees (fig 3.2a) based on the photographs and qualitative analysis of three architecture. We define metamer length for WT equal to 6 and for a mutant to 4. These values correspond to the ratio between WT and RNA60i length, which is approximately 3:2. Provided that the number of metamers is the same in both of them, we can assume that the ratio of metamer segments should be 3:2. Graph trees are generated using random procedure. The main stem has 27 metamers in both lines. Subsequently, we attach between 20 and 16 first-order branches to randomly chosen branching segments. The length of the branches is random, but, to achieve realistic architecture, the size range is progressively decreased with proximity to the tree top. In RNAi60 we additionally attach between 9 and 12 second-order branches at random. Finally, leaves are attached to all remaining branching

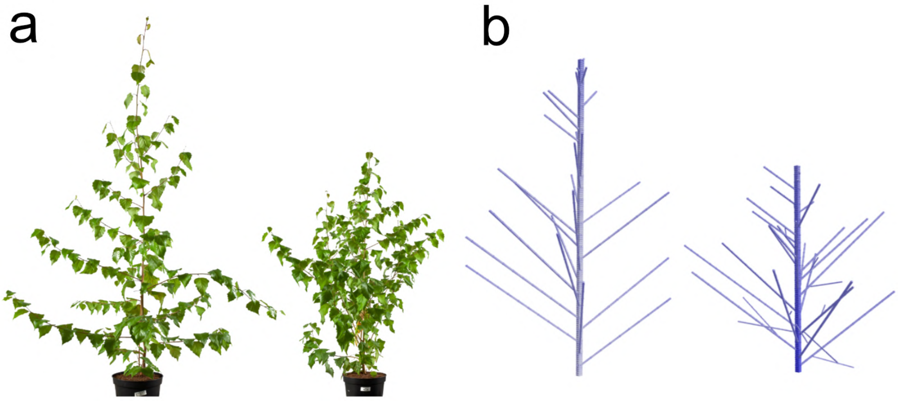

Figure 3.2 (a) photography of 2-months-old wild-type tree (left) and RNAi60 mutant(right) (b) visualisation of a tree representation of 2-months-old wild-type tree (left) and RNAi60 mutant(right)

segments. By setting different metamer lengths for WT and RNAi60 transgenic lines and the addition of second-order branches in RNAi60, we capture tree-like and bush-like morphology expressed by these lines.

3.4 Signaling model overview

In this section, we discuss modelling of auxin transport, synthesis and decay in a graph structure described in the previous section. Specifically, we formally describe the following assumptions which we call the Long-distance Signaling Model:

1. **Auxin synthesis:** Occurring at the apexes and at sites on branches where leaves are present, reflecting key areas of growth and development.
2. **Basipetal Transport:** Auxin moves from the apex towards the base, a directional flow critical for the plant's developmental patterning.
3. **Proportional Transport:** The strength of auxin transport is directly proportional to the auxin concentration, mimicking the efficiency and adaptability of natural auxin distribution.
4. **Global Decay Rate:** Auxin undergoes decay at a constant rate throughout the plan.

This basic model of LSM conforms conceptually to previously published formalisms that simulate long-distance auxin-mediated signalling [48].

The graph representing the tree $\mathscr{V}$ is dynamic meaning that we update it over a fixed number of simulation steps. In the model, one simulation step corresponds to 1 minute. Every vertex v has two attributes named auxin concentration A_v and basipetal transport strength T_v. In each simulation step, we update the values of these attributes by performing a forward Euler integration step of the differential equations calculating the rate of change of auxin concentration per vertex of the graph.

$$\frac{dA_v}{dt} = -A_v T_v + \sum_{c \in C} A_c T_c + P_A - A d_A.$$

The parameter d_A in the above equation is a parameter representing auxin decay while parameter P_A indicates the synthesis of new auxin. Auxin synthesis P_A is set to 0 for all segments. It is equal to the parameter p for bud vertices and for leaf vertices, it is equal to $r_l p$. Component $-A_v T_v$ corresponds to auxin outflux and $\sum_{c \in C} A_c T_c$ to auxin influx, set C is a set of child vertices of vertex v.

The transport strength of auxin is proportional to auxin flux defined as follows:

$$\frac{dT_v}{dt} = \frac{A_v T_v}{10 + A_v T_v} p_T + p'_T - T d_T,$$

where p_T and p'_T denote parameters that represent transporter production both dependent and independent from the auxin flow and d_T represents transporter decay.

3.5 Model evaluation

Efficient implementation using a 3D simulation framework written in the programming language Rust allowed for the exhaustive exploration of parameter space defined in equations (table 3.1). Such exploration was essential as precise estimates for auxin synthesis rates, decay rates and PAT speed in birches were not available from the experiments. Additionally allowed a deeper understanding of parameters and how they interact with each other. Therefore, we ran a set of simulations with varying configurations of parameter values of auxin dynamics covering a range of plausible values. Each simulation was run until auxin concentration values between simulation steps did not change noticeably anymore, or in other words until homeostasis was reached.

We then noted down all simulation runs that matched the diverging global auxin concentration patterns we measured in real WT and RNAi60. In figure 3.3c we show a slice of

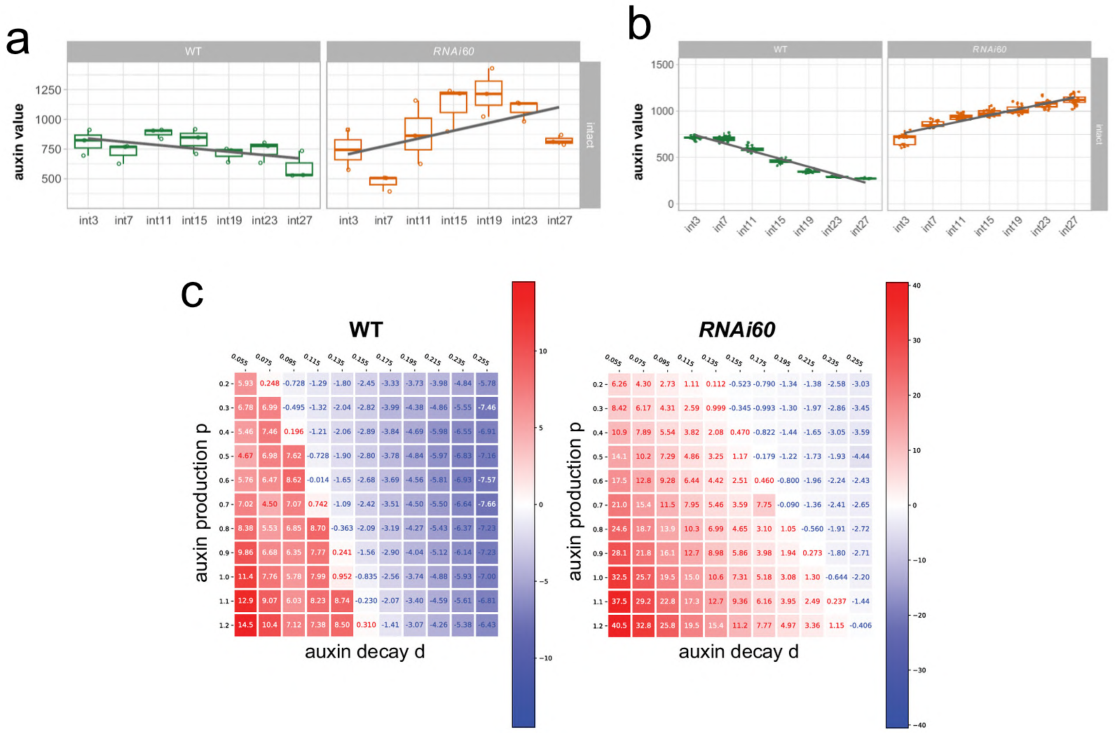

WT

	0.055	0.075	0.095	0.115	0.135	0.155	0.175	0.195	0.215	0.235	0.255
0.2	5.93	0.248	-0.728	-1.29	-1.80	-2.45	-3.33	-3.73	-3.98	-4.84	-5.78
0.3	6.78	6.99	-0.495	-1.32	-2.04	-2.82	-3.99	-4.38	-4.86	-5.55	-7.46
0.4	5.46	7.46	0.196	-1.21	-2.06	-2.89	-3.84	-4.69	-5.98	-6.55	-6.91
0.5	4.67	6.98	7.62	-0.728	-1.90	-2.80	-3.78	-4.84	-5.97	-6.83	-7.16
0.6	5.76	6.47	8.62	-0.014	-1.65	-2.68	-3.69	-4.56	-5.81	-6.93	-7.57
0.7	7.02	4.50	7.07	0.742	-1.09	-2.42	-3.51	-4.50	-5.50	-6.64	-7.66
0.8	8.38	5.53	6.85	8.70	-0.363	-2.09	-3.19	-4.27	-5.43	-6.37	-7.23
0.9	9.86	6.68	6.35	7.77	0.241	-1.56	-2.90	-4.04	-5.12	-6.14	-7.23
1.0	11.4	7.76	5.78	7.99	0.952	-0.835	-2.56	-3.74	-4.88	-5.93	-7.00
1.1	12.9	9.07	6.03	8.23	8.74	-0.230	-2.07	-3.40	-4.59	-5.61	-6.81
1.2	14.5	10.4	7.12	7.38	8.50	0.310	-1.41	-3.07	-4.26	-5.38	-6.43

RNAi60

	0.055	0.075	0.095	0.115	0.135	0.155	0.175	0.195	0.215	0.235	0.255
0.2	6.26	4.30	2.73	1.11	0.112	-0.523	-0.790	-1.34	-1.38	-2.58	-3.03
0.3	8.42	6.17	4.31	2.59	0.999	-0.345	-0.993	-1.30	-1.97	-2.86	-3.45
0.4	10.9	7.89	5.54	3.82	2.08	0.470	-0.822	-1.44	-1.65	-3.05	-3.59
0.5	14.1	10.2	7.29	4.86	3.25	1.17	-0.179	-1.22	-1.73	-1.93	-4.44
0.6	17.5	12.8	9.28	6.44	4.42	2.51	0.460	-0.800	-1.96	-2.24	-2.43
0.7	21.0	15.4	11.5	7.95	5.46	3.59	7.75	-0.090	-1.36	-2.41	-2.65
0.8	24.6	18.7	13.9	10.3	6.99	4.65	3.10	1.05	-0.560	-1.91	-2.72
0.9	28.1	21.8	16.1	12.7	8.98	5.86	3.98	1.94	0.273	-1.80	-2.71
1.0	32.5	25.7	19.5	15.0	10.6	7.31	5.18	3.08	1.30	-0.644	-2.20
1.1	37.5	29.2	22.8	17.3	12.7	9.36	6.16	3.95	2.49	0.237	-1.44
1.2	40.5	32.8	25.8	19.5	15.4	11.2	7.77	4.97	3.36	1.15	-0.406

Figure 3.3 (a) Experimental auxin concentration values in the model stems from tip to the base.
(b) Simulated auxin concentration values in the model stems from the tip to the base.
(c) Slices of parameter space. Each cell in the grid represents an auxin gradient obtained from the regression (grey kine in b) of an individual simulation run under the specified parameter value settings until homeostasis. Red color denotes a positive and blue color a negative gradient of auxin concentration

the parameter space of our computational model. The horizontal axis denotes auxin decay d_A and the vertical axis auxin synthesis parameter p_b. Each cell in the grid represents an individual simulation run under the specified parameter value settings until homeostasis. Cell colors indicate the gradient of the auxin concentration along the stem obtained from linear regression. Blue color indicates a negative gradient (decreasing auxin concentration values along the stem) and red indicates a positive gradient (increasing auxin concentration values along the stem).

The exploration revealed that our model has good characteristics. Gradual changes of parameter values cause gradual changes in the auxin gradient and for any parameter values within a reasonable range, the gradient is higher in RNAi60 than in WT. Specifically, in WT we expect constant or decreasing auxin concentration values at all segments of the stem (white/blue color) while in RNAi60 auxin concentration values should increase along the stem (red color). A wide range of our in silico experiments generated global auxin concentration patterns along the stem that matched the auxin concentration values observed in vivo even when using identical LSM parameter values - the different global auxin patterns are therefore the result of the varied numbers of segments that constitute a metamer in the two birch lines. In addition, in figure 3.2b we show an example rendering of our dynamic 3D simulation at homeostasis, where we used identical parameter value settings for both trees (p = 0.7, d = 0.155, corresponding to the middle cells in figure 3.3c). In this case, blue color indicates auxin concentration for a given segment which intensifies more for RNAi60 towards the base of the stem. In figure 3.3b we show auxin concentration values per metamer of the shoot for the same experiments as in figure 3.2b which conform to the observations in real plants shown in figure 3.3a. In summary, the analytical experiments using the LSM suggest that structural differences between WT and RNAi60 alone may suffice to explain differences in global auxin concentration patterns between the two lines.

Table 3.1 Summary of parameters in the Long-distance Signaling Model with values used in final result

Constant	**Description**	**Value**
p	Auxin synthesis rate	0.7
r_l	Auxin synthesis multiplier for leaves	0.2
d_A	Global constant representing auxin decay	0.155
p_T	Global constant for transporter production	1
p'_T	Global constant for transporter production independent of auxin flow	0.06
d_T	Transporter decay	0.05

Decapitation experiment

To further validate the model we replicated the decapitation experiment. Decapitation treatment with both stem and branch tips removed was applied to 1-month-old WT and RNAi60 trees. Decapitated trees were growing for one month (up to two in total) until the auxin levels were sampled, similarly to the original tree (figure 3.4a). In both lines decapitation of the main stem resulted in two top branches that acquired apical dominance and produced second-order branches. Decapitated first-order branches produced a single second-order branch close to the decapitation point (figure 3.4b).

To replicate these experiments, we created a procedure that recreates the geometry of decapitated trees. We first generate a one-month-old tree analogously to a 2-months old one. Next, we removed buds from all first-order branches and the stem and applied the results of

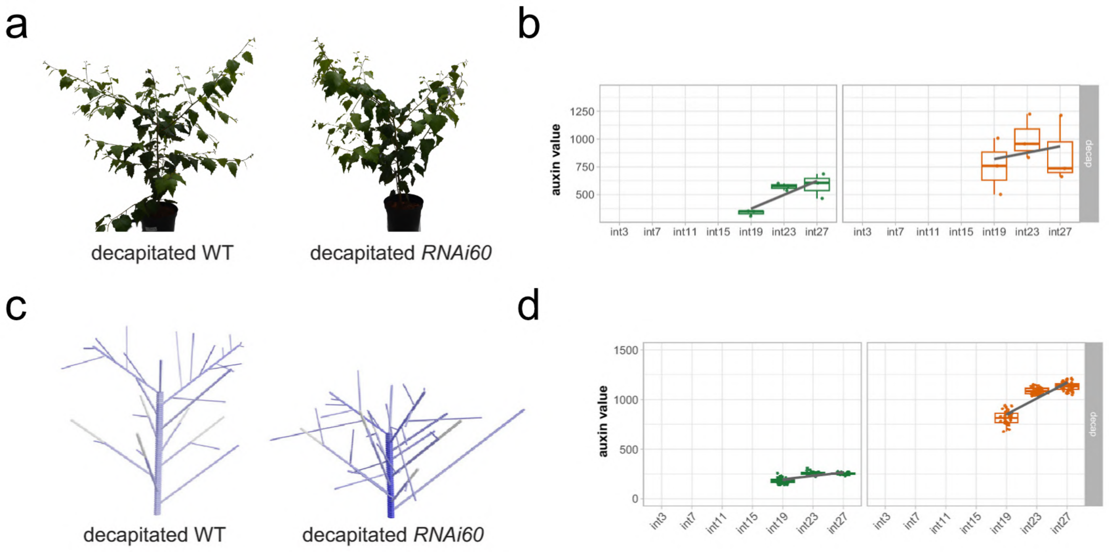

Figure 3.4 (a) Photographies of 2-moths old Wild-Type and RNAi60 trees with decapitation treatment.
(b) Experimental auxin concentration values in the model stems of trees with decapitation treatment.
(c) 3D representation of grpahs representing 2-month-old Wild-Type and RNAi60 trees with decapitation treatment.
(d) Simulated auxin concentration values in the model stems of trees with decapitation treatment.

growth post-decapitation (figure 3.4d). To calculate auxin levels in the main stem we used the same parameter values as in the original experiment.

We observed an alteration of the auxin distribution pattern in the WT after decapitation. Decapitated WT plants with higher-order branches showed an increase in IAA concentration from the top to base (figure 3.4b), similar to the intact RNAi60. Similar alterations are shown in the model results (figure 3.4d). Deviation in gradient value from the experimental results near the base was also visible in the intact experiment. It can be caused by environmental effects, that weren't

3.6 Conclusion

We proposed a model of long-distance signalling in birch trees and introduced tree representation as a discrete graph and signalling description through differential equations. The model has proven to be effective in showing how structural differences alone can affect the global auxin gradient. It aligns with Hypothesis 3, which states that modelling can be used to validate or disprove hypothetical biological mechanisms and highlight areas where further study is needed.

In contrast to the model presented in chapter 2 where we operated on continuous geometry of a 3D cone with a discrete agent model, this model operates in discrete space with differential equations. The nature of a studied object dictated different description of its geometry. In the case of apical meristem it is composed of small cells that are connected in a semi-regular manner, this space can be abstracted into continuous space, while in this chapter our study was centred around branches organisation in a tree. Describing such branching patterns is much more effective using a discrete geometry description. Regarding the choice of differential equations, we answer quantitative questions in this model, specifically how much auxin can be observed along the stem. Whereas during our study of iVs formation questions had qualitative character, e.g. we were categorising if repulsion between emerging iVs occurred or not. Adaptation of the agent model would be inefficient, to achieve similar numerical accuracy to the differential equation it would require simulating a large amount of agents that would be transported through the tree structure. This illustrates the necessity of adapting different computational paradigms to simulate varying aspects of auxin transport, supporting Hypothesis 2.

This model could be extended by imposing dynamic growth of tree structures based on auxin concentration or gradient. This could strengthen the argument for the hypothesis. A more interesting avenue would be to understand the mechanism behind the influence of strigolactone on the initial birch tree pattern.

Chapter 4

Scintilla: Simulating Combustible Vegetation for Wildfires

4.1 Introduction

Wildfires are disastrous natural phenomena that ravage communities and ecosystems alike. The Black Summer bushfire in Australia was a particularly severe example where an extensive area was burnt with more than one billion animal deaths [1]. A wildfire is the uncontrolled and often unpredictable combustion of vegetation that not only includes trees and shrubs but also other types of fuel, such as grass, duff, dead leaves and needles. These destructive events rapidly consume vast areas, leading to loss of life, property, and severe ecological damage. However, the underlying mechanisms that lead from smouldering ground combustion to a blazing crown fire are complex processes that are not fully understood. Therefore, to advance our understanding of the dynamics and progression of wildfires, we argue that it is critical to carefully simulate the feedback loops of vegetation, the atmosphere, and the composition of different fuels. By creating realistic 3D simulations, it is not only possible to enable applications such as training firefighters for wildfire management but also complex CG effects for movies or games.

A number of approaches have recently addressed generating more realistic models of ecosystems and the related physical processes between vegetation and the atmosphere. These methods range from efficient representations for large-scale ecosystems [31, 25] and urban forests [41] to the response of vegetation to erosion [13], avalanches [12], and climatic gradients [43]. In computer graphics, only a few methods address simulating the combustion of trees [47] and wildfires [21] with detailed geometry. Coupling intricate plant geometry with complex fluid dynamics, while also simulating the combustion process of fuel, remains

Figure 4.1 A temporal progression of a wildfire generated with our framework. Modeling different types of fuel and vegetation with detailed geometry enables simulating complex wildfire behavior ranging from harmless surface fires to raging crown fires.

a challenging objective. To the best of our knowledge, no method has simulated the various types of fuels that are represented by the understory and forest floor of an ecosystem.

In this chapter, we present a unified multi-scale representation for simulating wildfires. We generate 3D models of trees and shrubs based on branch modules – each plant is defined as a collection of modules that locally adapt to their environment. Based on this formulation we can efficiently model large-scale forest ecosystems. Plant matter that commonly defines the understory and forest floor, such as smaller plants, duff, and fine fuel, is represented by a novel layer-based representation that is integrated with the wildfire simulation. To simulate the horizontal as well as the vertical fire spread, we define a novel mathematical framework for heat transfer between the different fuel domains.

Unlike existing approaches in computer graphics, our unified framework can simulate all commonly described types of wildfires, including ground fires, surface fires, and crown fires in various stages. Furthermore, our approach realistically captures wildfires in different biomes, ranging from grassland, shrubland, savannah, tundra to boreal and deciduous forests. By including a detailed representation of vegetation our method captures the plausible dynamics of wildfires and their behaviour when subjected to various human forest management protocols. Furthermore, we include comparisons to controlled burn experiments that demonstrate that the emergent phenomena expressed with our simulations correspond to those observed in reality. Finally, to account for fire spotting due to sparks and flying embers, we advect particles through the air to then ignite fuel once they again make contact with vegetation to better express the unpredictable nature of wildfires.

In Fig. 4.1 we show a rendering of a complex wildfire created with our framework. The simulation parameter values have been calibrated to define an active crown fire which is combusting most of the vegetation that has been distributed in the scene. In summary, the contributions of this chapter are: We introduce (1) a novel fuel moisture model that accounts for a realistic distribution of fuel moisture in a forest biome as well as its integration into the wildfire simulation; (2) a boundary fuel model describing the impact of grass, fine fuel, and duff layers in a wildfire; (3) a physically-plausible model that captures the realistic generation, transportation and ignition of embers and firebrands that can produce new fires ahead of the fire front.

The work described in this chapter was accepted for the SIGGRAPH 2024 [27] conference as a Technical Paper and to be published in the SIGGRAPH 2024 issue of ACM Transactions on Graphics under the same title.

4.2 Related Works and Modelling approach

Unlike previous chapters phenomena of wildfire and combustion, that we tackle within this chapter, are explored through a wide range of modelling approaches, that aim to express their complexity. This spans from approaches for defining the pyrolysis process [9] and charring [30] to simulating the heat transfer [15]. Several studies investigate the resistance of plant species to wildfires [66, 29] and the impact of the moisture content of fuel [34]. It also has been recognized that the architecture of the canopy plays a role in the spread of wildfires [55]. Many existing methods focus on identifying parsimonious mathematical formalisms to analyze and predict wildfire behavior [51, 44, 40, 63, 32, 11, 26]. This includes models for the ignition of wildfires [3], the interaction of wildfires with the atmosphere [34] or simple geometric shapes as proxy objects for vegetation [38]. Moreover, the behaviour of wildfires is also studied specifically for different types of biomes [10, 14]. Existing simulation methods include empirical, physical, and even hybrid models, often relying on computational fluid dynamics [36] and large eddy simulations [16]. Finally, some methods investigate the fire spread according to different fuel types [37, 5]. For an overview of combustion processes the reader is referred to [35]. Many of these works aim to create an accurate representation of wildfires. However, either their predicting capabilities or, in the case of physically-principled wildfire simulators, they require long computation time, often several days to simulate a smaller wildfire. This limits their use in firefighting, where prediction is required in real-time. With recent advancements, AI models become more relevant in the prediction of natural phenomena [28]. The development of AI models requires labelled data, that is not generally available in case of wildfires. The data can be augmented synthetically but current methods are not adapted to produce realistic renders, which together with long computation times makes them poor candidates for it.

Our work aims to bridge a gap between computation time and predictive capability, offering a realistic wildfire simulation with high-quality renders. We achieve it by proposing a novel mathematical framework that unifies various modelling paradigms used to describe different aspects of combustion into a sophisticated hybrid model. This model combines the 3D domain of the atmosphere, the 2D domain of ground layers, a graph-based complex tree geometry and particle-based ember description. These components can be optimised and tuned independently, which allows us to adapt the simulation to the complexity of specific scenarios. With this approach, each domain is modelled more effectively, than when only one formalism is used, which is crucial for the aforementioned use cases.

4.3 Overview

Our main goal is to extend Hädrich et al. [21] by emphasizing the major role and coordinated action of different combustible materials such as grass, fine fuel, duff, and other vegetation, as well as the impact of fuel moisture, firebrands, and turbulence of fire. As input, our method uses a digital elevation model of the terrain with a soil water map, a set of multi-scale plant graphs [18] representing branches, modules and plants, an atmosphere data structure for storing variations in pressure, humidity, temperature, and wind velocities, as well as a soil map representing the distribution of soil water in the scene. Before running the wildfire simulation we first compute the fuel moisture content of the vegetation at module-scale based on the input – plants can have a varying distribution of fuel moisture within their structure. Additionally, we calculate the distribution of other wildfire fuels based on the vegetation data and described by 2D spatial maps representing grass, fine fuel, and duff (the boundary fuel layer).

For simulating wildfire dynamics, we introduce a multi-domain approach that describes combustion and heat transfer for all these materials. Specifically, we simulate the transfer of heat between the 2D spatial maps, the 3D domain of the atmosphere, and the plant graphs. Once the vegetation, the boundary fuels, and the atmosphere are defined, a user may interactively initiate fires anywhere in the scene by locally raising the temperature to a sufficiently high degree. Our wildfire simulation then resolves a set of coupled partial differential equations defined over the various spatial domains to simulate the combustion of vegetation, the boundary fuel layer, as well as the generation and transport of firebrands. This allows our approach to plausibly simulate wildfires occurring in the ground, on the surface and through the canopy, enabling the realistic combustion of vegetation in different forest biomes. An overview of our method is shown in Fig. 4.2.

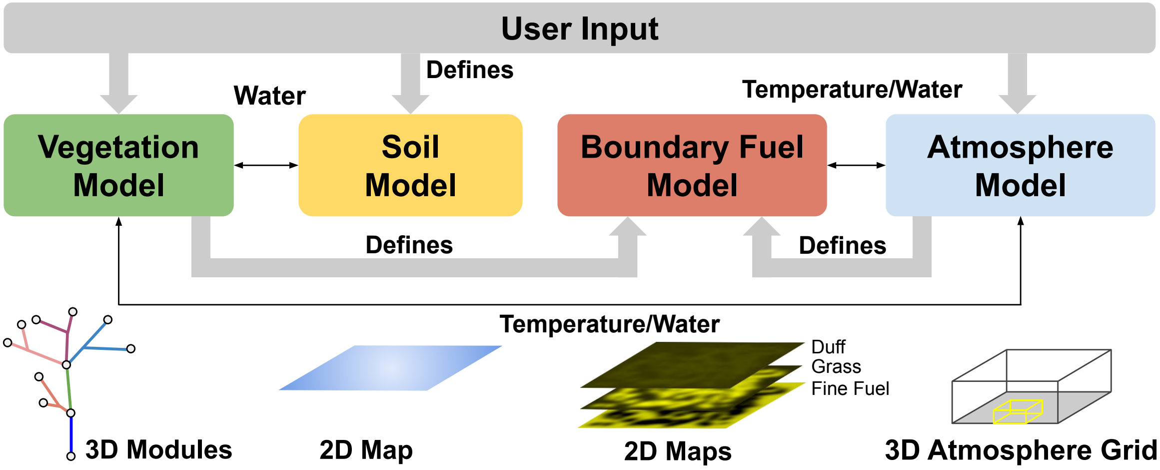

Figure 4.2 An overview of our method. A user specifies the initialization of vegetation, soil and atmosphere models as inputs. We then initialize the boundary fuel model. Wildfires are simulated by representing the fuel, water and other wildfire related quantities using a multi-domain approach, which includes 3D modules for representing plants, 2D maps for representing the soil and the forest floor, and a 3D grid for representing the atmosphere.

4.4 Wildfires

Wildfires in forest biomes can be highly unpredictable and dangerous, and their progression depends on a number of physical factors. Wildfires are typically initiated by a heat source such as lightning, human activity, or other natural events. Once a fire is ignited, it heats up the air and causes it to rise, which – in turn – draws in more oxygen and fuels to the fire. This process is known as convection, and it can cause the fire to grow rapidly. The flames can then leap from shrub to shrub, and embers can be carried by the wind to start new fires in other areas. Another physical phenomenon that can contribute to the spread of wildfires is radiant heat. As the flames burn, they emit heat that can ignite nearby vegetation even if the flames themselves do not reach it. This can cause the fire to spread more rapidly and unpredictably, making it difficult to contain. The rate at which a wildfire spreads also depends on the topography, the climate, and the type of biome, such as grassland, shrubland, forest or tundra.

Grassland wildfires tend to spread quickly and have a low to moderate intensity. The fine, continuous fuel bed of grasses allows for fast fire spread, while the relatively low biomass of the vegetation limits fire intensity. Grassland fires are often influenced by wind and may

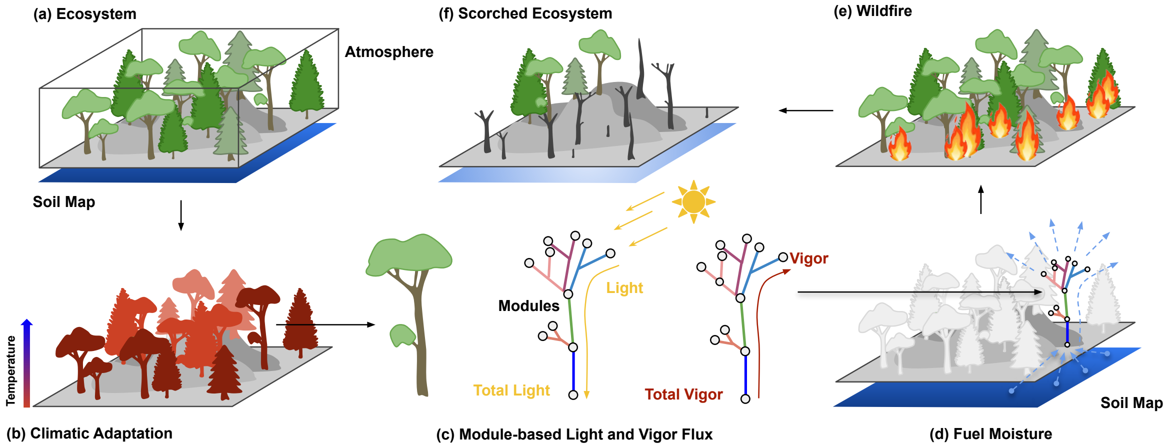

Figure 4.3 Stages of our wildfire simulation method: the initial ecosystem consists of terrain and vegetation, an atmosphere model, and a soil map (a), serving as the simulation input. We calculate climatic adaptation parameters for all plants (b) – lighter red colour intensity indicates less adapted plants to the cooler climate at higher altitudes. In (c) we show the computation of light and vigour flux for each module of a plant that we use to compute fuel moisture (d). Finally, we can simulate a wildfire (e) which then leads to a scorched ecosystem (f).

spread more quickly in areas with steep slopes or narrow canyons. *Shrubland wildfires* can be highly unpredictable, with rapid fire spread and high intensity. The presence of woody shrubs and other vegetation creates a complex fuel structure that can burn with high heat and create significant smoke. *Forest wildfires* can be extremely intense and destructive, particularly when they burn in the upper canopy. The presence of large trees and the abundance of ladder fuels, such as small trees and shrubs, can allow fires to spread rapidly and reach great heights. Forest fires can also create their own weather, with powerful up- and downdrafts that can contribute to erratic fire behaviour. Finally, *Tundra wildfires* typically burn in the upper soil layer, as the vegetation is low-growing and sparse. The low biomass of the vegetation limits fire intensity, but the flammable peat soils common in some tundra ecosystems can allow fires to smoulder underground and persist for weeks or even months.

4.5 Model

We introduce a wildfire model that describes the coordinated combustion of various organic fuels, such as wood, grass, and decomposing organic matter that enables the simulation of plausible wildfire dynamics in different forest biomes.

4.5.1 Hypotheses

The construction of our wildfire model follows a physically-principled approach. The combustion of wood and other organic materials is a complex chemical process involving hundreds of different molecules, that we aim to describe by a set of hypotheses capturing the essential processes controlling the dynamics of wildfires:

1. Organic material under heat is decomposed into char, vapour, and flammable gases (combustion); Eqs. 4.2, 4.13.
2. The rate at which organic material is combusted depends on its type, temperature and moisture content (fuel moisture); Eq. 4.14.
3. Thicker organic tissue that produces char undergoes pyrolysis and the region where this process occurs is approximated by a surface (pyrolyzing front); Eq. 4.13.
4. Temperature in the atmosphere and vapour are advected by the wind field (convection); see Sec. 4.3 [21].
5. Burning organic material may transfer heat to other organic materials and the atmosphere (radiant heat); see Sec. 4.5.6.
6. Grass amount per unit area is proportional to light availability, temperature, and soil water; Eq. 4.6.
7. Fine fuel amount per unit area is proportional to plant biomass and type; Eq. 4.7.
8. Duff amount per unit area is proportional to plant biomass, type, and soil water; Eq. 4.8.

Hypotheses (1)-(3) describe the combustion of organic material (pyrolysis). They are defined for the multi-scale plant graph representation of our wildfire model. Hypotheses (4) and (5) describe the coordinated action of wildfire components which are shared among other simulated spaces such as fuel, heat, water, and vapour transfer. Finally, hypotheses (6)-(8) describe how grass, fine fuel, and duff amounts are defined for a given scene.

4.5.2 Spaces

Our wildfire model comprises several spatial domains, each representing a distinct element of the wildfire environment (Fig. 4.3). We associate each domain with a specific set of variables to describe its specific conditions and properties.

Atmosphere. The atmosphere domain is a three-dimensional space that defines the atmospheric variables such as temperature T_a, light exposure L, water vapor q_v, smoke q_s, and the wind field u. Together, these factors set the overall climatic conditions influencing the fire behaviour, including its propagation and intensity. Additionally, it is within this space that smoke disperses and wind influences the direction and speed of the wildfire. We compute local light exposure by performing a single step of shadow propagation based on pyramid-shaped shadow cones [42]. The shadow cones are extended from each module position to update light exposure values of grid cells within that volume, which allows us to approximate light conditions for the whole scene.

Boundary Fuel Layer - Grass. This is a two-dimensional layer representing the grassy ground cover. For the grass layer we define the grass biomass ϖ_g, its temperature T_g, and moisture content W_g to describe how easily grass may ignite and how rapidly the fire will spread at ground level. Users may specify the type of grass present in the scene by defining species-specific climatic adaptation parameters for temperature T_A, humidity P_A, and light L_A.

Boundary Fuel Layer - Fine Fuel. The fine fuel layer is another two-dimensional layer, which represents smaller fuels such as twigs, leaves, and other loose organic material. The variables defined within this layer include the fine fuel biomass ϖ_f, its temperature T_f, and moisture content W_f. Our method specifies a number of parameters determining the amount and distribution of fine fuel. Fine fuels, due to their size and surface-to-volume ratio, are typically the first to ignite and can significantly influence the fire's spread.

Boundary Fuel Layer - Duff. The duff layer, also a 2D domain, represents the layer of decomposing organic material found beneath the litter of leaves and twigs. This layer defines the duff biomass ϖ_d, its temperature T_d, and moisture content W_d. The properties of the duff layer can impact the smouldering and the underground spread of the wildfire, as well as its duration.

Multi-Domain Mapping. Co-locating the 2D domains of grass, duff, and fine fuel with the 3D domain of the atmosphere mathematically requires mapping between the respective grids. In the 3D atmosphere domain, a z-coordinate value is associated with each point. This z-coordinate corresponds to the height above the ground level. We place the grass, duff, and fine fuel domains in the atmospheric domain based on their real-world heights. To co-locate these domains, we define a function $z = h(x,y)$ that maps each point in the 2D domain (x,y) to a height z in the 3D domain. This function is defined for each 2D layer. Therefore, we refer to the grass, fine fuel, and duff domains as the boundary fuel layer domains – the interface between ground and atmosphere. Interactions between the layers can then be calculated based on the spatial proximity and properties at each co-located point.

4.5.3 Vegetation Model

To represent vegetation we use a vigor-based representation for plants [31]. We employ a hierarchical, discrete graph representation composed of modules and branch segments to represent plants. A module $\mathscr{M}$ is composed of a set of connected branch segments where each branch segment is defined by a truncated cone. It can be described by a graph $G_{\mathscr{M}}$. Each module $\mathscr{M}$ is defined by a set of attributes comprised of moisture W, mass M, light flux Q, and vigour V. At the next higher scale of the hierarchy a plant $\mathscr{P}$ is defined by a graph $H_{\mathscr{P}}$ as a set of connected modules. In addition, each plant also has a number of plant type attributes which define various species dependent traits relevant to wildfire modelling. Specifically, each plant is defined by average fine fuel production φ_f, fine fuel spread σ_f, temperature adaptation T_A, humidity adaptation P_A, moisture production ψ, and transpiration rate κ_p. A full list of module and plant type parameters can be found in the Appendix (4.10.2). This multi-scale graph representation is used to generate realistic plant geometry (Fig. 4.20, Appendix 4.10.1).

We propose a method to compute fuel moisture values W for each module M of a plant $\mathscr{P}$ based on four steps: computing plant environmental adaptation, approximating local light conditions, distributing vigour to modules based on light conditions, and computing time-varying fuel moisture based on module vigour (Fig. 4.3b-d). For model details, we refer to Makowski et al. [31] and the Appendix.

Once we have computed vigour V for all modules, we compute their fuel moisture. We posit that branches exhibiting higher vigour, indicative of healthier and more hydrated vegetation, inherently possess higher moisture content, making them less readily combustible. Conversely, branches with lower vigour, suggesting weakened or dehydrated vegetation, have reduced moisture content, making them more prone to ignition and combustion. We compute the initial fuel moisture W of module $\mathscr{M}$ using a sum of softplus and sigmoid logistic functions:

$$W_{\mathscr{M}}(V_{\mathscr{M}},M_{\mathscr{M}}) = \log(1+e^{V_{\mathscr{M}}}) \cdot \psi \cdot M_{\mathscr{M}} + W_{min} \cdot \frac{1}{1+e^{-V_{\mathscr{M}}}}, \tag{4.1}$$

where ψ is a coefficient expressing species dependent moisture content, W_{min} defines a minimum fuel moisture value for a given plant type, and $M_{\mathscr{M}}$ is the total mass of a module. We define a starting moisture value for modules and calculate their changes over time that may result from transpiration due to heat:

$$\frac{dW_{\mathscr{M}}}{dt} = \kappa_w^m(T_{\mathscr{M}}) \cdot A, \tag{4.2}$$

where κ_w^m denotes an evaporation function for plants and A is the surface area of module $\mathscr{M}$. κ_w^m follows the idea of Arrhenius reaction rate but is modelled by a smoothstep function ($S_{a,b} : x \mapsto 3\bar{x}^2 - 2\bar{x}^3$ where $\bar{x} = max(0, min(1, (x-a)/(b-a)))$). This means that κ_w^m,

$$\kappa_w^m(T_{\mathscr{M}}) = S_{T_0^m, T_1^m}(T_{\mathscr{M}}) \tag{4.3}$$

in our model is described by a sigmoid-like function for computational efficiency reasons. Please note that in contrast to Hädrich et al. [21] we simulate the evapotranspiration of water prior to combustion. This significantly increases the realism of our model as organic material has to dry up first before it can ignite. We also take into account the evaporation of water from the soil by considering the temperature of the duff layer

$$\frac{\partial q_w}{\partial t} = \Delta q_w - \kappa_w^d(T_d) q_w\,, \tag{4.4}$$

where Δq_w represents water diffusion in the soil and where κ_w^d denotes an evaporation function. κ_w^d follows the idea of Arrhenius reaction rate but is modelled in our case by a smoothstep function:

$$\kappa_w^d(T_d) = S_{T_0^d, T_1^d}(T_d) \tag{4.5}$$

The terms $\kappa_w^m(T_{\mathscr{M}})A$ from Eq. (4.2) and $\kappa_w^d(T_d)q_w$ from Eq. (4.4) have to be accounted for when describing the rate of change of vapour q_v of the atmospheric model [21]. In summary, our vegetation model enables a detailed representation of fuel moisture by taking into account light exposure, the vigour of branches and the overall climatic adaptation of a plant to a particular region, as well as the evapotranspiration of plants and soil during a wildfire.

4.5.4 Boundary Fuel Model

Our boundary fuel model is defined by a layer-based representation for grass, fine fuel, and duff. Together, these layers capture the complexity of surface fuels typically present in wildfire-prone environments. In our mathematical model, we represent grasses as a concentration of biomass on a 2D grid. This model is specifically designed to define a plausible grass cover based on light availability, temperature, and soil water availability. Each grid cell in the model is assigned a biomass value B_g:

$$B_g(x,y) = \frac{\mathscr{N}_T(T_a) \cdot \mathscr{N}_L(L) \cdot \mathscr{N}_P(q_w)}{\mathscr{N}_T(T_A) \cdot \mathscr{N}_L(L_A) \cdot \mathscr{N}_P(P_A)} \cdot \varpi_g\,, \tag{4.6}$$

where x and y describe a position in the 2D map, ϖ_g is the biomass of the type of grass under ideal conditions, $\mathcal{N}_T(\cdot)$, $\mathcal{N}_L(\cdot)$ and $\mathcal{N}_P(\cdot)$ denote the normal distributions of temperature, light and soil water. We sample the light exposure L and the temperature T_a at the grid cell of the atmosphere space associated with the corresponding grass space cell (x, y). A distinctive feature of this model is the ability to express different grass species by allowing users to specify values of environmental adaptation parameters. These parameters encapsulate the specific adaptive traits of grass species in response to environmental variables, allowing for the simulation of various grass types under diverse climatic conditions.

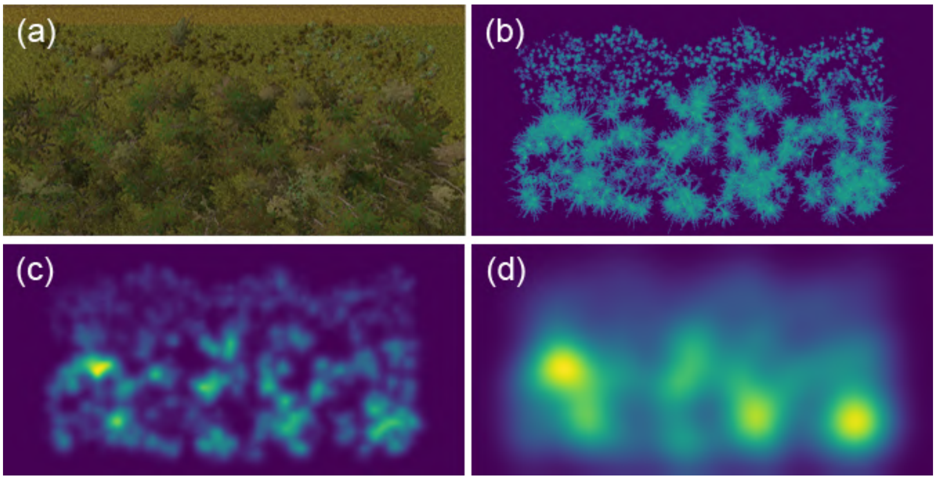

Figure 4.4 Stages of fine fuel map computation: top-down view of the forest edge scene (a). A colourmap representation of plant modules indicating distinct plants and their structure within the ecosystem (b). Fine fuel map generated using a smaller value of the parameter σ_f, depicting how fuel is distributed closely around individual plants (c). Fine fuel map computed with a larger σ_f value, demonstrating a broader spread of fine fuel around each plant (d).

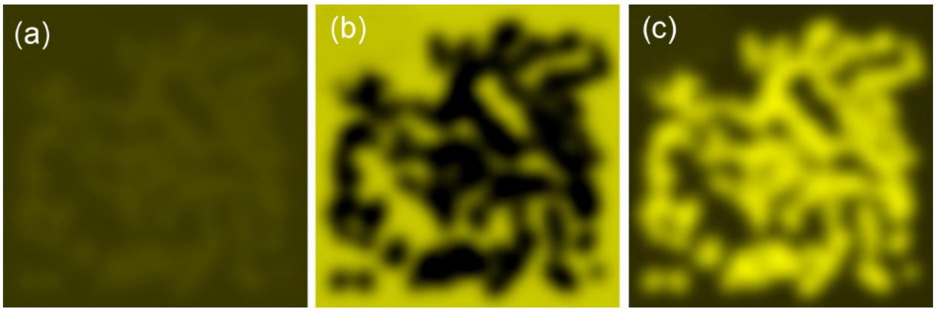

Figure 4.5 An example arrangement of duff (a), grass (b), and fine fuel (c), generated using our boundary fuel model. Grass is avoiding the regions where shrubs are located (dark spots), whereas duff and fine fuel are found more readily around the locations of shrubs.

Duff map B_d and fine fuel map B_f are obtained by sampling all plants associated with the wildfire scene. The computation of the fine fuel amount is based on the total biomass of all plant modules. Each module's contribution to the fine fuel layer is calculated based on its biomass. This biomass is processed through a kernel function, referred to as the fine fuel kernel G_f which transforms the 3D plant module biomass distribution into a 2D map of fine fuel amount,

$$G_f(\mathscr{M},x,y) = \frac{\varpi_f}{2\pi\sigma_f^2} e^{-\frac{(x-x_{\mathscr{M}})^2+(y-y_{\mathscr{M}})^2}{2\sigma_f^2}} \cdot M_{\mathscr{M}} \cdot \varphi_f \,, \tag{4.7}$$

where $x_{\mathscr{M}}$ and $y_{\mathscr{M}}$ are the position of a module in 3D space, ϖ_f a global fine fuel biomass scaling coefficient, σ_f is the standard deviation of the Gaussian distribution which determines the spread or width of the Gaussian function, $M_{\mathscr{M}}$ the biomass of the module of a plant, and φ_f a coefficient that describes how prone a given plant species is to distribute fine fuel. The fine fuel kernel function accounts for the dispersal and deposition patterns of fine fuels, capturing the effect of plant structure on the distribution of these fuels. In Fig. 4.4 we show two example fine fuel maps (c, d) computed from an initial scene (a) and a visualization of the modules (b). Varying σ_f values allows to control of the range of fine fuel dispersal. Similarly, the duff layer is computed from the 3D modules, but the translation considers the accumulation and decomposition patterns dependent on humidity:

$$G_d(\mathscr{M},x,y) = \frac{\varpi_d}{2\pi\sigma_f^2} e^{-\frac{(x-x_{\mathscr{M}})^2+(y-y_{\mathscr{M}})^2}{2\sigma_f^2}} \cdot M_{\mathscr{M}} \cdot \varphi_f \cdot \mu_d(q_w) \,, \tag{4.8}$$

$$\mu_d(q_w) = e^{-\frac{1}{2}\left(\frac{q_w-\mu_d^{opt}}{\sigma_d}\right)^2} \,, \tag{4.9}$$

where the duff kernel function is defined analogously to the fine fuel kernel function but additionally depends on a moisture function μ_d derived from soil water q_w, an optimal moisture value for decomposition μ_d^{opt}, and a term controlling the spread of the bell-shaped curve σ_d. The closer the soil water amount is to the optimal moisture value the faster fine fuel is transformed to duff. We obtain 2D maps representing the biomass of fine fuel and duff by accumulating the kernel functions for all plants:

$$B_f(x,y) = \sum_{\mathscr{P}} \sum_{\mathscr{M}\in\mathscr{P}} G_f(\mathscr{M},x,y), \tag{4.10}$$

$$B_d(x,y) = \sum_{\mathscr{P}} \sum_{\mathscr{M}\in\mathscr{P}} G_d(\mathscr{M},x,y). \tag{4.11}$$

By using this approach, our model provides a spatially explicit representation of the boundary fuels. The computation of grass, fine fuel, and duff moisture W_g, W_f, W_d is achieved by linearly scaling soil water q_w with coefficients ψ_g, ψ_f, ψ_d expressing layer-specific moisture control (e.g., $W_g = \psi_g \cdot q_w$). The rate of change of the boundary fuel layer biomass and moisture is then defined by:

$$\frac{\mathrm{d}B_b}{\mathrm{d}t} = -k(T_b, W_b), \frac{\mathrm{d}W_b}{\mathrm{d}t} = -k_w(T_b, W_b)\sqrt{B_b}, \tag{4.12}$$

where the index b indicates any of the three boundary fuel types and T_b the temperature (see Eqs. 4.18, 4.19, 4.20). An example rendering of the 2D maps after considering the contribution of all modules is shown in Fig. 4.5. In this scene, grass is avoiding the locations of shrubs due to lower light exposure values (dark spots, Fig. 4.5b), while duff and fine fuel are arranged in some proximity of the shrubs according to the Gaussian kernel calculations (light colour, Fig. 4.5a, c).

4.5.5 Combustion

The main mechanism driving a wildfire is the combustion of wood and other organic matter that act as fuel. Combustion is a chemical reaction that occurs between a fuel and an oxidizing agent, typically oxygen, resulting in the production of heat, light, and various reaction products such as water and carbon dioxide. We assume a more realistic model of combustion compared to Hädrich et al. [21] by including vapour in the combustion process. Organic material is decomposed into char, flammable gases (fuel), and vapour i.e.,

$$\text{Organic Material} + \text{Heat} \rightarrow \text{Fuel} + \text{Char} + \text{Vapor}\,.$$

Additionally, we extend the rate of the mass change introduced in Pirk et al. [47] $\mathrm{d}M/\mathrm{d}t$ to account for fuel moisture and water vapour which can be described by

$$\frac{\mathrm{d}M}{\mathrm{d}t} + k(T_{\mathscr{M}}, W_{\mathscr{M}}, u)\, cA = 0\,, \tag{4.13}$$

$$k(T_{\mathscr{M}}, W_{\mathscr{M}}, u) = \eta(u) \cdot S_{T_0,T_1}(T_{\mathscr{M}}) \cdot S_{W_0,W_1}(W_{\mathscr{M}}), \tag{4.14}$$

$$\eta(u) = 1 + (\eta_{\mathsf{max}} - 1)\, S_{0,u_{\mathsf{ref}}}(u)\,, \tag{4.15}$$

where k denotes the reaction rate of the combusting fuel which is obtained from the temperature of the module $T_{\mathscr{M}}$, the total moisture of module $W_{\mathscr{M}}$, and wind speed u. The dimensionless char insulation parameter is denoted by c and the pyrolyzing front area by A. Both, c and A depend on the tree geometry and vary during the combustion process. Please see Hädrich et al. [21] for a detailed description. In contrast, in our model, we extend the description of the reaction rate to also take into account fuel moisture. In reality, wood or other organic fuels with high moisture content do not combust as easily as dry fuels, and the moisture must be evaporated before combustion can proceed, which requires additional energy and hence slows down the reaction. Consequently, this is an important extension to increase the realism of wildfire modelling. However, we keep the sigmoid-like relationship as already introduced in Sec. 4.5.3 (Eq. 4.3) to ensure an efficient computation (compared to using an exponential function). Variable η describes the impact of wind on the reaction rate, where we assume that strong winds can increase the reaction rate. We use the definition of η where u_{ref} denotes a reference wind speed for maximum boost.

4.5.6 Heat Transfer

In our model, wildfires are defined by the complex interplay of heat transfer processes across multiple spatial domains. The 3D atmospheric domain represents the air above the ground and is subject to heat transfer processes such as conduction, convection, and radiation. We define a time-dependent vector-valued velocity field $u : (x,t) \mapsto u(x,t)$ which for given time $t \in \mathbb{R}^{\geq 0}$ and position $x \in \mathbb{R}^3$ returns the corresponding local flow $u(x,t) \in \mathbb{R}^3$. The temporal evolution of u follows Hädrich et al. [21] and defines drag as well as buoyancy forces. We define temperature as a scalar field returning the corresponding temperatures T_a at times $t \in \mathbb{R}^{\geq 0}$ at positions $x \in \mathbb{R}^3$:

$$\begin{aligned}\frac{\partial T_a}{\partial t} + u \cdot \nabla T_a = \alpha \nabla^2 T_a - \gamma (T_a - T_{\mathsf{amb}})^4 - \tau \frac{\mathrm{d}M_s}{\mathrm{d}t} \\ - K_{ga}(T_a - T_g) - K_{fa}(T_a - T_f)\,,\end{aligned} \tag{4.16}$$

where the terms $K_{ij}(T_j - T_i)$ represent the heat flux from domain j to domain i, and K_{ij} is the thermal conductivity at the interface between the domains. Please note that in Hädrich et al. [21] the boundary fuel domains are not included. The temporal temperature change of a certain fluid parcel, as it flows along the trajectory of the wind, is described by a diffusion component with intensity α, and an ambient cooling component with the radiative cooling term γ involving a fixed ambient temperature T_{amb}. Whereas, K_{ga} denotes the heat conductivity between grass and the atmosphere and T_g is the grass temperature. M_s denotes the mass of the grid cell and is defined as the weighted sum of vegetation modules's mass that overlaps this grid cell. The water content W_s in each grid cell is similarly defined.

Vegetation, which serves as the fuel source in wildfires, is represented using a graph-based model, with nodes representing branch modules and edges connecting them. Therefore, in addition to the environmental temperature field T_a, we introduce a module temperature function $T_{\mathscr{M}}(M,t)$ which for given time $t \in \mathbb{R}^{\geq 0}$ and module $\mathscr{M}$ returns the module's surface temperature. Heat transfer of modules is described as heat conduction between modules and radiative heat exchange with the atmosphere:

$$\frac{\partial T_{\mathscr{M}}}{\partial t} = \alpha_m \nabla^2 T_{\mathscr{M}} + b(T_a - T_{\mathscr{M}}), \tag{4.17}$$

where α_m and b denote diffusion and temperature coefficients.

Heat transfer in the boundary fuel domains is modelled by two-dimensional heat conduction equations, capturing the transfer of heat within and between these layers. These equations are coupled with the 3D atmosphere domain through boundary conditions that represent heat exchange between the ground layers and the atmosphere:

$$\frac{\partial T_g}{\partial t} = D_g \nabla^2 T_g + K_{ga}(T_a - T_g) + K_{gf}(T_f - T_g) + K_{gd}(T_d - T_g), \tag{4.18}$$

$$\begin{aligned} \frac{\partial T_f}{\partial t} = D_f \nabla^2 T_f + K_{fa}(T_a - T_f) + K_{fg}(T_g - T_f) \\ + K_{fd}(T_d - T_f) \end{aligned}, \tag{4.19}$$

$$\frac{\partial T_d}{\partial t} = D_d \nabla^2 T_d + K_{df}(T_f - T_d) + K_{dg}(T_g - T_d), \tag{4.20}$$

Please note that duff does not transfer heat directly to the atmosphere but only to the grass or fine fuel layer.

4.5.7 Sparks and Embers

In real wildfires, sparks and embers can lead to sudden new fires, even at distant locations from the main fire line. Consequently, understanding how firebrands are generated and transported is of paramount importance for firefighting. Due to the complexity of the phenomena involved in the problem, such as heat transfer, fluid dynamics, combustion, and structural failure, it has yet to be fully understood and modelled. It has been shown that the particles released per kilogram of fuel consumed are around 10^3 for different species [2]. We can simplify this information by assuming that the number of particles released is proportional to the amount of burnt fuel, i.e.,

$$\frac{\mathrm{d}N_e}{\mathrm{d}t} = c_e \frac{\mathrm{d}M}{\mathrm{d}t}, \tag{4.21}$$

in which c_e is the proportional constant and N_e is the ember release rate occurring during the combustion in every tree module. In addition to the ember generation rate, a realistic ember model must mimic similar ember geometrical properties to those happening in real tree combustion due to the strong influence of geometric properties in transport and ignition phenomena. Therefore, we consider the statistical work made by Tohidi et al. [61] which shows that the ember surface area A_s follows a logarithmic normal distribution $\mathsf{LogNormal}(\mu_{\log}, \sigma_{\log})$ with logarithmic mean and standard deviation

$$\mu_{\log} = \log \frac{\mu^2}{\sqrt{\mu^2 + \sigma^2}}, \quad \sigma^2_{\log} = \log\left(1 + \frac{\sigma^2}{\mu^2}\right), \tag{4.22}$$

in which μ and σ are calculated from the experimental data collected by Manzello et al. [33]. To estimate the ember mass, we use the approximation $m_e \approx A_s^{3/2}$.

Ember transport. The firebrands are described as particles with a position (same as with the module position) and velocity following Newton's 2nd law of motion. We regarded the drag forces generated by the fire plume and wind, the embers' weight, and neglected lift forces due to the small velocity gradients around the spherical embers. The drag force was estimated using a correlation proposed by Schiller and Naumann [54] to calculate the drag coefficient.

Combustion and heat transfer by embers. The crucial ember parameters are temperature, size, and age. As we will see in the next paragraph, these parameters are the main variables that can considerably affect our results. Therefore, we implemented a model similar to Eq. (4.13- 4.15) neglecting the moisture content in the particle as follows:

$$\frac{\mathsf{d}m_e}{\mathsf{d}t} + k(T_e, u_{\mathsf{rel}})\, c A_e = 0, \tag{4.23}$$

where A_e denotes the ember surface area, u_{rel} the speed difference between ember and wind, and T_e the ember temperature. Moreover, according to Stefan-Boltzmann and Newton cooling laws, we estimated the ember temperature change by

$$m_e C p_e \frac{\partial T_e}{\partial t} = \sigma A_e (T^4_{\mathsf{amb}} - T^4_e) + h A_e (T_a - T_e) - \Delta H_c \frac{\mathsf{d}m_e}{\mathsf{d}t}. \tag{4.24}$$

The convective coefficient h is given by the correlation proposed by Whitaker [64] and ΔH_c denotes the combustion heat rate.

Fire spot ignition by embers. The numerical solution of heat transfer between embers and other vegetation is challenging as it requires very small time steps. Therefore, we employ an analytical solution following the findings of Hadden et al. [19], who demonstrated experimentally that the so-called hot spot ignition theory can be a reliable qualitative indicator for the ignition of grass beds by embers. When the ember intersects a module or the bottom grid layer of our simulation domain, we model the grass ignition in a grass layer cell by

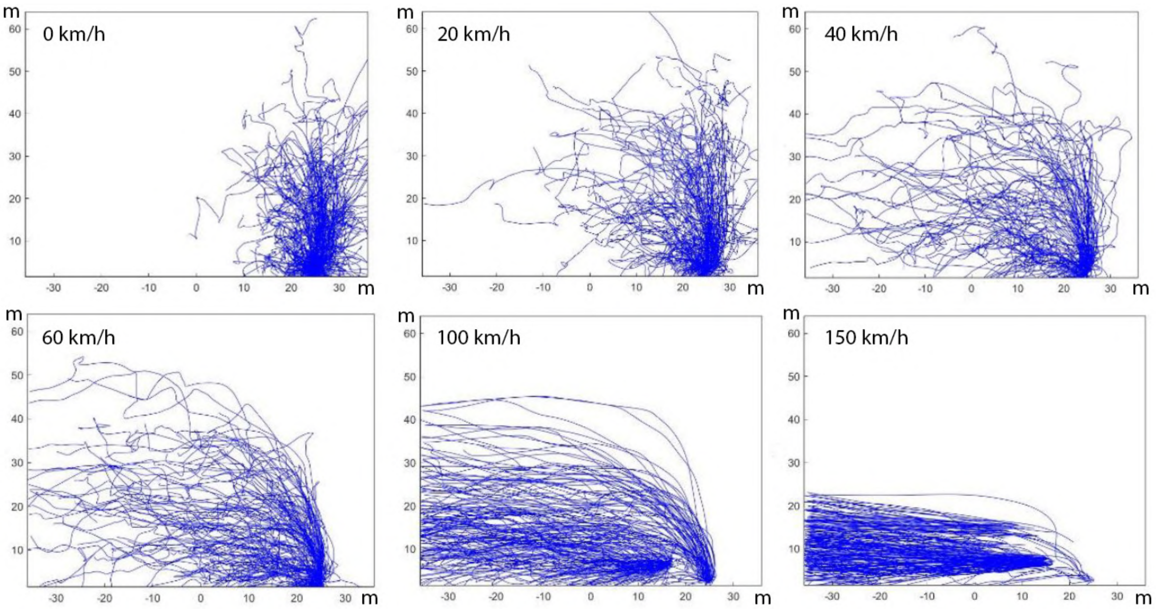
0 km/h
20 km/h
40 km/h
60 km/h
100 km/h
150 km/h

Figure 4.6 100 Firebrand trajectories depicted as blue lines for various vertical wind profiles of varying speeds ranging from 0, 20, 40, 60, 100, and 150 km/h. The trajectories are more random with lower velocities compared to high wind velocities, but at higher wind speeds the embers are carried a longer distance. The range of how far the embers travel is given in meters (m).

estimating the minimum particle radius necessary for ignition as follows

$$r_{cr} = \delta_{cr}\sqrt{\frac{K_{gg}}{\rho_g A_g \Delta H_g}\frac{RT_e^2}{E}\exp\left(\frac{E}{RT_e}\right)}\,. \tag{4.25}$$

where δ_{cr} denotes the Frank-Kamenetskii hot spot parameter for ignition (4.27), k_{gg} the grass thermal conductivity, A a grass pre-exponential factor, E the activation energy, R the universal gas constant, and ΔH_g the grass combustion heat. In case the ember radius is greater than the minimum particle radius for ignition r_{cr}, we raise the temperature of the grass layer to T_1, which is the temperature of combustion. If the ember does not have enough energy to start a new fire, it is discarded. It is worth noting that, like in real wildfires, the ignition of new fire spots in cells is not a sufficient condition to start a fire. New fires will only start in cells where the heat transfer from grass layers to wind and the environment does not suffocate the new fire.

We estimate the dimensionless Frank-Kamenetskii hot spot parameter δ_{cr} at which thermal runaway (ignition) occurs as:

$$b = \frac{\rho_g C p_g}{\rho_e C p_e}\,,\quad \beta = \frac{RT_e}{E}\,,\quad \theta_0 = \frac{E}{RT_e^2}\left(T_e - T_g\right)\,, \tag{4.26}$$

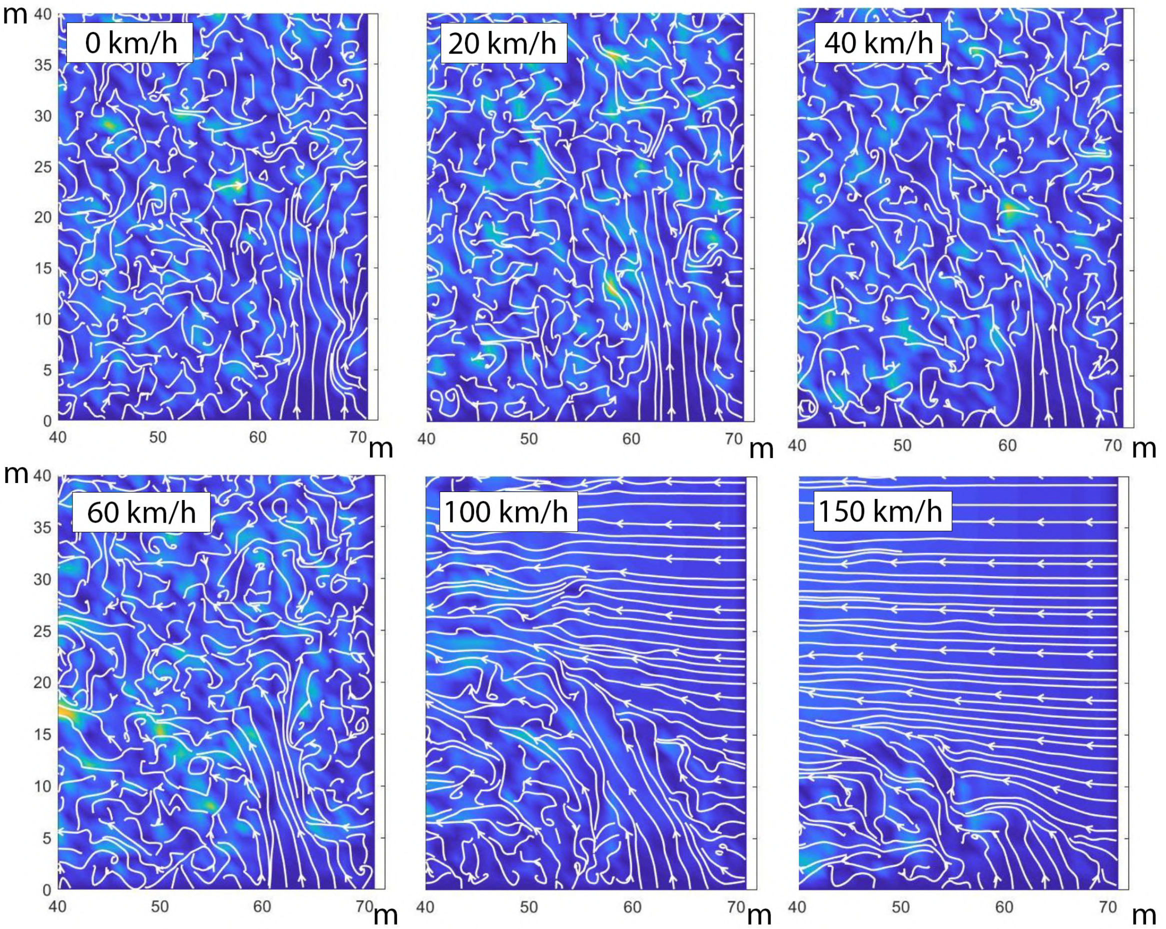

Figure 4.7 Stream plots of the wind field for the simulation results shown in Figure 4.6 with varying speeds ranging from 0, 20, 40, 60, 100, and 150 km/h. The colour map jet indicates the speed of the wind field. The stream plots indicate a higher updraft at the position of the fire at lower wind velocities which explains the more erratic trajectories of embers. For both axes the range of how far the embers travel is given in meters (m).

$$\delta_{cr} \approx 0.4\sqrt{b^2+1.5\,(b+0.1b^3)}\,(2.25-\theta_0)^2\,(1-0.5\beta\theta_0)\,, \tag{4.27}$$

where Cp_g, ρ_g, E, T_g, and R are the specific heat of the grass, grass density, grass activation energy, grass temperature, and ideal gas constant.

Figure 4.6 shows example trajectories of our ember model. At low wind velocities the trajectories are quite random leading (a-c) to more unpredictable migration of firebrands compared to the experiments with higher wind velocities (d-f). This can result in a more chaotic shape of the fire front (Figure 4.17 i-l). The stream plots in Figure 4.7 expose the shape of the fire plume (at location 60m - 70m) which is the cause of the updraft carrying the firebrands into a higher altitude. Please also note the more turbulent wind field contributing to the random ember trajectories at lower wind velocities.

4.6 Implementation

Algorithm 3: Wildfire simulation preparation.

```
Input: Digital elevation model of the terrain, multi-scale plant graphs, atmosphere
       data structure, soil map.
Output: Fuel moisture content of vegetation, 2D spatial maps of grass, fine fuel, and
        duff distribution.
1  Approximate local light conditions $L$ (Sec. 4.5.2)
2  Compute the fuel moisture content for each plant module:
3      for each plant $\mathscr{P}$ in vegetation do
4          Compute plant environmental adaptation $o$ using Eq. (4.28)
5          Distribute light flux $Q$ through the plant graph $H$ using Eq. (4.29)
6          Distribute vigor flux $V$ through the plant graph $H$ using Eq. (4.32)
7          for each module $\mathscr{M} \in \mathscr{P}$ do
8              Compute fuel moisture $W_{\mathscr{M}}$ based on vigor $V_{\mathscr{M}}$ using Eq. (4.1)
9          end
10     end
11 Compute 2D spatial maps for grass, fine fuel, and duff:
12     For each cell in the grid, compute biomass $B_g$, $B_f$, $B_d$ as per Eqs. 4.6, 4.10, 4.11
13 end
```

We implemented our framework with C++ and CUDA. To facilitate the visualization of fire, we use volume ray casting [46], implemented with OpenGL and GLSL. This process simulates the behavior of light rays as they traverse the volume. Dynamic handling of tree geometries and leaves is accomplished within geometry shaders. This real-time visualization approach enables interactive exploration of our simulations.

In Algorithm 3 we show how to calculate moisture content and to create 2D fuel maps. First, we approximate local light conditions L (Line 1) to affect vegetation health and fuel availability. We then compute the fuel moisture content. For each plant $\mathscr{P}$ (Line 3), we calculate its environmental adaptation o (Line 4) using Eq. (4.28), distributes light flux Q across the plant graph H (Line 5) via Eq. (4.29), and does the same for vigor flux V (Line 6) with Eq. (4.32). Each module $\mathscr{M}$'s fuel moisture $W_{\mathscr{M}}$ is calculated (Line 8) using Eq. (4.1) based on vigor $V_{\mathscr{M}}$. In the second part (Lines 11-12), we create 2D maps of grass, fine fuel, and duff. We calculate biomass layers B_g, B_f, B_d per grid cell (Line 12) using Eqs. 4.6, 4.10, 4.11. Required inputs are a terrain model, plant graphs, atmosphere data, and soil map. The outputs are the moisture content and 2D fuel maps, preparing the system for wildfire simulation.

In Algorithm 4 we show how to perform the numerical simulations to update the system state. For each module $\mathscr{M}$ in the system (Line 1), we update the mass M (Line 2) following

Algorithm 4: Numerical procedure of our simulator.

```
Input: Current system state.
Output: Updated system state.
for each module $\mathscr{M} \in \bigcup \mathscr{P}$ do
    Update mass $M_{\mathscr{M}}$ according to Eq. (4.13).
    Update moisture $W_{\mathscr{M}}$ according to Eq. (4.2).
    Generate firebrands according to Eq. (4.21) and Eq. (4.22).
    Perform radii update according to Eq. (Hädrich et al. [21]).
    Update temperature $T_{\mathscr{M}}$ according to Eq. (4.17).
end
for each firebrand do
    Update mass $m_e$ according to Eq. (4.23).
    Update temperature $T_e$ according to Eq. (4.24).
    Update position and velocity by taking drag into account.
    Check intersection with modules and bottom boundary layer.
    Compute ignition event according to Eq. (4.25).
end
for each grid cell $x$ in fuel layers $B_g$, $B_f$, $B_d$ do
    Update masses $M_g$,$M_f$,$M_d$ according to Eq. (4.13).
    Update moisture $W_g$,$W_f$,$W_d$ according to Eq. (4.12)
    Update temperatures $T_g$, $T_f$, $T_d$ according to Eqs. 4.18, 4.19, 4.20.
end
for each cell $x$ in atmospheric grid do
    Update $M_s := M_s(x,t)$ and $W_s := W_s(x,t)$ as described in Section 4.5.6.
    Update temperature $T_a$ according to Eq. (4.16).
end
Update drag forces $f_d$ and buoyancy force $b$ according to Hädrich et al. [21].
Update $q_v$, $q_s$, and $u$ according to Hädrich et al. [21] and Sec. 4.5.3 including
  vorticity confinement with intensity $\varepsilon$, the advection of $u$ is upgraded to
  MacCormack method [56] (advection of other scalars is still solved with
  Semi-Lagrange but their back-trace operations are upgraded to RK-2).
Update $q_w$ according to Eq. (4.4).
for each module $\mathscr{M} \in \bigcup \mathscr{P}$ do
    if $M_{\mathscr{M}} = 0$ then $\mathscr{P} \leftarrow \mathscr{P} \setminus (\{\mathscr{M}\} \cup \mathsf{descendants}(\mathscr{M}))$
end
```

Eq. (4.13). The moisture W is then updated (Line 3) via Eq. (4.2), and radii are adjusted according to Hädrich et al. (Line 5). Temperature $T_{\mathscr{M}}$ updates then follow Eq. (4.17) (Line 6). Next, for each firebrand we update their mass, temperature, position, velocity, and check for potential ignition with vegetation (Lines 9-13). Subsequently, for each grid cell in fuel layers B_g, B_f, B_d (Line 15), we update masses M_g,M_f,M_d (Line 16) and moisture W_g,W_f,W_d (Line 17) similarly to Eq. (4.13) and Eq. (4.2). Then, we update temperatures T_g, T_f, T_d (Line 18) according to Eqs. 4.18, 4.19, 4.20. Next, for each cell in the atmospheric grid (Line 20), we update M_s and W_s (Line 21) as detailed in Section 4.5.6. We then adjust temperature T_a (Line 22) according to Eq. (4.16). Then, we modify drag forces f_d and buoyancy force b (Line 24). Further, we update q_v, q_s, and u according to Hädrich et al., incorporating vorticity confinement with intensity ε and MacCormack method for u's advection (Line 25). We then proceed to update q_w (Line 26) based on Eq. (4.4). In the last loop, if a module $\mathscr{M}$'s mass becomes zero, the module and its descendants are removed from the proper plant $\mathscr{P}$ (Line 28). This procedure operates on the current system state to generate an updated system state.

4.6.1 Numerical procedure

In the *Fire in Paradise* framework [21], the authors adopted the semi-Lagrangian scheme from the influential paper by Stam [59] to solve the advection term of the Navier-Stokes equation. This approach, while unconditionally stable, has been recognized to lead to significant numerical diffusion, a limitation that we aimed to overcome. To this end, we employ the unconditionally stable MacCormack scheme [56], which has been shown to not only effectively reduce numerical diffusion but also to achieve second-order accuracy, making it a superior choice for our purposes. For the ember transport we use the forward Euler method.

Additionally, we made enhancements to the back trace operations of the advection terms of all related equations, including the Navier-Stokes equation. To increase the precision of these operations, we implemented the second-order Runge-Kutta (RK-2) scheme in place of the previous first-order method. This modification is expected to offer improved accuracy and overall performance of our model. By combining these improvements, we aim to deliver a more robust and accurate wildfire simulation.

Fig. 4.7 exposes the significant amount of turbulence which occurs during our wildfire simulations. These turbulences are absent when solving with the semi-Lagrangian scheme (Figure 4.8 To quantify the difference between the MacCormack and the semi-Lagrangian scheme, we measured the average kinetic energy for each grid point in the domains, which indicates a 19.35% higher turbulence for the MacCormack scheme. This increase in turbulence is a direct consequence of the reduction in numerical diffusion achieved through our enhancements to the advection solution method. Such a result is significant as it allows a more advanced simulation of turbulent phenomena of wildfire simulations.

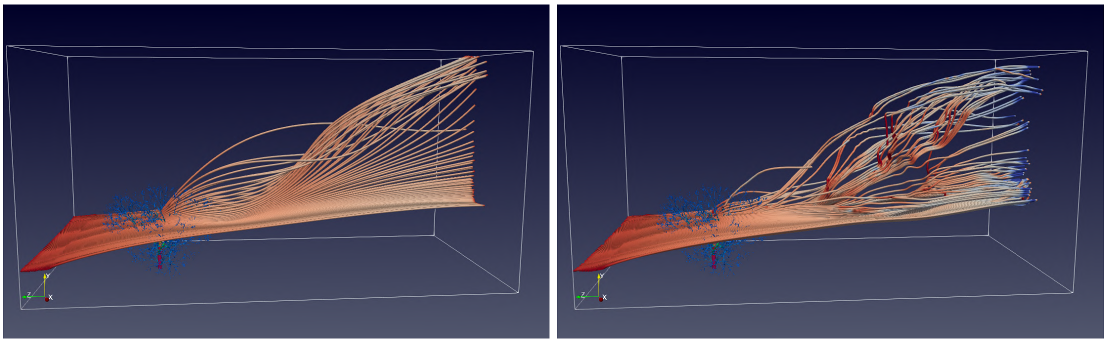

Figure 4.8 A side-by-side comparison of the wildfire simulations before (left) and after (right) the application of the numerical changes in our study. The simulation domain is marked by a box with white borders, and the resolution of this domain is set at $64 \times 64 \times 128$. Visualization of both the tree and the streamlines has been accomplished using the ParaView software. Color-coding of streamlines indicates wind speeds, while tree branches are colored according to their respective radii.

4.6.2 Initial Conditions

We set values for physical parameters of our simulations with readily available observational data, such as T_a, or q_w, according to plausible ranges obtained from the literature. Other parameters can be derived from observational data but might be accurate only in certain conditions, such as k which can be derived from controlled combustion experiments, W_g which can be derived from soil moisture measurements and known water retention properties of the biomass, or σ_f which can be derived from the observed spread of fine fuels around plants. Obtaining parameter values from observational data can be challenging for variables such as species-specific adaptive parameters like T_A, L_A, and P_A, biological growth parameters such as ϖ_g, kernel functions involved in fuel mapping exemplified by $G_f(x,y)$, and parameters governing thermal and moisture transfer, for instance, K_{ij}. However, we use various research sources to guide our selection of parameter values such as Vanella et al. [63] to estimate max biomass of fine fuel, grass, duff ϖ_g, ϖ_f, ϖ_d, Bishop [8] to estimate moisture content per plant species ψ, and Hadden et al. [19] to set thermal conductivity K_{ij} and combustion heat rate ΔH_c. We also demonstrate that our parameter value selections result in simulations which compare favourably with simulations obtained with the analytical model from Rothermel and a real world burn experiment (Fig.4.15). For most scenes we use the same initial conditions. A typical list of parameter values used in the simulations we describe here can be found in Appendix 4.10.4.

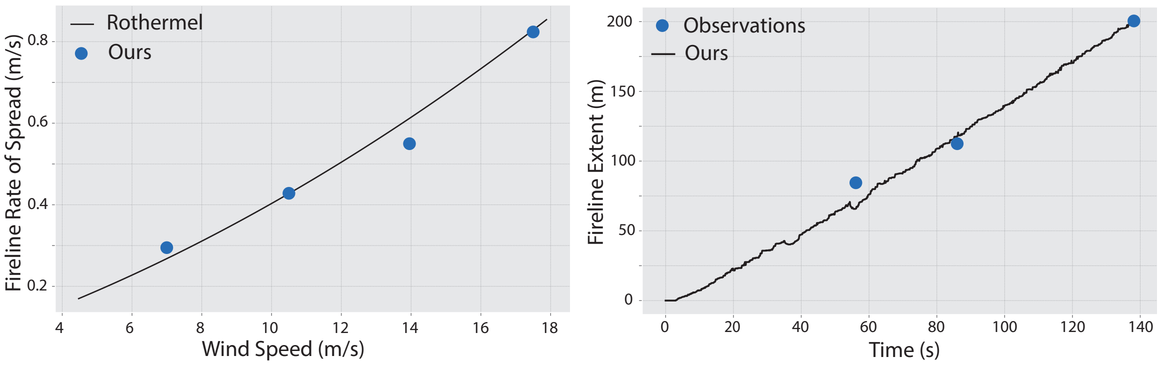

Figure 4.9 Left: A comparison of the rate of fire spread of the fireline using Rothermel's model configured for crown fuel [8] (solid line) and our simulation results for four experiments with varying wind speeds. Our simulation results correspond well to Rothermel's model. Right: A comparison of the maximum extent of firelines in our simulation (solid line) to measurements of the controlled burn experiment shown in Fig. 4.9 at three different time points (blue dots). Our simulation captures accurately the linear progression of the fireline.

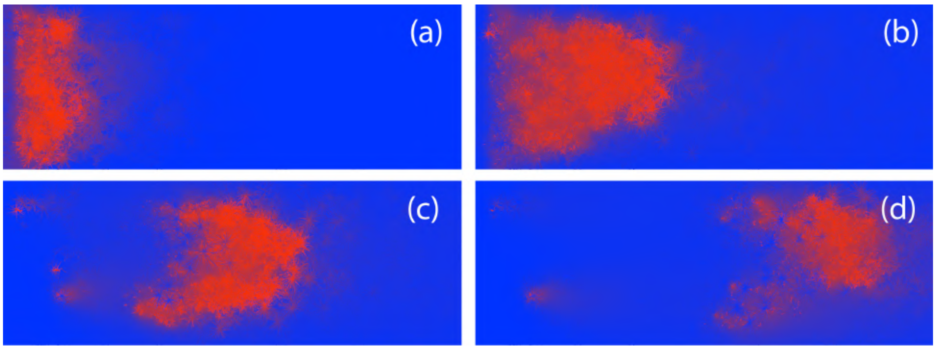

Figure 4.10 Heat map of a top down view on a burning forest patch with a wind field directed from left to right. Red color indicates temperature. Letters a-d indicate the temporal progression of the crown fire. The rate of spread of the fireline is approximately constant over time. We use this setup to generate the simulation results of varying wind speeds to compute the data points shown in Fig. 4.9 (left).

4.7 Results

To showcase our wildfire simulation framework we present qualitative results obtained from various experiments. Specifically, we show that our model can generate known wildfire types, the distinct ranks of wildfires, and wildfires for different types of biomes (Fig. 4.13). Our model also supports exploring human cultivation factors for wildfire prevention, such as removing trees and shrubs from ecosystems. We validate our simulations with real-world experimental results.

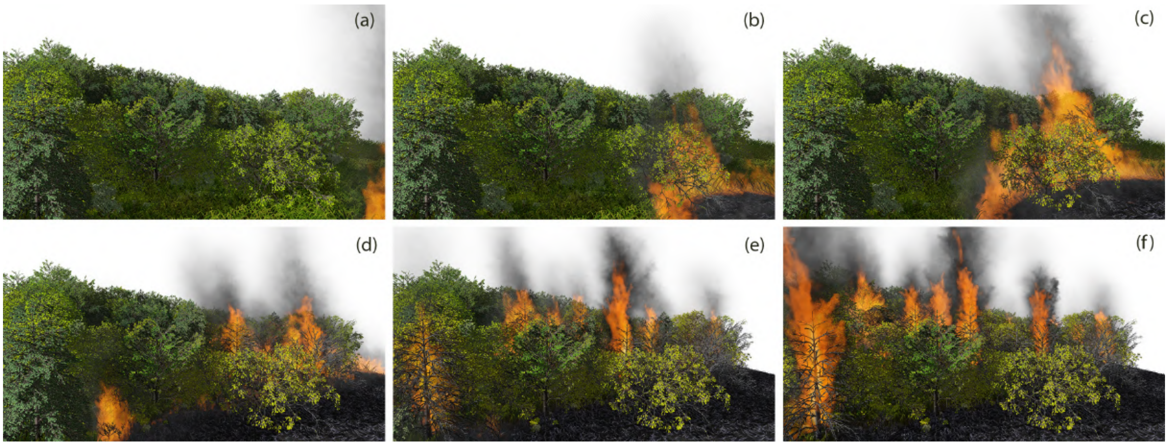

Figure 4.11 Progression of wildfire from grassland to forest edge: Initial fire ignition in grassland (a). Fire spreads, establishing as a surface fire (b). Fire reaches the forest edge, with the lower branches beginning to combust (c). Fire's transition from surface to active crown fire begins as it ascends the trees (d). Full transition to active crown fire, showing high-intensity flames within the forest canopy (e). Fire progresses further into the forest, vertical maintaining its status as an active crown fire with flame jets emerging (f).

4.7.1 Types of Wildfires

Table 4.1 Overview of the different parameter value configurations of simulations presented in Fig. 4.12. For each scene, the spatial dimensions are x = 70, y = 48, z = 128 with a spatial resolution (Δx) of 1 meter, $\varpi_d = 0.15$, $\varpi_f = 0.1$, $\varpi_g = 0.1$, and a constant time step size of $\Delta t = 0.0125$ s. The wind force for all scenes is set at 12 m/s. There were a total of 3749 plants in the scene composed of 114550 modules. Each simulation scene is characterized by the exact same setup except we vary the eight variables: W_{min}, $\psi_{\mathscr{M}}$, ϖ_g, ψ_g, ϖ_f, ψ_f, ϖ_d, and ψ_d.

Figure	**Scene**	W_{min}	$\psi_{\mathscr{M}}$	ψ_g	ψ_f	ψ_d
Fig. 4.12a	Wildfire Rank 2	0.4	1.0	0.36	0.48	0.36
Fig. 4.12b	Wildfire Rank 3	0.4	1.0	0.1	0.32	0.24
Fig. 4.12c	Wildfire Rank 4	0.3	1.0	0.1	0.32	0.24
Fig. 4.12d	Wildfire Rank 5	0.5	0.7	0.07	0.2	0.16
Fig. 4.12e	Wildfire Rank 6	0.5	0.5	0.05	0.16	0.12

Our wildfire model offers the capability of simulating a range of wildfire types, from Rank 1 to Rank 6 using the Wildfire Ranking System proposed by the British Columbia Wildfire Services[1]. Wildfires of different ranks can be simulated by adjusting the fuel moisture content of the plant modules. Each rank represents a different level of fire intensity and propagation rate, associated with the fire's interaction with different types of fuels present in the ecosystem. Rank 1, ground fires, typically occur in the organic matter present on the

---

[1] https://www2.gov.bc.ca/

Figure 4.12 By modulating overall fuel moisture content in the boundary fuel layer and plant modules our wildfire model allows the simulation of different wildfire dynamics, ranging from various types of surface fires (a,b) to crown fires (c-e).

forest floor, known as duff. These fires burn slowly, producing relatively small flames. By increasing the moisture content in the duff layer, our model simulates ground fires. Surface fires, or Rank 2 to 3 fires, involve the combustion of vegetation at the forest floor (leaf litter, and small branches), represented in our model as fine fuel and grass (Fig. 4.11a,b and Fig. 4.12a,b). Adjusting the moisture content within these components allows us to control the spread and intensity of surface fires (Table 4.1). Finally, crown fires, ranks 4 to 6, are the most intense and fast-moving fires, consuming both the surface and canopy fuels (Fig. 4.11c-e and Fig. 4.12c-e). The range of different wildfires is simulated in our model by manipulating moisture content within tree modules and the boundary fuel layer. When fuel moisture is low, our model simulates a rapid vertical fire spread, leading to an intuitive control of wildfire severity through fuel moisture parameters.

In Fig. 4.10 we show a temporal progression of a crown fire in a narrow forest patch as a heat map. Red colors indicate higher temperatures. The fireline progresses from left to right because we apply a wind field in that direction. We computed average velocities for the fireline for different wind speed experiments using our simulation framework. Fig. 4.9 (left) shows a comparison of four simulation runs with different wind speeds and a corresponding parameterization of Rothermel's model for crown fires [8]. As shown, our simulation runs conform to the Rothermel curve indicating a plausbile simulation of fireline progression with our modeling framework.

4.7.2 Human Intervention

By considering different fuel types our wildfire simulation allows assessing the impact of various human intervention methods. An important method is vegetation management to minimize the potential for severe wildfires. In Fig. 4.14 we show simulation results for different cultivation scenarios and their impact on wildfire progression. In the first scenario (Fig. 4.14a), the simulation depicts a dense, uncultivated grove with an abundance of vertical fuel resources represented by trees of various heights. As expected, these conditions lead to an intense and rapidly spreading wildfire due to the large amount of fuel. In contrast, Fig. 4.14b shows a human cultivation scenario, where medium-sized trees have been removed. The results depict a decrease in both the intensity and spread of the simulated wildfires. Lastly, Fig. 4.14c shows a more severe cutback of the vegetation – even smaller shrubs have been removed. Here, the scarcity of vertical fuel resources results in a less severe surface fire. These outcomes underscore the potential effectiveness of strategic vegetation management for mitigating the impact of wildfires.

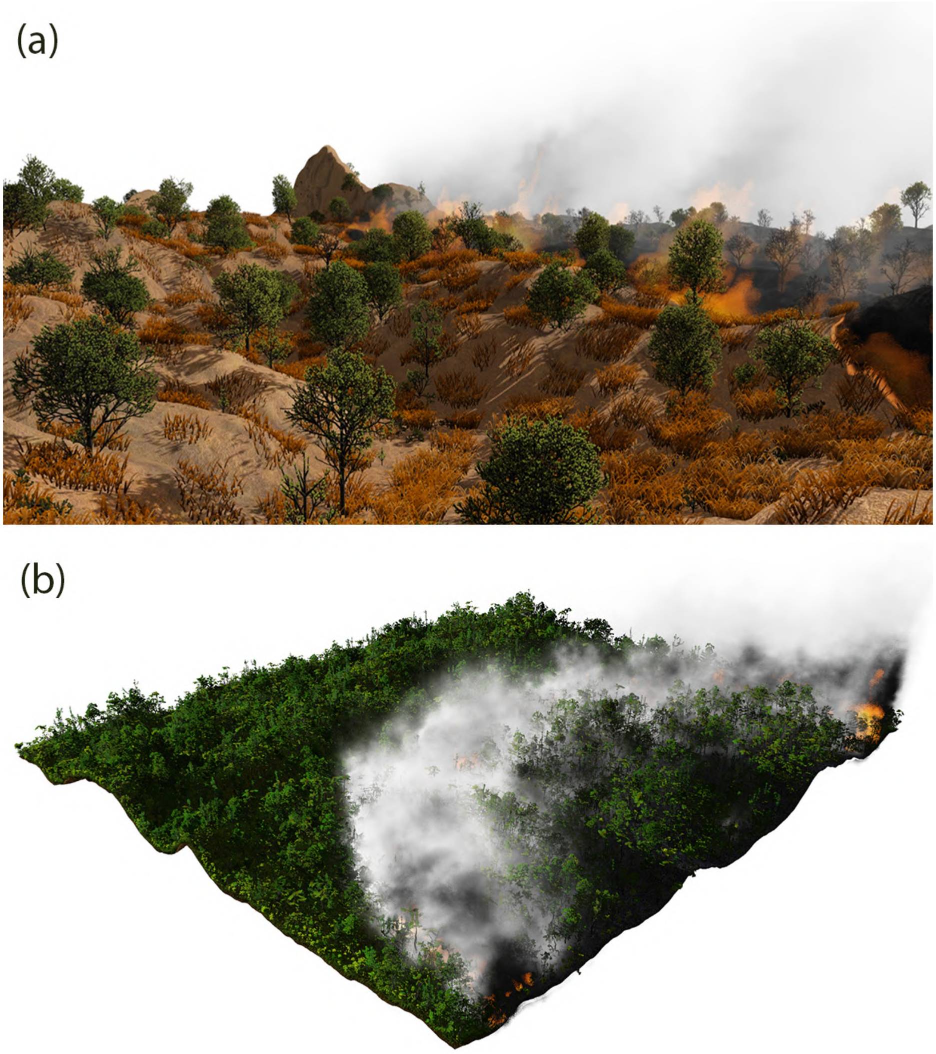

Figure 4.13 Renderings showing two different biomes: A close-up of a shrubland fire in the savannah (a) and a wildfire in the jungle characterized by high evaporation (b).

4.7.3 Boundary Fuel Wildfire Simulation

Fireline validation. To validate our wildfire model, we carried out comparisons with real-world experimental results. We prepared a simulation with a uniform grass concentration over a flat terrain of the size 200m x 200m. The fire was initiated along the left edge of the scene following the details provided in [63]. This study involved controlled burns and provides detailed observations and measurements that offer a suitable benchmark for our model. In these experiments, fires were ignited by two field workers with drip torches, who walked in opposite directions along the upwind boundary of the plot. We simulate an identical ignition process in our framework. Our simulated fireline progression shows remarkable similarity with the experimentally observed fire progression documented in the study. The shape,

Figure 4.14 Wildfire progression in varying cultivation scenarios. (a) Wildfire simulation in a dense, uncultivated grove with abundant vertical fuel resources in the form of trees of various heights, leading to intense and rapidly spreading wildfires. (b) Illustrates the effects of human cultivation efforts on wildfire behavior, represented by a scenario where medium-sized trees have been removed, resulting in a decrease in fire intensity and spread. (c) Further cultivation effects represented by a scene with minimal shrub presence; the scarcity of vertical fuel resources results primarily in a less severe surface fire.

direction, and general characteristics of fire spread in our model replicates the main features of the fireline from the experimental results (Fig. 4.15). We also quantitatively compared the extent of the fireline to the observations of a controlled burn experiment (Fig. 4.15, right). The plot shows the close correspondence of our simulation results to real-world measurements of a fireline in three different time points. We overlay our simulated fireline (red contour) with the observed measurements (dots, squares, triangles) and the results of the simulation by Vanella et al. [63] for clarity.

Boundary fuel distribution. In the controlled burn scenario a symmetric fireline progression emerges. However, in reality firelines often show more intricate progression dynamics. The dispersion pattern of fine fuel spots can, for example, instigate a localized retardation in the progression of the fireline, which can lead to an emergent complexity of the wildfire's structure. In Fig. 4.16 we show a temporal progression of a wildfire initiated at the left side of the scene. An uneven distribution of fine fuel (indicated by greener areas) leads to an uneven fireline advancement. A wildfire in such a fuel environment is characterized by the creation of *fingers* which are extended, narrow protrusions of the fireline that reach further into unburnt areas (Fig. 4.16a-c). Similarly, the fireline can retract or slow down in

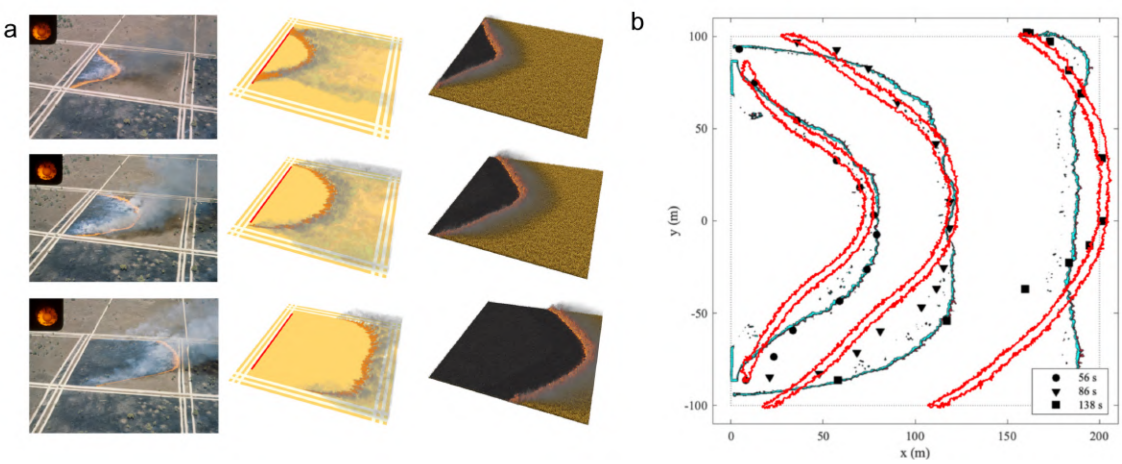

Figure 4.15 (a) Photographs of a controlled burn experiment (left), results of a wildfire simulation published by Vanella et al. [63] (middle), and our simulation results (right). Our simulation captures the main characteristics of the progressing fireline in the controlled burn experiment. (b) Comparison of the fireline of a real burn experiment (dots, squares, triangles) at three different time points with our simulated fireline contour (red) and the results of a wildfire simulation conducted by Vanella et al. [63] (teal contour).

areas of lower fuel availability, leading to the formation of *bays* –recesses or indentations in the fireline that represent areas where the fire has not yet or may not reach. This gives the fireline a unique, irregular shape, further enhancing the visual and dynamical realism of the simulation (Fig. 4.16e). Furthermore, if the fireline encircles an area of unburnt vegetation, it may result in the creation of *islands*. These are patches of unburnt vegetation surrounded by burnt areas, signifying the heterogeneity in fire propagation due to fine-scale variations in fuel distribution (Fig. 4.16d).

Fuel moisture effect. A key advantage of our approach is that it allows us to capture the complexities of fireline progression dynamics that account for variable fuel moisture. In particular, the simulation results have demonstrated the crucial role of fuel moisture distribution in modulating the spread and behavior of wildfires. In scenarios where shrubs — which typically contain higher fuel moisture compared to grass — are distributed within a grassland, our simulation shows that they can act as a natural barrier to the progression of fire (Fig. 4.17a). Specifically, the fireline is observed to navigate around these denser lines of shrubs, selecting paths where the shrub density – and consequently the fuel moisture content – is lower (Fig. 4.17b, c). This behavior shows that the wildfire is attracted by areas of lower fuel moisture, leading to a more realistic and complex fireline progression pattern. To test the influence of fuel moisture content further, we conducted a second experiment where the fuel moisture content of the shrubs was reduced. The results of this experiment show a less pronounced retardation of the fireline progression around the shrubs (Fig. 4.17d-f). This

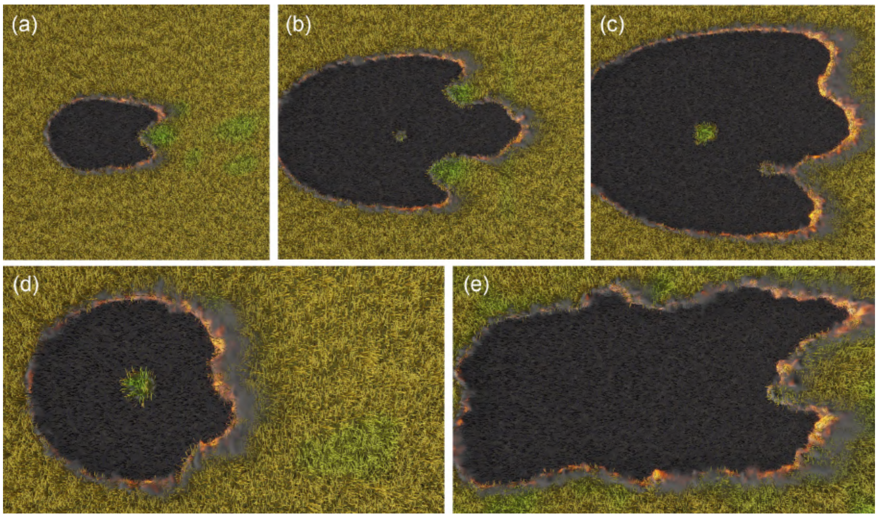

Figure 4.16 (a): Initial configuration showing the ecosystem with the distribution of fine fuel spots (indicated by greener color). (b): Early stages of fireline progression with local delays evident at fine fuel spots. (c): Intermediate stage of the wildfire, displaying complex progression dynamics including finger formations. (d): Advanced stage, where bay and island formations become apparent due to the localized slowing of the fireline at the fine fuel spots. (e): Final state of the wildfire highlighting the intricate anatomy shaped by the distribution of fine fuel.

outcome shows that fuel moisture content plays a significant role in defining the rate and direction of wildfire spread.

Ember Influence and Wind Dynamics. The simulation results depicted in in (Fig. 4.17 g-i) incorporate the ember model. These simulations differ from the previous grassland wildfire due to the emergence of new ignition points that advance the fireline (g, j, k), resulting in a more linear fireline front. This linearization is a direct consequence of embers migrating in the immediate area of the primary fireline and starting auxiliary fires that eventually merge with the main front. Subsequent frames (Fig. 4.17 j-l) introduce a wind field from the left to right. This interaction leads to ignition points appearing further from the primary fireline, leading to complex shapes of wildfire progression. Our simulations with the ember model and varying fuel moisture distribution showcase the unpredictable nature of wildfire spread, emphasizing the need for detailed, spatial models in wildfire research.

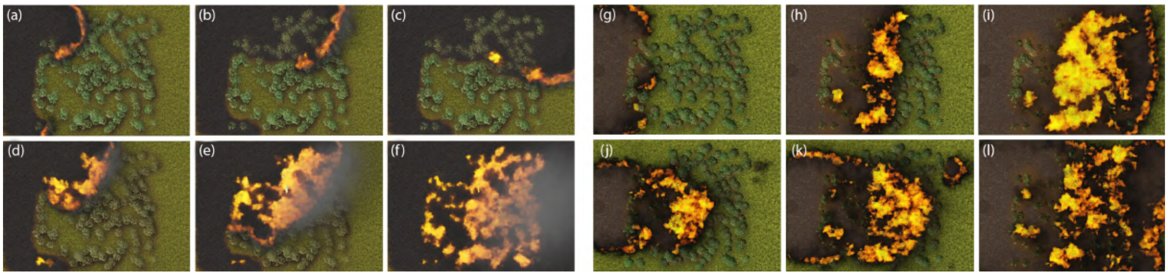

Figure 4.17 The initial state of a grassland ecosystem interspersed with moisture-rich shrubs viewed from above without ember model (a). Simulation result showing the progression of the wildfire, which avoids the dense line of shrubs due to their higher fuel moisture content (b). Final state of the wildfire progression showing the protective role of moisture-rich shrubs against fire spread (c). In the row below (d-f), we show the same scene but with lowered fuel moisture values for the shrubs. In this case, the wildfire simulation results in complete conflagration. In (g-i) we show a simulation with the ember model. In this case a new spot fire ahead of the fireline emerges in (g) and leads to a straighter fireline compared to the two top rows. In (j-l) we add wind from left to right which results in new spot fires appearing further away from the fireline (j, k). The interplay between fuel moisture distribution and firebrand simulation leads to complex fireline shapes in our wildfire simulations.

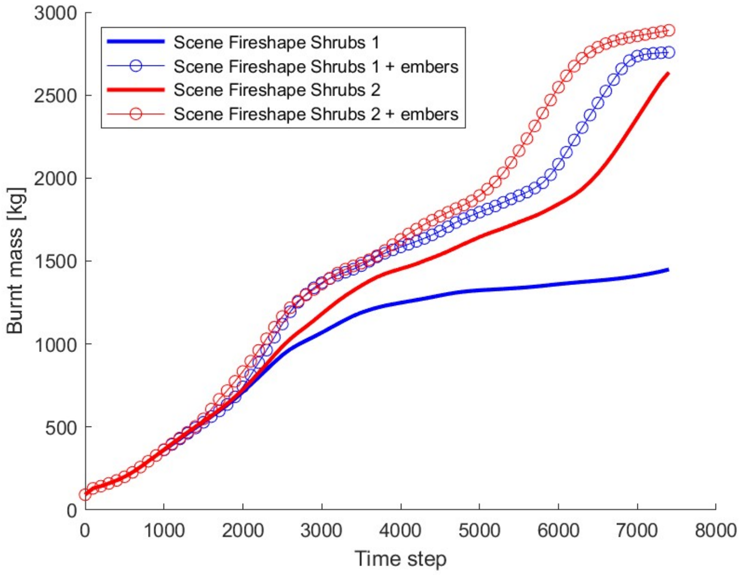

Figure 4.18 This plot depicts a quantitative ablation study of the ember model shown in the results in Fig. 4.17. The hill-shaped blue line indicates biomass loss as a function of time for the model without embers is contrasted with a more complex curve shape of the experiment with ember model - due to the non-linear nature of wildfires with embers. The red line indicates the mass loss evolution for a drier scene. Here, the difference between the models is less noticeable.

Table 4.2 Performance characteristics for various wildfire simulations. The table presents the grid size, the number of trees and modules in the simulation, the memory used, and the duration of each simulation step for different scenes. The time-step is 45 seconds.

Figure	**Scene**	**Grid Size**	Cell Size	Modules	Plants	Memory	Step Duration
Fig. 4.19	Mountain Forest	405x405x250	1m	886,293	202,301	23GB	201.3ms
Fig. 4.14b	Cultivated Forest	576x320x560	0.125m	29,158	1,582	22GB	220ms
Fig. 4.13b	Rainforest	405x405x150	1m	254,843	61,820	12GB	65ms

4.8 Discussion and Limitations

We have presented a method for simulating realistic wildfires across a variety of scenarios. The key novelty of our approach is the detailed description of vegetation that includes fuel moisture, the interaction with other fuels encapsulated in our method as the boundary fuel model, and a validation over a large number of key wildfire phenomena such as different wildfire types and wildfire anatomical parts. The validation against a controlled burn experiment indicates that our model can accurately simulate wildfire progression under certain conditions. As indicated by our results, our method offers intuitive control for generating wildfires of variable severity and type by manually setting fuel moisture parameters or managing the vegetation distribution in the scene. Furthermore, many aspects of our model could be calibrated using empirical observations or established analytical approaches such as fire spread rates provided by the Rothermel model [4] to increase usefulness towards real-world applications.

One of the main limitations of our framework is the scale of the scenes we are currently able to process (Fig. 4.19). While the geometric detail of vegetation significantly improves the fidelity of wildfire simulations, it imposes considerable memory demands that limit the size of the ecosystems we can simulate in real-time. This constraint presents a challenge in the context of real-world wildfires, which often span vast geographical areas. We need to address this memory limitation in order to realize the full potential of our simulation in the accurate prediction and management of large-scale wildfires. Our simulation would also benefit from a more detailed soil model to better represent the contribution of ground fires, the inclusion of fire-induced phenomena such as spotting and fire whirls, which can significantly influence fire spread and intensity. We also aim to refine our model parameters and assumptions based on further validation studies and expert feedback.

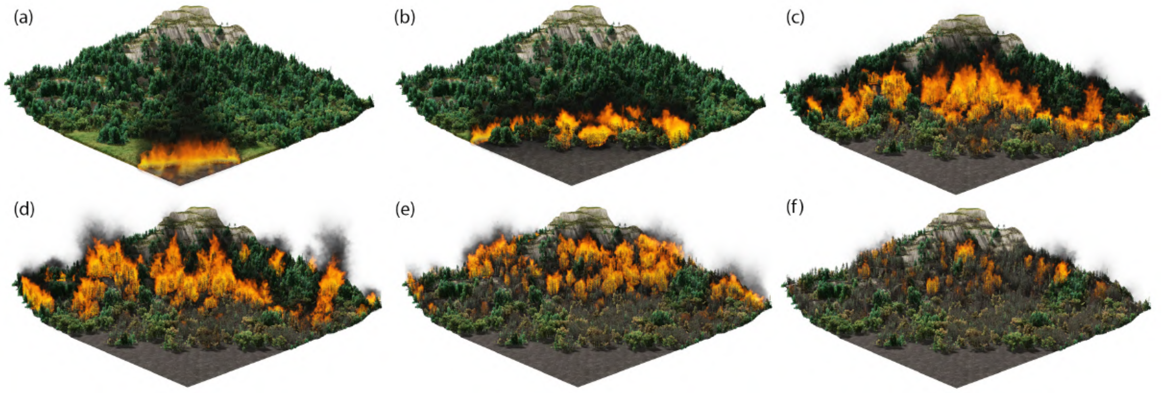

Figure 4.19 A larger wildfire scene with around 200K plants composed of almost 1000K modules simulated at interactive rates. The wildfire starts as a grass fire progressing towards a forest edge (a). Once the fireline enters the forest some trees start combusting while others resist ignition due to the effects of fuel moisture (b). Eventually, the wildfire spreads to the crowns of trees and becomes more destructive (c). Due to the burning crowns, a lot of firebrands are generated which cause new fire sources ahead of the fireline (d). The wildfire progresses in a complex fireline higher up the mountain side (e). Finally, as most of the fuel is consumed by the flames the wildfire wanes and exposes the burnt down trees in the forest (f).

4.9 Conclusion

In this chapter, we have presented a novel model for wildfire simulations that offers several significant advancements over existing models in the field. Our model captures key wildfire behaviours, such as surface, ground, and crown fires, in an accurate and computationally efficient manner addressing Hypothesis 1. One of the major strengths of our model lies in its ability to simulate wildfires across various biomes, a feature that contributes to its broad applicability. These phenomena could not be simulated before and advance the state-of-the-art in computer graphics and beyond. Moreover, the model has been validated using real-world controlled burn experiments in fields, demonstrating its capability to reproduce important features of fireline progression. Our innovative approach to fuel moisture modelling allows us to dynamically track moisture content in fuels and to set up complex vegetation scenes for wildfire simulations. Vegetation distribution is an important factor in wildfire behavior which means that the explicit consideration of a detailed vegetation model as well as a boundary fuel layer enhances the realism of our simulation.

Unlike many existing wildfire simulations, our model operates at interactive timescales, a significant advantage that opens up possibilities for real-time or near-real-time applications, especially beneficial for firefighting services. Our model shows to be a promising tool for both research and practical applications in wildfire management. By integrating different paradigms we were able to model each wildfire domain separately using the most effective approach, which in turn resulted in fast simulation. By using a separate boundary fuel model for small plants we were able to overcome boundary slip conditions and still use a relatively coarse grid. Similarly, by using the off-grid model of vegetation we could achieve a more complex geometry of the tree than the voxel grid would allow us. However, this approach requires careful evaluation when it comes to the integration of these models, as we are required to consider how each two components should interact with each other. A hybrid approach was essential to achieve interactive rates aligning with Hypothesis 2.

Looking forward, we see several avenues for further improvement. One key focus will be the ability to simulate larger wildfire scenes. The scale of wildfires is a significant factor in their development and visual impression, and we aim to accurately capture these large-scale phenomena in our simulations. To achieve this, we plan to employ level-of-detail techniques, which will help manage the computational cost while maintaining visual realism. Another area of potential development is expanding the comparisons of our model with real-world historical wildfires. Such comparisons will provide additional validations of the model's accuracy and will further enhance our understanding of wildfire dynamics and its visual representation. In conclusion, the advancements introduced in this study offer substantial potential for improving the visual realism and interactivity of wildfire simulations.

4.10 Appendix

4.10.1 Vegetation Model

We compute the environmental adaptation parameter $o \in [0,1]$ of a given plant based on local temperature and soil water availability as proposed by [31]. We sample the soil water availability q_w and atmospheric temperature T_a at the position where the plant is located. Next we compute a climatic adaptation parameter o as follows:

$$o = \frac{\mathcal{N}_T(T_a) \cdot \mathcal{N}_P(q_w)}{\mathcal{N}_T(T_A) \cdot \mathcal{N}_P(P_A)}, \tag{4.28}$$

where $\mathcal{N}_T(\cdot)$ and $\mathcal{N}_P(\cdot)$ denote the normal distributions of temperature and soil water, and T_A and P_A are plant type parameters defining the climatic adaptation of a given plant species to temperature and humidity.

Next, we evaluate light exposure values of the atmosphere space and propagate them as light flux through the plant graph H. Specifically, we sample the light exposure at the locations of all end nodes of plant graph H (except root nodes) and set light flux values Q_i of modules equal to light exposure values L. Then we propagate the values of light exposure as light flux Q of all end nodes downwards through the graph H summing them together at each module bifurcation point:

$$Q_i = Q_m + Q_c\,, \tag{4.29}$$

where Q_m denotes light flux from the main module and Q_c the light flux of the child module until the total light exposure value of all end nodes is computed at the base node as total light flux Q_p.

After calculating the light flux, we calculate the vigor values from the base node to the end nodes of the plant graph H. The vigor of a module is a measure of its physiological activity and health, which directly impacts its moisture content. Starting with the base node we determine the total vigor V_{root} available for the plant as

$$V_{root} = Q_p \cdot o\,. \tag{4.30}$$

This means that total vigor of a plant depends both on the total light availability to modules as well as its overall climatic adaptation to local temperature and soil water. Once we have computed the total vigor for the base module, we propagate vigor V as vigor flux upwards in the plant graph H by allocating vigor flux to main or child modules. At each branching point, we determine the distribution of vigor towards the next node of the current module (V_m) and the node of the child module (V_c) based on the vigor of the parent module (V_p):

$$V_m = V_p \cdot \frac{\lambda(Q_m)}{\lambda(Q_m) + (1-\lambda)(Q_c)}\,, \tag{4.31}$$

$$V_c = (V_p - V_m)\,. \tag{4.32}$$

where the weight λ corresponds to the one introduced in [42], which is used to distinguish species-dependent preferences to develop vigorous branches. The notion of vigor in our model therefore conceptualizes the impact of local light conditions as well as species-dependent traits.

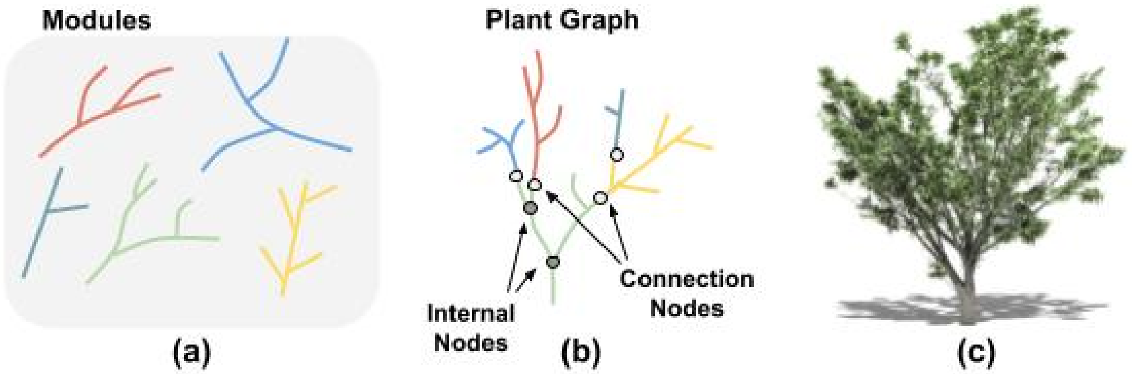

Figure 4.20 Our plant representation is module-based: Each plant is defined as a combination of modules (a), which are reused across the ecosystem by exploiting the repetitive structure of plants (b). After defining the branch graph, we generate the final plant geometry from the module-based graph description (c).

4.10.2 Scene Setup Parameters

L	Light exposure values
T_A, L_A, P_A	Adaptive parameters response to temperature, light, and soil water, respectively, for a given plant species or grass
ϖ_g, ϖ_f, ϖ_d	Maximum biomass of grass, fine fuel, and duff, respectively
$\mathscr{M}$	A module in a plant structure
$G_{\mathscr{M}}$	A graph describing a module
M	Mass of a plant module
Q	Light Flux of a plant module
v	Vigor of a plant module
$\mathscr{P}$	A plant
$H_{\mathscr{P}}$	A graph describing a plant
φ_f	Average fine fuel production of a plant
σ_f	Fine fuel spread of a plant
κ_p	Transpiration rate
o	Environmental adaptation parameter of a plant
Q_p	Total light flux available to the plant
V_{root}	Total vigor available to the plant
λ	Species-dependent preference to develop vigorous branches at the apex
ψ	Moisture content per plant species
W_{min}	Minimum fuel moisture value for a given plant species

B_g, B_f, B_d	Biomass value of a grid cell for grass, fine fuel, and duff layers, respectively
$G_f(x,y)$	Fine fuel kernel function
$G_d(x,y)$	Duff kernel function
σ_f	Standard deviation of the Gaussian in fine fuel kernel
μ_d^{opt}	Optimal moisture value for decomposition

4.10.3 Wildfire Simulation Parameters

T_a	Atmospheric temperature (°C)
q_v	Vapor content in the atmospheric model (kg/m^3)
q_s	Smoke in the atmosphere grid cell
u	Wind speed (m/s)
T_g, T_f, T_d	Temperature of grass, fine fuel, and duff, respectively (°C)
W_g, W_f, W_d	Moisture content of grass, fine fuel, and duff (%)
W	Moisture of a plant module (%)
Δq_w	Water diffusion in the soil ($kg/m^3 \cdot m/s$)
k	Reaction rate of the combusting fuel (rate units)
$T_{\mathscr{M}}$	Temperature of the module (°C)
$W_{\mathscr{M}}$	Total moisture of module (%)
c	Dimensionless char insulation parameter
A	Pyrolyzing front area (m^2)
T_0, T_1	Lower and upper temperature limits for combustion (°C)
W_0, W_1	Lower and upper moisture limits for combustion (%)
η	Function describing the impact of wind on the reaction rate
u_{ref}	Optimal wind speed for maximum boost to the reaction rate (m/s)
u	Velocity field (m/s)
K_{ij}	Thermal conductivity between domains i and j ($W/(m \cdot K)$)
α	Diffusion intensity
γ	Radiative cooling term
T_{amb}	Ambient temperature (°C)
M_s	Mass for grid cell (kg)
W_s	Water content in each grid cell (%)
T_m	Module's surface temperature (°C)
α_m	Diffusion coefficient for modules (m^2/s)
b	Temperature coefficient for modules
D_g, D_f, D_d	Diffusion coefficients for grass, fine fuel, and duff (m^2/s)
$\kappa_w^m(T_{\mathscr{M}})A$	Evaporation function for another module (e.g., vegetation), dependent on the module temperature $T_{\mathscr{M}}$ ($1/s$), multiplied by area A (m^2)
$S_{T_0^d,T_1^d}(T_d)$	Smoothstep function for evaporation in the duff layer, defined between two temperature limits T_0^d and T_1^d (°C)
ΔH_x	combustion heat rate for specific domain x

A_g	Grass pre-exponential factor
ρ_g	Grass density (derived from biomass)
r_{cr}	Minimum particle radius necessary for ignition
E	Activation energy
R	Universal gas constant

4.10.4 Parameter Values

Table 4.3 Overview of the wildfire simulation parameters and their corresponding values for the ember simulation shown in Fig. 4.17 (g-i).

Parameter	**Symbol**	**Value**
Vorticity Confinement	c	30.0
Eta	η	10
DX	Δx	1
Initial Water Multiplier	W_{min}	0.33
Wind Velocity	$u(x,z)$	(12, 10)
Fine Fuel Burn Rate	k	1
Duff Burn Rate	ϖ_d	1
Grass Burn Rate	ϖ_g	3.7
Grass Diffusion Rate	D_g	0.8
Fine Fuel Rate	ϖ_f	0.5
Fire Temperature Cooling	γ	0.0015
Min Water Burn	W_{min}	0.03
Grass Mass	B_g	0.2
Grass Water	W_g	0.1
Fuel Mass	B_f	0.2
Fuel Water	W_f	0.8
Duff Mass	B_d	0.1
Duff Water	W_d	0.2

Chapter 5

Conclusion

Throughout this thesis, I present various mathematical models designed to address specific natural phenomena of different scales in both temporal and spatial dimensions. Such variety required careful consideration of each research problem. I dedicated a significant part of my efforts to understanding them and finding an appropriate formalism and level of detail for their description. Creating an adequate mathematical representation requires balancing the complexity of the project. Too simple a model won't be able to express the process. Meanwhile, excessive complexity can hinder our ability to validate it efficiently and understand the biological underpinnings.

Through careful validation of these models, I aimed to assess three theses posed in the first chapter. This process serves as a broader understanding of the potential and limitations of computational methods and their applicability across different scales and contexts in biological research.

Hypothesis 1: Computational models can simulate complex biological systems.

Each chapter presents models simulating phenomena at different scales. Chapter 2 describes a model of vascular pattern formation in Arabidopsis Thaliana at the cellular level. In Chapter 3 we move larger systems, applying differential equations to understand long-distance signalling in trees. Chapter 4 demonstrates a hybrid model on an ecological scale, simulating wildfire dynamics using sophisticated computational techniques.

Hypothesis 2: Different modelling approaches are necessary to address the unique challenges presented by different biological phenomena.

Every model presented in the thesis was created under a different design paradigm. They were evaluated in terms of applicability. The key findings are as follows.

A discrete paradigm is more natural if the observation of phenomena weighs heavier on a descriptive than a prescriptive side. Similarly, it is more effective when questions regarding studied phenomena are qualitative than quantitative (e.g. Question if vascular connection occurs), aside from that it allows for fast testing on various hypotheses by modifying certain assumptions, without additional retuning of parameters.

Conversely, a continuous approach is more suitable when the question is qualitative. Aside from that these types of methods are more effective when conducting optimisation or sensitivity analysis. Due to their smooth nature, they are easier to control and we can employ a wide array of tools from mathematical analysis to study them.

A sophisticated hybrid model, in which we combine different paradigms is essential to achieve efficient simulation of a complex phenomenon that spans various domains. These methods enable us to use the most effective method for simulating each domain. Establishing communication between these domains is a crucial task, that requires careful consideration and validation.

Hypothesis 3: Modelling can be used to assess hypothetical biological mechanisms and discover areas where more comprehensive research is needed.

Each model was validated against the experimental data and highlighted areas requiring further study. For instance, the ring experiments conducted in 2.6 provided an argument for the existence of a mechanism that synchronises iVs with auxin expression on the surface. Whereas LSM presented in 3 was based on the assumptions of biological hypothesis. Its conformation to experimental observation argues for this hypothesis.

In conclusion, this dissertation confirms the utility of computational models in advancing our understanding of biological phenomena. It demonstrates the necessity of employing diverse modelling techniques to address the challenges presented by biological systems, therefore supporting the initial hypotheses and highlighting the continued need for innovative computational approaches in biology.

Bibliography

[1] Abram, N. J., Henley, B. J., Sen Gupta, A., Lippmann, T. J. R., Clarke, H., Dowdy, A. J., Sharples, J. J., Nolan, R. H., Zhang, T., Wooster, M. J., Wurtzel, J. B., Meissner, K. J., Pitman, A. J., Ukkola, A. M., Murphy, B. P., Tapper, N. J., and Boer, M. M. (2021). Connections of climate change and variability to large and extreme forest fires in southeast australia. *Communications Earth & Environment*, 2(1):8.

[2] Adusumilli, S., Chaplen, J. E., and Blunck, D. L. (2021). Firebrand generation rates at the source for trees and a shrub. *Frontiers in Mechanical Engineering*, 7.

[3] Anand, C., Shotorban, B., Mahalingam, S., McAllister, S., and Weise, D. (2017). Physics-based modeling of live wildland fuel ignition experiments in the fist apparatus. *Combustion Science and Technology*, 189.

[4] Andrews, P. L. (2018). The rothermel surface fire spread model and associated developments: A comprehensive explanation. Technical report.

[5] Aragoneses, E. and Chuvieco, E. (2021). Generation and mapping of fuel types for fire risk assessment. *Fire*, 4(3).

[6] Bayer, E. M., Smith, R. S., Mandel, T., Nakayama, N., Sauer, M., Prusinkiewicz, P., and Kuhlemeier, C. (2009). Integration of transport-based models for phyllotaxis and midvein formation. *Genes Dev.*, 23(3):373–384.

[7] Benková, E., Michniewicz, M., Sauer, M., Teichmann, T., Seifertová, D., Jürgens, G., and Friml, J. (2003). Local, efflux-dependent auxin gradients as a common module for plant organ formation. *Cell*, 115(5):591–602.

[8] Bishop, J. (2007). Technical background of the fireline assessment method (flame). In *The Fire Environment–Innovations, Management, and Policy Conference Proceedings*, pages 27–74.

[9] Bohren, C. F. and Thorud, D. B. (1973). Two theoretical models of radiation heat transfer between forest trees and snowpacks. *Agric. For. Meteorol.*, 11:3 – 16.

[10] Cheney, N. P., Gould, J. S., and Catchpole, W. R. (1993). The influence of fuel, weather and fire shape variables on fire-spread in grasslands. *International Journal of Wildland Fire*, 3(1):31–44.

[11] Coen, J. L. (2013). Modeling wildland fires : A description of the coupled atmosphere-wildland fire environment model (cawfe).

[12] Cordonnier, G., Ecormier, P., Galin, E., Gain, J., Benes, B., and Cani, M.-P. (2018). Interactive generation of time-evolving, snow-covered landscapes with avalanches. *CGF*, 37(2):497–509.

[13] Cordonnier, G., Galin, E., Gain, J., Benes, B., Guérin, E., Peytavie, A., and Cani, M.-P. (2017). Authoring landscapes by combining ecosystem and terrain erosion simulation. *ACM Trans. Graph.*, 36(4).

[14] Dupuy, J.-L. and Larini, M. (2000). Fire spread through a porous forest fuel bed: a radiative and convective model including fire-induced flow effects. *International Journal of Wildland Fire*, 9(3):155–172.

[15] Encinas, L. H., White, S. H., del Rey, A. M., and Sánchez, G. R. (2007). Modelling forest fire spread using hexagonal cellular automata. *Appl. Math. Model.*, 31(6):1213 – 1227.

[16] Filippi, J.-B., Bosseur, F., Mari, C., and Lac, C. (2018). Simulation of a large wildfire in a coupled fire-atmosphere model. *Atmosphere*, 9:218.

[17] Gierer, A. and Meinhardt, H. (1972). A theory of biological pattern formation. *Kybernetik*, 12(1):30–39.

[18] Godin, C. and Caraglio, Y. (1998). A multiscale model of plant topological structures. *Journal of Theoretical Biology*, 191(1):1–46.

[19] Hadden, R. M., Scott, S., Lautenberger, C., and Fernandez-Pello, A. C. (2011). Ignition of combustible fuel beds by hot particles: An experimental and theoretical study. *Fire Technology*, 47:341–355.

[20] Hädrich, T., Banuti, D. T., Pałubicki, W., Pirk, S., and Michels, D. L. (2021a). Fire in paradise: Mesoscale simulation of wildfires. *ACM Trans. Graph.*, 40(4).

[21] Hädrich, T., Banuti, D. T., Pałubicki, W., Pirk, S., and Michels, D. L. (2021b). Fire in paradise: Mesoscale simulation of wildfires. *ACM Trans. on Graph.*, 40(4).

[22] Hartmann, F. P., Barbier de Reuille, P., and Kuhlemeier, C. (2019). Toward a 3d model of phyllotaxis based on a biochemically plausible auxin-transport mechanism. *PLOS Computational Biology*, 15(4).

[23] Heisler, M. G., Ohno, C., Das, P., Sieber, P., Reddy, G. V., Long, J. A., and Meyerowitz, E. M. (2005). Patterns of auxin transport and gene expression during primordium development revealed by live imaging of the arabidopsis inflorescence meristem. *Current Biology*, 15(21):1899–1911.

[24] Jönsson, H., Heisler, M. G., Shapiro, B. E., Meyerowitz, E. M., and Mjolsness, E. (2006). An auxin-driven polarized transport model for phyllotaxis. *Proceedings of the National Academy of Sciences*, 103(5):1633–1638.

[25] Kapp, K., Gain, J., Guérin, E., Galin, E., and Peytavie, A. (2020). Data-driven authoring of large-scale ecosystems. *ACM Trans. Graph.*

[26] Katan, J. and Perez, L. (2021). ABWiSE v1.0: toward an agent-based approach to simulating wildfire spread. *Natural Hazards and Earth System Sciences*, 21(10):3141–3160.

[27] Kokosza, A., Wrede, H., Esparza, D. G., Makowski, M., Liu, D. Michels, D. L., Pirk, S., and Pałubicki, W. (to appear). Scintilla: Simulating combustible vegetation for wildfires. *ACM Trans. Graph.*

[28] Lam, R., Sanchez-Gonzalez, A., Willson, M., Wirnsberger, P., Fortunato, M., Alet, F., Ravuri, S., Ewalds, T., Eaton-Rosen, Z., Hu, W., Merose, A., Hoyer, S., Holland, G., Vinyals, O., Stott, J., Pritzel, A., Mohamed, S., and Battaglia, P. (2023). Learning skillful medium-range global weather forecasting. *Science*, 382(6677):1416–1421.

[29] Lawes, M. J., Richards, A., Dathe, J., and Midgley, J. J. (2011). Bark thickness determines fire resistance of selected tree species from fire-prone tropical savanna in north australia. *Plant Ecol.*, 212(12):2057–2069.

[30] Lizhong, Y., Xiaojun, C., Xiaodong, Z., and Weicheng, F. (2002). A modified model of pyrolysis for charring materials in fire. *Int. J. Eng. Sci.*, 40(9):1011 – 1021.

[31] Makowski, M., Hädrich, T., Scheffczyk, J., Michels, D. L., Pirk, S., and Pałubicki, W. (2019). Synthetic silviculture: Multi-scale modeling of plant ecosystems. *ACM Trans. Graph.*, 38(4).

[32] Mandel, J., Kochanski, A., Vejmelka, M., and Beezley, J. (2014). Data assimilation of satellite fire detection in coupled atmosphere-fire simulation by wrf-sfire.

[33] Manzello, S. L., Maranghides, A., Shields, J. R., Mell, W. E., Hayashi, Y., and Nii, D. (2009). Mass and size distribution of firebrands generated from burning korean pine (pinus koraiensis) trees. *Fire and Materials*, 33(1):21–31.

[34] Masinda, M. M., Sun, L., Wang, G., and Hu, T. (2020). Moisture content thresholds for ignition and rate of fire spread for various dead fuels in northeast forest ecosystems of china. *Journal of Forestry Research*.

[35] McAllister, S., Chen, J., and Fernandez-Pello, A. (2011). *Fundamentals of Combustion Processes*. Mechanical Engineering Series. Springer New York.

[36] McGrattan, K., McDermott, R., Floyd, J., Hostikka, S., Forney, G., and Baum, H. (2012). Computational fluid dynamics modelling of fire. *International Journal of Computational Fluid Dynamics*, 26(6-8):349–361.

[37] Mell, W., Jenkins, M. A., Gould, J., and Cheney, P. (2007). A physics-based approach to modelling grassland fires. *International Journal of Wildland Fire*, 16(1):1–22.

[38] Mendoza, H., Brown, A., and Ricks, A. (2019). Modeling high heat flux combustion of coniferous trees using chemically reacting lagrangian particles. WSSCI Fall Technical Meeting of the Western States Section of the Combustion Institute.

[39] Mitchison, G. J. (1980). A model for vein formation in higher plants. *Proceedings of the Royal Society of London. Series B. Biological Sciences*, 207(1166):79–109.

[40] Monedero, S., Ramirez, J., Molina-Terrén, D., and Cardil, A. (2017). Simulating wildfires backwards in time from the final fire perimeter in point-functional fire models. *Environmental Modelling & Software*, 92:163 – 168.

[41] Niese, T., Pirk, S., Albrecht, M., Benes, B., and Deussen, O. (2022). Procedural urban forestry. *ACM Transaction on Graphics*, 41(1).

[42] Palubicki, W., Horel, K., Longay, S., Runions, A., Lane, B., Měch, R., and Prusinkiewicz, P. (2009). Self-organizing tree models for image synthesis. *ACM Transactions on Graphics*, 28(3):58:1–58:10.

[43] Pałubicki, W., Makowski, M., Gajda, W., Hädrich, T., Michels, D. L., and Pirk, S. (2022). Ecoclimates: Climate-response modeling of vegetation. *ACM Trans. Graph.*, 41(4).

[44] Pastor, E., Zárate, L., Planas, E., and Arnaldos, J. (2003). Mathematical models and calculation systems for the study of wildland fire behaviour. *Progress in Energy and Combustion Science*, 29(2):139 – 153.

[45] Pałubicki, W., Kokosza, A., and Burian, A. (2019). Formal description of plant morphogenesis. *Journal of Experimental Botany*, 70(14):3601–3613.

[46] Pharr, M., Jakob, W., and Humphreys, G. (2016). *Physically Based Rendering: From Theory to Implementation*. Morgan Kaufmann Publishers Inc., San Francisco, USA, 3rd edition.

[47] Pirk, S., Jarząbek, M., Hädrich, T., Michels, D. L., and Palubicki, W. (2017). Interactive wood combustion for botanical tree models. *ACM Trans. Graph.*, 36(6).

[48] Prusinkiewicz, P., Crawford, S., Smith, R. S., Ljung, K., Bennett, T., Ongaro, V., and Leyser, O. (2009). Control of bud activation by an auxin transport switch. *Proceedings of the National Academy of Sciences*, 106(41):17431–17436.

[49] Prusinkiewicz, P. and Lindenmayer, A. (1990). *The algorithmic beauty of plants*. Springer-Verlag, Berlin, Heidelberg.

[50] Reinhardt, D., Pesce, E.-R., Stieger, P., Mandel, T., Baltensperger, K., Bennett, M., Traas, J., Friml, J., and Kuhlemeier, C. (2003). Regulation of phyllotaxis by polar auxin transport. *Nature*, 426(6964):255–260.

[51] Richards, G. D. (1990). An elliptical growth model of forest fire fronts and its numerical solution. *International Journal for Numerical Methods in Engineering*, 30(6):1163–1179.

[52] Rolland-Lagan, A. and Prusinkiewicz, P. (2005). Reviewing models of auxin canalization in the context of leaf vein pattern formation in arabidopsis. *The Plant Journal*, 44(5):854–865.

[53] Runions, A., Smith, R. S., and Prusinkiewicz, P. (2014). Computational models of auxin-driven development. *Auxin and Its Role in Plant Development*, page 315–357.

[54] Schiller, L. and Naumann, Z. (1935). A drag coefficient correlation. *VDI Zeitung*, 77:318–320.

[55] Schwilk, D. W. (2003). Flammability is a niche construction trait: Canopy architecture affects fire intensity. *The American Naturalist*, 162(6):725–733.

[56] Selle, A., Fedkiw, R., Kim, B., Liu, Y., and Rossignac, J. (2008). An unconditionally stable maccormack method. *Journal of Scientific Computing*, 35:350–371.

[57] SMITH, R. S. and BAYER, E. M. (2009). Auxin transport-feedback models of patterning in plants. *Plant, Cell & Environment*, 32(9):1258–1271.

[58] Smith, R. S., Guyomarc'h, S., Mandel, T., Reinhardt, D., Kuhlemeier, C., and Prusinkiewicz, P. (2006). A plausible model of phyllotaxis. *Proceedings of the National Academy of Sciences*, 103(5):1301–1306.

[59] Stam, J. (1999). Stable fluids. In *Proceedings of the 26th Annual Conference on Computer Graphics and Interactive Techniques*, SIGGRAPH '99, page 121–128, USA. ACM Press/Addison-Wesley Publishing Co.

[60] Su, C., Kokosza, A., Xie, X., Pěnčík, A., Zhang, Y., Raumonen, P., Shi, X., Muranen, S., Topcu, M. K., Immanen, J., Hagqvist, R., Safronov, O., Alonso-Serra, J., Eswaran, G., Venegas, M. P., Ljung, K., Ward, S., Mähönen, A. P., Himanen, K., Salojärvi, J., Fernie, A. R., Novák, O., Leyser, O., Pałubicki, W., Helariutta, Y., and Nieminen, K. (2023). Tree architecture: A strigolactone-deficient mutant reveals a connection between branching order and auxin gradient along the tree stem. *Proceedings of the National Academy of Sciences*, 120(48):e2308587120.

[61] Tohidi, A., Kaye, N., and Bridges, W. (2015). Statistical description of firebrand size and shape distribution from coniferous trees for use in metropolis monte carlo simulations of firebrand flight distance. *Fire Safety Journal*, 77:21–35.

[62] Turing, A. (1952). The chemical basis of morphogenesis. *Philosophical Transactions of the Royal Society B*, 237:37–72.

[63] Vanella, M., McGrattan, K., McDermott, R., Forney, G., Mell, W., Gissi, E., and Fiorucci, P. (2021). A multi-fidelity framework for wildland fire behavior simulations over complex terrain. *Atmosphere*, 12(2).

[64] Whitaker, S. (1972). Forced convection heat transfer correlations for flow in pipes, past flat plates, single cylinders, single spheres, and for flow in packed beds and tube bundles. *AIChE Journal*, 18(2):361–371.

[65] Yang, Z. and Midmore, D. J. (2009). Self-organisation at the whole-plant level: A modelling study. *Functional Plant Biology*, 36(1):56.

[66] Zylstra, P. (2021). Linking fire behaviour and its ecological effects to plant traits, using frame in r. *Methods in Ecology and Evolution*, 12(8):1365–1378.